STUDIES OF NANOSTRUCTURES, ION BEAM PATTERNED SURFACES AND THEIR INTERACTION WITH DNA

By

SUBRATA MAJUMDER

PHYS07200604024
Institute Of physics
Bhubaneswar, India

A Thesis Submitted To The
BOARD OF STUDIES IN PHYSICAL SCIENCES
In Partial Fulfillment Of Requirements
FOR THE DEGREE OF
DOCTOR OF PHILOSOPHY
OF
HOMI BHABHA NATIONAL INSTITUTE

APRIL, 2013

Homi Bhabha National Institute

Recommendations of the Viva Voce Board

As members of the Viva Voce Board, we certify that we have read the dissertation prepared by Mr. Subrata Majumder, entitled " Studies of nanostructures, ion beam patterned surfaces and their interaction with DNA", and recommend that it may be accepted as fulfilling the dissertation requirement for the Degree of Doctor of Philosophy.

Date: 11-4-13 AM Jayannavar 11-4-13

Chairman - Prof. A.M. Jayannavar

SVarma **Date:** 11. Apr. 13

Guide / Convener - Prof. Shikha Varma

KKNanda **Date:** 11/04/13

Member 1 - Prof. K.K. Nanda

SMBhattacharjee **Date:** 11/04/13

Member 2 - Prof. S.M. Bhattacharjee

Date: 11/04/13

Member 3 - Prof. T. Som

Final approval and acceptance of this dissertation is contingent upon the candidate's submission of the final copies of the dissertation to HBNI.

I hereby certify that I have read this dissertation prepared under my direction and recommend that it may be accepted as fulfilling the dissertation requirement.

SVarma

(Shikha Varma)

Date: 11-4-13

Place: Bhubaneswar

STATEMENT BY AUTHOR

This dissertation has been submitted in partial fulfillment of requirements for the degree of Doctor of Philosophy of Homi Bhabha National Institute(HBNI) and is deposited in the library to be made available to borrowers under the rules of HBNI.

Brief quotations from this dissertation are allowable without special permission, provided that accurate acknowledgment of source is made. Requests for permission for extended quotation from reproduction of this manuscript in whole or in part may be granted by the Competent Authority of HBNI when in his or her judgment, the proposed use of the material is in the interests of scholarship. In all other instances, however, permission must be obtained from the author.

Signature:
(Subrata Majumder)

DECLARATION

I, Subrata Majumder, hereby declare that the investigations presented in the thesis have been carried out by me. The matter embodied in the thesis is original and has not been submitted earlier as a whole or in part for a degree/diploma at this or any other Institution/University.

Subrata Majumder
Institute of Physics
Bhubaneswar

To my Parents

To my beloved Wife

To my teacher Prof. Amal. K. Ghosh

Acknowledgements

This thesis is the result of nearly six years of work at Institute Of Physics, Bhubaneswar whereby I have been accompanied and supported by many personalities. It will be my pleasure, that now I have the opportunity to express my sincere gratitude to all of them.

The person, the name first come to my mind and will remain in my life as well, is my **Guide** *Prof. Shikha Varma*. She is not just a guide for me. She is my mentor, my friend and my well wisher. Actually it is she, who taught me how to take my work in life. Just after finishing my masters, I learned how to read a Physics book, and now after all these years of learning and working in experimental physics, I understood, how to read a scientific paper!!. It is she, who took care of me all the time I was here, staying thousand miles away from my near and dear, and felt me like her child. In a way, I feel, I am one of the luckiest person, who is blessed with such a nice and caring person as a guide and mentor. I learned from her the tricks to handle the physics problems in a very unique way. This basic teaching of her will help me in my lifetime academic career. I will always prey she stays beside me all the time as she used to be during the last few years. I spent my happiest time at IOP.

The another person I should mention after, is *Prof. Ajit Mohan Srivastava*. He is a very popular name in science community and I have been fascinated by him in several time by several ways. But his one sentence will make me remind him through out my life, is “every body has the right to forget”, although it came out of very sudden.

I must thank the people in my group, who always stayed with me and made me a part of their social as well as academic activities. I should thank Dipakda, Smruti, Dr. Ramarao, Dr Anupama, Vanraj, Indrani, and Shalik. I will miss their company from my heart. I am really thankful to Mr. Santosh Choudhury, the backbone of our XPS laboratory, for his support in all the experiments.

I am also thankful to Prof. S N Sahu, Prof. A. K. Pal, Prof. P. V. Satyam, Dr. S.N. Sarangi, Dr. B. P. Bug, Prof. G. B. N. Chainy, Dr. U. Subudhi, Prof. D. K. Avasthi, Prof. D. Kanjilal, Prof. K. Yoshikawa, Prof. Zinchenko and Prof. M. Ichikawa for their support and many useful discussions. I would like to thank to my all teachers from my School to University who helped me in many ways. I heartily acknowledge the support from my teacher *Prof Amal K Ghosh*. It would have been some other destination for me if he was not there at all. I am also grateful to DAE for supporting my stays at IOP. I wish to acknowledge the timely help from the technical as well as library and administrative staffs of IOP. I also thank to my all friends (Chitra, Sankha, Rupali, Soumia, Poulomi, Trilochan, Ranjita and others) for a memorable stay at IOP. I also thank Somnathda and Anantada for their all time support.

I am extremely grateful to my dearest parents (baba, bapu, ma, and my late mother) and my brothers, who have continuously supported me in all ways, and took all burden and pains that I was supposed to take care.

Finally, and most importantly, I am very grateful to my beloved wife Sanhita, for her love, affection and continuous support. She has been my inspiration and blessed me a beautiful life and family without which, it would have been impossible for me to go on with my life.

Date : (Subrata Majumder)

List of Publications/Preprints

Published and Communicated in Journals

[1]** "Ion irradiation induced nano pattern formation on TiO2 Single Crystal", ***S. Majumder, D Paramanik, V Solanki, I Mishra, D.K. Avasthi, D Kanjilal, and Shikha Varma, ***Appl.Surf.Sci*** 258, 4122-4124 (2012).

[2]** "Bandgap Tailoring of Rutile TiO2 (110) via Surface patterning with ECR sputtering", ***Subrata Majumder, D. Paramanik, V. Solanki, B.P. Bag, and Shikha Varma, ***Appl. Phys. Lett.***98, 053105 (2011).

[3] "Formation of Patterns and Scaling Properties of Tantalum Surfaces after Low Energy Ion Beam Irradiation", ***Subrata Majumder***, R. Medicherla, D. Paramanik, V. Solanki, I. Mishra, and Shikha Varma, ***Rad. Eff. Def. Solids.*** 166, 592-597 (2011).

[4]** "ZnO Nanocrystals: Magnetic Study", ***S. Majumder, V. Solanki, A. Gupta and Shikha Varma, ***Asian jour. of Phys.***, 19, (2 & 3), 269 (2010).

The (*) indicates papers on which this thesis is based.

[5]** “Fabrication, photoemission studies, and sensor of Hg nanoparticles templated on plasmid DNA”, ***Subrata Majumder, M. Priyadarshini, U. Subudhi, M. Umananda, G. B. N. Chainy, P. V. Satyam, and Shikha Varma, ***Appl. Phys. Lett.***, 94, 073110 (2009).

Also appeared in

- ***Nature India*** 68, February 27, (2009).
- ***Virtual Journal of Biological Physics Research***, 17, 5, March 1 (2009)

[6]** “X-Ray Photoelectron Spectroscopic Investigations of Modifications in Plasmid DNA after Interaction with Hg-Nanoparticles”, ***S. Majumder, M. Priya-darshini, U. Subudhi, G.B.N. Chainy and Shikha Varma, ***Appl. Surf. Sci***, 256 438-442(2009).

[7]** “Observation of Magnetic-Domains in Undoped ZnO Grains at Room Temperature”, ***S. Majumder, D. Paramanik, A. Gupta, Shikha Varma, ***Appl. Surf. Sci.***, 256 (2009) 513-516.

[8] “Studies of self-organized Nanostructures on InP(111) surfaces after low energy Ar^+ ion irradiation”, D. Paramanik, ***S. Majumder***, S. R. Sahoo, S. N. Sahu and S. Varma, ***Journal Of Nanoscience And Nanotechnology***, 8, 4227-30 (2008).

[9] “Nano Pattern Formation and Surface Modifications by Ion Irradiation”, Dipak Paramanik , ***Subrata Majumder***, S. R. Sahoo, Shikha Varma, ***Defence Science Journal : Ion Beam Technology*** Vol. 59, No. 4, July 2009, pp.413-424.

[10] “Formation of self organised Ta nano-structures by argon ion sputtering of Ta foil: XPS and AFM study”, V.R.R. Medicherla, ***S.Majumder***, D. Paramanik and Shikha Varma, ***The Journal of Electron Spectroscopy and Related Phenomena***, 180, 1-5 (2010).

[11] “Vertically aligned Mn-doped Zinc Oxide nanorods by hybrid wet chemical route”, R.N. Gayen, ***S. Majumder***, S. Varma, and A. K. Pal, ***Mater.Chem. Phys.*** 123, 138-146, (2010).

[12] “Scaling Studies Of Nano Dots Formed On InP(111) Surfaces Via MeV Implantations”, D. Paramanik, S. R. Sahoo, ***S. Majumdar*** and S. Varma, ***Jour. of Nanoscience and Nanotechnology***, 8, 4207 (2008).

[13] “Size Dependant Electronic Structure from InP Nanodots”, D. Paramanik, S. R. Sahoo, ***Subrata Majumder*** and Shikha Varma, ***Vacuum***, 1-55(2009).

[14] “Evolution of surface morphology of NiO thin films under swift heavy ion irradiation”, P. Mallick, Chandana Rath, ***S. Majumdar***, R. Biswal, D. C. Agarwal, Shikha Varma, D.K. Avasthi, P.V. Satyam and N. C. Mishra, ***Appl. Surf. Sci.***, 256 (2009) 521-523.

[15] “Surface plasmon characteristics of nanocrystalline gold/DLC composite films prepared by plasma CVD technique”, R. Paul, S. Hussain, ***S. Majumder***, S. Varma and A. K. Pal, ***Mater. Sc.& Engg. B***,164,156-164,(2009).

[16] “Effect of substrate temperature on implantation doping of Co in CdS nanocrystalline thin films”, S.Chandramohan, A. Kanjilal, S. N. Sarangi, ***S. Majumder***, R. Sathyamoorthy, C.-H. Hong, and T. Som, ***Nanoscale***, 2, 1155-1159 (2010).

[17] “Effect of Fe-ion implantation doping on structural and optical properties of CdS thin films”, S.Chandramohan, A. Kanjilal, S. N. Sarangi, ***S. Majumder***, R. Sathyamoorthy, and T. Som, ***Appl. Phys. A***, 99, 837-842 (2010).

[18] “Implantation-assisted cobalt doping induced modifications in structural, optical, and vibrational properties of CdS thin films”, S. Chandramohan, A. Kanjilal, S.N. Sarangi, ***Subrata Majumder***, R. Sathyamoorthy, T. Som, ***Journal of Applied Physics***, 106, 063506 (2009).

[19] “Surface roughness and power spectral density study of SHI irradiated ultra-thin gold films”, P. Dash, P. Mallick, H. Rath, A. Tripathi, Jai Prakash, D.K. Avasthi, ***S. Mazumder***, S.Varma, P.V. Satyam and N. C. Mishra, ***Appl. Surf. Sci.***,256(2009) 558-561.

[20] “Size Scaling Properties of Nanostructures Produced By Ion Sputtering”, ***Subrata Majumder***, D. Paramanik, and Shikha Varma, ***Phys. Rev. Lett.*** (2012) (under review).

[21]** “Enhance Biocompatibility of Plasmid DNA through Surface Patterning of Rutile TiO2 (110)”, ***Subrata Majumder, I. Mishra, and Shikha Varma (2012) (under preparation)

Conference Proceedings

[1] “Developing Nano-patterns on InP(111) surfaces after keV irradiation”, ***S.Majumder***, Dipak Paramanik, S.R.Sahoo , Shikha Varma, ***DAE Solid State Physics Symposium***, December 26-31,(2006), Barkatullah University,Bhopal, India

[2] “Time evolution of Nano-dots on InP(111) surfaces by 3 keV Ar ion Sputtering”, D. Paramanik, ***S.Majumder***, S. R. Sahoo and S. Varma, ***Mat. Res.Soc. Symp. Proc.*** 1020,GG04 (2007), April 9-13, Material research Society Spring Meeting, San Francisco, USA.

[3] “Utilizing Ion Beams For Forming Nanostructures On InP Surfaces, D. Paramanik”, ***S. Majumder***, S. R. Sahoo, S. K. Choudhury and Shikha Varma, Mesoscopic, Nanoscopic, and Macroscopic Materials (IWMNMM), ***AIP conf. Proc.*** 1063(2008)239.

[4] “Evolution Of Surface Topography On GaAs(100) And GaAs(111) At Normal And Oblique Incidence Of Ar Ions”, V. Venugopal, P. Das, T. Basu, S. Garg, ***S.Majumder***, S. N. Sarangi, S. R. Bhattacharyya, T. K. Chini, and T. Som, ***AIP Conf. Proc.***, 1276, 50, (2010) (International Conference on Advanced Nanomaterials and Nanotechnology (ICANN-2009))

[5] “Reduction of Anatase TiO2 on Si(111) by Ion Beam Sputtering”, V.R.R. Medicherla, R.R. Mohanta, K.L. Mohanta, Nimai C.Nayak, S. Choudhary, ***S.Majumder***, V. Solanki, Shikha Varma, D.M. Phase, and V. Sathe, ***AIP Conf. Proc.***, 1461, 403 (2012).

Synopsis

In recent years much effort has been undertaken to find the possible routes to fabricate the nanostructured materials with tailorable functional properties. The control at the nano scale during material synthesis process offers the possibility of designing high quality devices with improved performances [1]. The complex structure formed together by nanotechnology and bioengineering provide the template for designing useful nanostructures through the manipulation of DNA. DNA exhibit great flexibility and have shown potential as precisely controllable and programmable scaffolds for designing, fabricating, and organizing functional nanomaterials [2, 3].

In the present thesis, the formation of TiO_2, ZnO and Hg nanostructures and their interactions with DNA have been investigated by utilizing a variety of techniques. The oxide (TiO_2, ZnO) nanostructures display enormous potential for the applications in photo catalysis [4], optical and electronic devices, magnetic recording media and biosensors [5–7]. As these oxide nanostructures are being widely applied in several bioapplications, we have also explored their interaction with DNA. Mercury (Hg) is a carcinogenic element that perturbs and influences DNA structure. This imparts a serious concern for understanding the binding of Hg ion to DNA. The effect of interaction of DNA with Hg nanostructures, fabricated within the DNA scaffolds has been investigated here for understanding mercury related toxic effects as well as for the development of biosensor for detection of Hg contamination.

In the first part of this thesis, the results of investigations on TiO_2 nanostructures are presented. These nanostructures have been created on single crystal rutile TiO_2 surface by irradiating it with 3keV Ar^+ ions, from ECR source, with a fluence of $1.5x10^{19}$ ions/cm^2. Studies have shown that such nanostructures are formed due to the competition between the curvature dependent ion sputtering which roughens the surface and smoothening through various relaxation mechanisms [8]. Energetic ions incident on a solid material can influence the different physical and chemical properties of the material which can be utilized in research and technology in various ways [9]. Self organized structures fabricated by ion irradiation process become an attractive route to produce regular arrays of nanostructures on large areas in a single technological step. Several techniques like Atomic Force Microscopy (AFM), Field Emission Scanning Electron Microscope (FESEM), X-ray Photoelectron Spectroscopy (XPS), X-ray diffraction (XRD), Optical absorption (UV-Vis) spectroscopy and Photoluminescence (PL) have been utilized in the following investigations. The sputtering process on any bi-atomic surface is known to preferentially create vacancy of the low mass ion. The ion beam patterned surfaces show the presence of excess Ti^{+3} component as well as possess Ti rich zones which promote the creation of self assembled nanostructures. The TiO_2 nanostructures are about 50nm in size. On the TiO_2 surface, sputtering leads to the formation of oxygen vacancies, with the two associated electrons getting transferred to the empty 3d orbitals of the neighboring Ti atom and forming two Ti^{3+} sites [10]. The results show a nearly five times enhancement in absorbance of visible light, and about 5 times increase in luminescence from the ion beam sputtered surface. Along with this, about 0.1 eV narrowing of bandgap is also observed for nanodot patterned surfaces, in the absence of any dopant material. The analysis shows that the formation of crystalline rutile TiO_2 nanodots along with the development of Ti interstitials and Ti^{3+} complexes on the $TiO_2(110)$ surface, after ion beam sputtering, are responsible for these significant modifications. The results suggest that these nanodot patterned rutile TiO_2 surfaces can be used as an effective photo catalysts [11, 12].

In order to study the modifications in the biocompatibility of TiO_2 surfaces, after they are patterned with nanodots, we have investigated the interaction of DNA with ion beam modified surfaces. This has been studied as a function of fluence. Two fluences of 6×10^{15}

and 1.8×10^{16} ions/cm^2 have been utilized to create nanodots on TiO_2(110) surfaces. AFM and XPS studies have been utilized to characterize the surfaces both prior to and after conjugation of nanodots with DNA. XPS studies display formation of Ti^{3+} state for the nanodots prior to its interaction with DNA. However after the adsorption of DNA, the Ti^{3+} state is charge compensated through the negative charges of the DNA phosphate backbone. The PSD, performed on the AFM images has been utilized to estimate the persistence length, P, and the correlation length, ξ, related to the intermolecular separation. The results show that both P, and ξ are smallest on the DNA interacted virgin surface. Their values gradually increases as the irradiation fluence is increased. The enhanced P and ξ lengths, for increasing fluences, suggest increase in biocompatibility of the TiO_2 surfaces.

In the next part of the thesis, we have investigated the formation of ZnO nanostructures and their interaction with DNA. ZnO films of 500 and 1000nm were grown by Physical Vapor Deposition (PVD) method on Si(100) by heating a mixture of ZnO powder and graphite at 900°C in a system with a base pressure of 1×10^{-5} mbar. The graphite serves as the catalyst which can reduce the melting point of bulk ZnO powder below 900°C. The films were characterised by AFM, XPS, PL, XRD, Magnetic Force Microscopy (MFM), Magneto Optic Kerr Effect (MOKE) and Rutherford Back Scattering Spectrometry (RBS). The films were found to be discontinuous and show nanostructures with sizes of 90 and 270nm, respectively, for films of thickness 500 and 1000nm. These nanostructures, interestingly, show room temperature ferromagnetism even in the absence of any magnetic doping. The MFM images display the presence of magnetic domains with long range order of exchange interaction for the bigger nanostructures, while the smaller nanostructures show very isolated magnetic domains. This is also confirmed by the MOKE measurements, which show lower coercivity for the bigger nanostructures. The coercivity is found to be 520 and 230 Oe for the 90 and 270nm sized nanostructures, respectively. The reduction of the domain wall pinning effect produces smaller coercivity for larger nanostructures. PL results indicate presence of excess oxygen vacancies for bigger nanostructures and show emissions at 610nm and 630nm, representing the yellow and red wavelengths, respectively.

These emissions are attributed to the direct recombination of the photo generated charge carriers generated at the oxygen vacancy sites to the valance band state of Zn sites [13]. Presence of excess Oxygen vacancies, for bigger ZnO nanostructures, is also indicated by XPS studies. Results indicate that excess oxygen vacancies are responsible for the long range ferromagnetism observed in ZnO in the absence of any magnetic doping at the room temperature.

ZnO nanostructures have also been interacted with DNA and the modifications have been investigated using the PSD, utilizing AFM images. Results show extensive correlation, at the nanoscale, between the ZnO nanodots after their interaction with DNA.

In the last part of the thesis, the formation of mercury (Hg) nanostructures within the DNA scaffolds have been investigated. Techniques of XPS, AFM, Scanning Tunneling Microscopy (STM), Scanning Tunneling Spectroscopy(STS) and Transmission Electron Microscopy (TEM) have been utilized to investigate the conjugation of Hg nanostructures with DNA. The mercuric nanoparticles (NPs) have been fabricated within the DNA scaffold by utilizing the site specific interactions. The Hg NPs are embedded within the double helix and exclusively interact with the nucleic acid bases of DNA. In addition, protonation of the amine group, promotes the formation of metal-base complexes such as metal-purine (M-Pu) and metal-purine-pyrimidine (M-Pu-Py). Stabilization energy estimates suggest that guanine-cytosine (G-C) base pair sites are the likely candidates in the formation of these complexes. Formation of metal-base complexes as well as the modifications in transport (electrical) properties of DNA, after conjugation with Hg, can be utilized as sensors of mercury contamination and DNA assays [14, 15].

Thus in this thesis the formation of TiO_2, ZnO and Hg nanostructures and their interactions with DNA have been investigated. Self assembled TiO_2 nanostructures have been created on rutile TiO_2 surfaces by ion beam patterning. Fabrication of crystalline TiO_2 nanodots also produce excess Ti^{3+} component and Ti rich zones and all these together lead to modifications in bandgap, absorbance and PL emission from nanodot patterned surfaces. Results of interaction of DNA with TiO_2 nanostructures, on the ion beam patterned surfaces, indicate that these surfaces become highly biocompatible after sputtering. ZnO nanostructures, created through PVD method are semiconducting in nature and interestingly show room temperature ferromagnetism even in the absence of any magnetic doping. Results presented here suggest that oxygen vacancies are responsible for the room temperature ferromagnetism observed in ZnO nanstructures. An increased correlation in ZnO nanodots is observed after they are interacted with DNA. Hg nanostructures have been fabricated within the DNA strands through the interaction of Hg salt with plasmid DNA. Formation of two Hg metal-base complexes and modifications in the transport properties of metal conjugated DNA can be utilized as sensor for mercury contamination.

References

[1] George M. Whitesides and Bartosz Grzybowski, Science, 295, 2418 (2002).

[2] J. Zhang, Y. Liu, Y. Ke, and H. Yan, Nano Lett. 6, 248 (2006).

[3] L. Berti and G. A. BurLey, Nat. Nanotechnol. 3, 81 (2008).

[4] Fujishima, T.N. Rao, and D.A. Tryk, J. Photochem. Photobiol. C, 1,1 (2000).

[5] N. Huang, Y.R. Chen, J.M. Luo, J. Yi, R. Lu, J. Xiao, Z.N. Xue, and X.H. Liu, J. Biomater. Appl. 8, 404 (1994).

[6] Roger J. Narayan, Nancy A. Monteiro-Riviere, Robin L. Brigmon, Michael J. Pellin, Jeffrey W. Elam, J Miner Met Mater Soc, 61, 6, 12-16 (2009).

[7] K. Keren, M. Krueger, R. Gilad, G. Ben-Yoseph, U. Sivan, and E. Braun, Science 297, 72 (2002).

[8] S. Facsko, T. Dekorsy, C. Koerdt, C. Trappe, H. Kurz, A. Vogt, H. L. Hartnagel, Science 285, 1551 (1999).

[9] L.C. Feldman, J.W. Mayer and S.T. Picraux In: Material Analysis By Ion Channeling, Academic Press, New York, p. 1.1. (1982).

[10] V.E.Henrich, G. Dresselhaus, and H.J. Zeiger, Phys. Rev. Lett., 36, 1335 (1976).

[11] S. Majumder, D Paramanik, V Solanki, I Mishra, D.K. Avasthi, D Kanjilal, and Shikha Varma, Appl.Surf.Sci 258, 4122-4124 (2012).

[12] Subrata Majumder, D. Paramanik, V. Solanki, B.P. Bag, and Shikha Varma, Appl. Phys. Lett.98, 053105 (2011).

[13] S. Majumder, D. Paramanik, A. Gupta, Shikha Varma, Appl. Surf. Sci., 256, 513-516 (2009).

[14] Subrata Majumder, M. Priyadarshini, U. Subudhi, M. Umananda, G. B. N. Chainy, P. V. Satyam, and Shikha Varma, Appl. Phys. Lett. 94, 073110 (2009).

[15] S. Majumder, M. Priyadarshini, U. Subudhi, G.B.N. Chainy and Shikha Varma, Appl. Surf. Sci, 256, 438-442(2009).

Contents

List of Tables

List of Figures

Chapter 1

Introduction

1.1 Introduction

For last few decades, nanostructured materials with tailorable functional properties have received immense attention due to their importance in fundamental science and very prominent role in numerous applications. Extensive efforts have been undertaken to achieve these nanostructures, through variety of routes. Top down or bottom up approaches, with control at the nanoscale during material synthesis process, offer the possibility of designing devices with desirable characteristics and improved performances [1–3]. With nano-bio interfaces, presenting exceptional properties and many unique behaviors, their understanding becomes significant for fundamental studies as well as in the field of biophysical and biomedical research. In this direction, DNA biomolecules play an important role and DNA modified surfaces have received considerable attention in the field of bio-nanotechnology due to their importance in the development of several biosensing and diagnostic tools such as DNA microarrays. DNA also exhibits great flexibility and have shown potential as precisely controllable and programmable scaffolds for designing, fabricating, and organizing functional nanomaterials [4, 5].

To date, two basic approaches for the fabrication of semiconductor nanostructures have been pursued. In the top-down approach, techniques are used for direct patterning of nanostructures, whereas the bottom-up approach relies on fabricating nanostructures using smaller components e.g., atoms, molecules or their clusters. Self-organization phenomena open the way for the formation of a regular array of nanostructures on large areas in a single technological process step. Self-organized semiconductor quantum dots have been produced by the Stranski-Krastanow growth mode in molecular beam epitaxy and metal-organic vapor phase epitaxy, in which coherent island formation occurs during the growth of lattice-mismatched semiconductors [6].

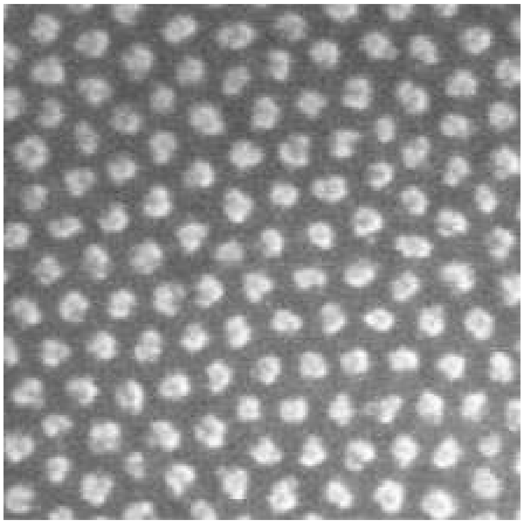

Figure 1.1: Quantum dots on GaSb(100) have been fabricated by normal incidence ion sputtering using 420 eV Ar^+ ion source (from Facsko et al. (1999)). Image is from 500×500 nm^2 area. Dots as small as 15 nm have been reported.

Physical vapor deposition technique utilizes the self organized bottom-up approach for fabricating nanostructures with versatile properties. Patterning of surfaces by ion beams, on the other hand, presents a controlled and cost effective method of production of well ordered self assembled nanostructures by top-down technique. Spontaneous self-organization processes have been used to create patterns with lateral feature sizes as small as 15 nm, and with a good short-range order [7] as shown in fig. 1.1. DNA nanotechnology exploits the self recognition properties of DNA to self assemble nanostructures in a bottom-up approach.

Fabricating nanostructures of oxide materials are of great interest because of their versatile diversity of physical and chemical properties achieved through tuning the dimension of the nanocrystals grown on single crystals and thin films. In recent years much effort has been undertaken to find the possible routes to fabricate the nanostructured materials with tailorable functional properties. The control at the nano scale of material structure during the synthesis process offers the possibility of designing high quality devices with improved predefined performances. The nanosized Titania (TiO_2) and Zinc Oxide (ZnO) have gained importance because of their modified electronic and optical properties which have many applications in photocatalysis [8–10], photo electrochemical cells [11–13], gas and humidity sensors [14, 15]. Being wide band gap semiconductors TiO_2 and ZnO have been widely studied for their superior properties in photoconduction and photocatalysis. They also show compatibility in biological fields [16]. The performance of the materials strongly depends on the modification of its electronic and structural properties at the surface and interface [17]. The controlled growth of the nanocrystalline TiO_2 and ZnO is thus crucial for advanced electronic materials. Till today several growth techniques like gas condensation, reactive magnetron sputtering [18], pulsed laser deposition [19–22], metal organic chemical vapor deposition(MOCVD) [23, 24] have been applied to grow the TiO_2 and ZnO nanocrystals. Different surrounding temperature during thermal treatment process however can remarkably change their physical properties [25, 26].

DNA is a polyelectrolyte with a high density of negative charges. It is gaining importance as a unique scaffold for templating nanostructures and nano wires. DNA, due to its base sequences, offer specificity and thus is an attractive assembly linker for bottom up nanofabrication. The immobilization of deoxyribonucleic acid (DNA) on a solid surface is of interest in studies of molecular recognition biosensors [27], DNA-based bio-chip [28] etc. The understanding of chemical and structural modification of the DNA molecule, after its interaction with the metal oxide surfaces and nanoparticles [29, 30], is very crucial in tuning its properties for applications.

In the present thesis, the formation of TiO_2, ZnO and Hg nanostructures and their interactions with DNA have been investigated by utilizing a variety of techniques. The oxide (TiO_2, ZnO) nanostructures display enormous potential for the applications in photo catalysis [8], optical and electronic devices, magnetic recording media and biosensors [16,31,32]. TiO_2 nanostructures have been fabricated by utilizing the top-down approach, where sputtering by ion- irradiation leads to the formation self assembled nanostructures. ZnO nanostructures through bottom-up approach, have been produced by physical vapor deposition method. As the oxide nanostructures are being widely applied in several bio-applications, we have also explored interaction of TiO_2 and ZnO nanostructures with DNA. Mercury (Hg) is a carcinogenic element that perturbs and influences DNA structure. This imparts a serious concern for understanding the binding of Hg ion to DNA. The effect of interaction of DNA with Hg nanostructures, fabricated within the DNA scaffolds has also been investigated here for understanding mercury related toxic effects as well as for the development of biosensor for detection of Hg contamination.

This chapter is organized in following order. In section 1.2, we discuss the basics of ion-solid interaction. The sputtering process along with the formation of patterns by ion beam sputtering and their theoretical aspects are discussed in section 1.3. The interaction of nanostructures with DNA will be discussed in section 1.4.

1.2 Basics of Ion-Solid Interaction

Energetic ions incident on a solid material can influence the physical and chemical properties of the material which can be useful in research and technology in various ways [33]. In its passage through the matter, an energetic ion can interact with the atomic electrons, which is purely a coulombic interaction that results in atom to go to an *Excited* or *Ionized* state and eventually return to the *ground* state.

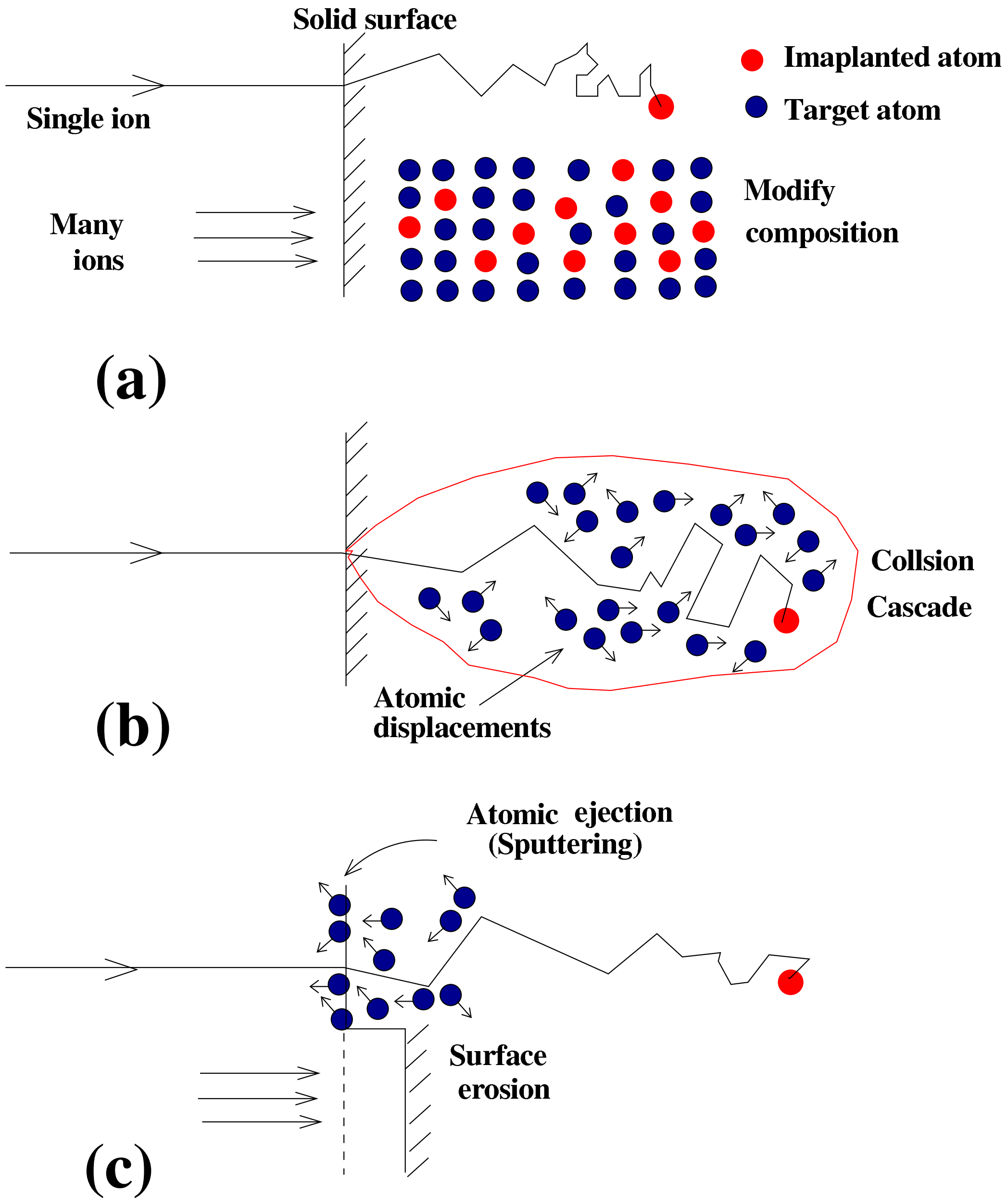

Figure 1.2: Basic materials modification processes (a) implantation; (b) damage; and (c) sputtering (from ref. [52]).

The primary processes leading to material modification via ion beam irradiation are shown in fig. 1.2. As shown in fig. 1.2(a) ion implantation can lead to the build up of a concentration profile of foreign atoms within a solid, thus altering the composition in the implanted zone. The spatial distribution of foreign atoms will depend on the ion energy and the stopping (nuclear and electronic) processes. In the fig. 1.2(b) as illustrated, the “hard” nuclear collisions can causes the displacement of the target atoms from their regular lattice sites. Even a single heavy ion can lead to the displacement of several tens, or even hundreds, of lattice atoms within the volume surrounding the ion trajectory. This is termed as collision or displacement cascade. As a consequence, ion bombardment can create considerable structural damage to the material.

Figure 1.2(c) illustrates the phenomena which is termed as the “sputtering”, where the nuclear collision of ions can sometimes lead to the ejection of surface atoms from target. This phenomenon of sputtering can cause surface erosion and can also sometimes produce self assembly of nano structure on surfaces. The phenomenon of sputtering is predominant at low (keV) energies whereas the lattice modification and deep layer implantations occur at high (MeV) energies.

When energetic ions strike a surface the ions lose energy by two nearly uncorrelated basic energy transfer mechanisms. The energy deposition is commonly described by the “stopping power” [34] dE/dx which gives the energy transfer per path length of a particle along its trajectory. The elastic collisions with the atomic nuclei, produce nuclear energy loss ($S_n = (dE/dx)_n$) whereas, inelastic excitations and ionizations of the electrons produce electronic energy loss ($S_e = (dE/dx)_e$) [34]. The total stopping power is the sum of both Stopping Powers. The basic interaction process in both the cases is Coulomb type, a pure Coulomb potential for ion-electron interactions and a screened Coulomb potential for nuclear interaction. However, the energy regions of the dominance for these two processes are different.

At ion energies of a few keV/amu, where the ion velocity is much less than the Bohr velocity of electrons, the interaction time between the projectile and a nucleus is relatively large. In this energy regime, nuclear energy loss is the predominant mechanism. At higher energies of about a few MeV/amu, where projectile velocity is comparable to the Bohr velocity of electrons, inelastic electronic energy loss becomes the major slowing down process. The distinct regions of S_n and S_e dominance are shown in fig. 1.3 which shows the variations of both the stopping powers of Argon (Ar) ions traversing through Titanium Dioxide (Ti

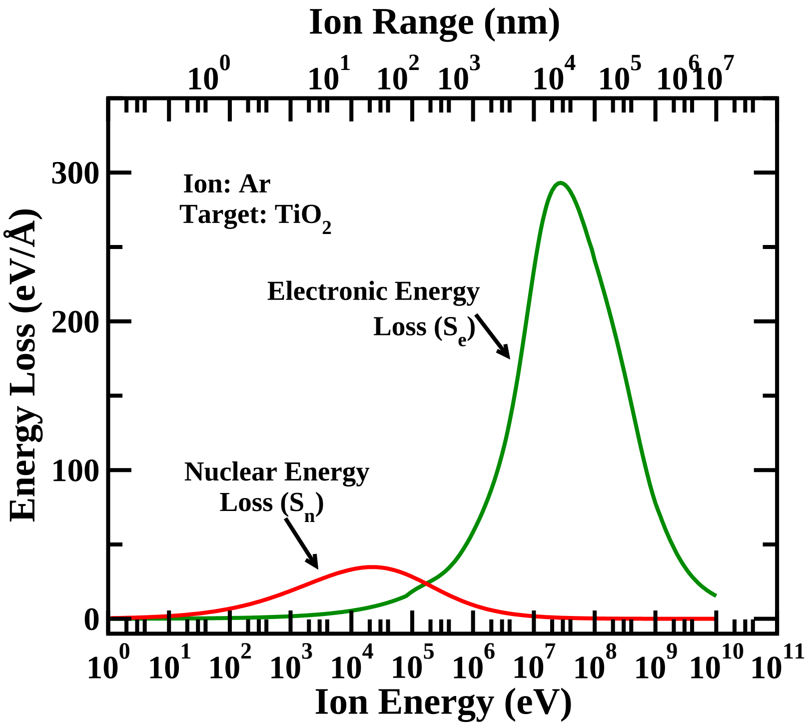

Figure 1.3: Variation of stopping power, nuclear energy loss S_n and electronic energy loss S_e for Ar ions in TiO_2 target estimated using SRIM2012 simulation code [35].

1.3 Sputtering Process

Sputtering is the removal of near surface atoms from the target material. A qualitative picture of the sputtering process is as follows: an incoming ion penetrates into the bulk of the material and undergoes a series of collisions with the atoms of the substrate. Some of the atoms undergo secondary collisions, thereby generating another generation of recoiling atoms. A vast majority of atoms will not gain enough energy to leave their lattice positions permanently. However, some of them will be permanently removed from their sites.

The atoms located in the close vicinity of the surface, which can gain enough energy to break their bonds, will be sputtered. Usually the number of sputtered atoms is orders of magnitude smaller than the total number of atoms participating in the collision cascade.

An ion sputtering event is best described as a collision process [36] involving electronic stopping and nuclear scattering. Ion sputtering occurs when an ion colliding with one or more target nuclei results in elastic scattering events. If the energy thus imparted to near surface atoms is large enough to break atomic bonds, atoms are sputtered. The sputtering yield (S) is defined as the mean number of sputtered target atoms per incident ion:

$$S = \alpha N S_n(E)/E_B \tag{1.1}$$

Here, N is the target atom density, E_B is the binding energy of a surface atom and α is a material and geometry dependent parameter. The product NS_n(E) represents the energy loss per unit length as the ion travels in the target. As the definition of sputtering yield implies, the number of atoms removed are assumed proportional to the number of incident particles while holding all other factors constant. Sputtering yield is strongly dependent on the kinetic energy of the bombarding ion. The sputtering yield is very sensitive to the surface binding energy and for real surfaces this changes with its roughness and stoichiometry. When multi-component targets are bombarded with heavy ions, various elemental constituents may not be sputtered at the same rate. Preferential sputtering, of lighter atoms compared to heavier atoms, can result in a surface composition which differs appreciably from the stoichiometric bulk composition [37, 38]. However, it is quite difficult to distinguish between preferential sputtering and other processes such as radiation induced mass transport and segregation effects, all of which may lead to near-surface composition changes during sputtering.

1.3.1 Formation of Patterns by Ion Beam Sputtering Technique

Self-organized structure formation on the nanoscale induced by ion-beam erosion, i.e. the removal of target material by bombarding its surface with ionized particles, has recently turned into a highly active research area of surface science with deep connections to the modern theory of nonequilibrium systems. Under some conditions of uniform ion irradiation of a solid surface, one can generate a spontaneous sputter pattern topography on the solid surface. The patterned surface very often takes the form of one-dimensional ripples or two-dimensional arrays of dots. The periodicity of the pattern is understood to arise as a result of a kinetic competition between the surface roughening effect of the ion beam and the morphological relaxation. In the last few decades, significant amount of experimental and theoretical works have been carried out on the ion stimulated formation and relaxation of self-organized topographic features on different solid surfaces [39–54]. For example the spontaneously self-organized dots and ripples, as small as 20 nm, have been successfully formed on GaSb [55] and SiO_2 [42] surfaces as shown in fig. 1.4.

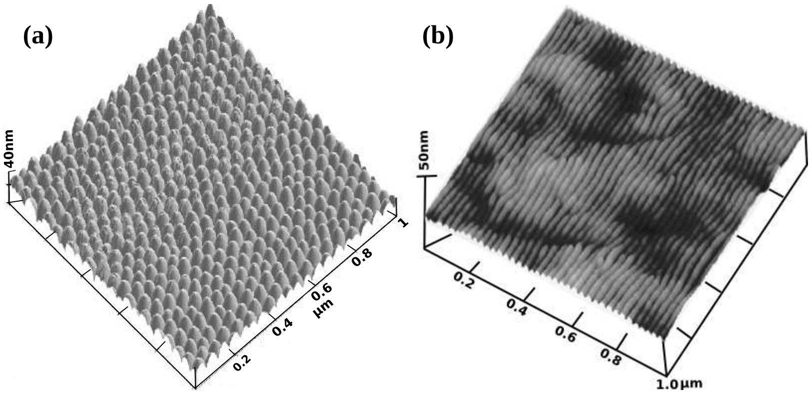

Figure 1.4: Atomic force microscope−height profile of (a) quantum dot structures created on GaSb(100) sputtered in normal incidence with Ar^+ ions of 500 eV energy (from [55]) and (b) ripple structure on SiO_2 sputtered with 1 keV Xe^+ ions incident at 55° with respect to the surface normal (from [42]).

1.3.2 Theoretical Aspects of Pattern Formation via Sputtering Technique

All theories of pattern formation (created via ion sputtering) originate from the quantitative description of the process of ion sputtering through Sigmund's [56] model demonstrating the instability of a planar surface to uniform ion beam erosion. According to his model, assuming an amorphous target in infinite medium, the probability of an atom being dislodged from the target surface is simply proportional to the total energy that reaches the atom from nearby ion collision processes. In the elastic collision regime, at the energies of a few keV where electronic stopping is not dominating, the deposited energy can be approximated by Gaussian distribution near its maximum.

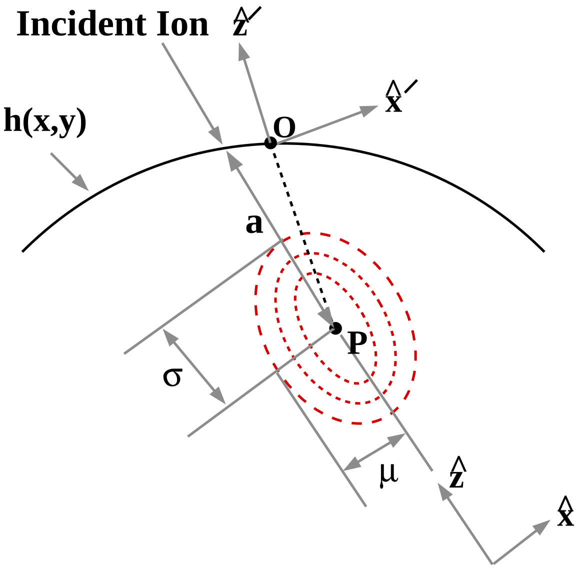

Figure 1.5: Schematic illustration of Sigmund's model showing the contour of energy distributed by an incident energetic ion. The single ion penetrates the bulk of the material and stops at point *P*, spreading out all its kinetic energy to the neighboring sites following a Gaussian form of transversal (μ) and longitudinal (σ) widths. The energy released at point *P* contributes to the erosion rate at the point *O* on the surface.

The effective process can be visualized in a way as shown in fig. 1.5, where the ion beam approach to the solid surface is conveniently described by a height function $z = h(x,y)$, in the z direction. The energy distribution at (x',y',z') due to an ion with kinetic energy E is given by:

$$E(x,y,z;x',y',z') = \frac{\varepsilon}{(2\pi)^{3/2}\sigma\mu^2} \exp\left[-\frac{(x'-x)^2+(y'-y)^2}{2\mu^2} - \frac{(z'-z)^2}{2\sigma^2}\right] \tag{1.2}$$

where ε is the total energy released by the ion after traversing a depth of length a. Since we are interested in the surface evolution, the energy reaches at the surface for $z = h(x,y)$ and $z' = h(x',y') - a$, is therefore,

$$\begin{aligned} E(x,y;x',y') = {} & \frac{\varepsilon}{(2\pi)^{3/2}\sigma\mu^2}\cdot \\ & \exp\left[-\frac{(x'-x)^2+(y'-y)^2}{2\mu^2} - \frac{(h(x',y')-a-h(x,y))^2}{2\sigma^2}\right] \end{aligned} \tag{1.3}$$

The integration of the equation1.3, gives the total power density at the surface $h(x,y)$. Thus the velocity of a surface element due to the sputtering can be expressed in a simple way, where η is a proportionality constant relating to the sputtering rate and the power density, and J the flux of the incident ion;

$$v(x,y) = \eta J \int\int dx'dy' E(x,y;x',y') \tag{1.4}$$

In the above equation 1.4, the integrand is very much localized due to its Gaussian nature of distribution, however the integration is extended for the entire surface. in the present coordinate system the velocity of the element (normal to the surface) can be expressed as:

$$v = -\frac{\partial h/\partial t}{\sqrt{1+|\nabla h|^2}} \tag{1.5}$$

This equation describes the complete mathematical description of the surface topographic evolution under the ion beam sputtering. From the above description one observes that (discussed in detail in ref. [57]) the evolution of the surface; i.e., the effect of sputtering

(sputtering yield) on a surface, is strongly dependant on the nature of the surface topography. It has been shown that the topography of a surface can indeed influence the rate of change of the sputtering erosion yield, and the rate of the erosion at any point on the surface is proportional to the amount of energy deposited at that point on the surface.

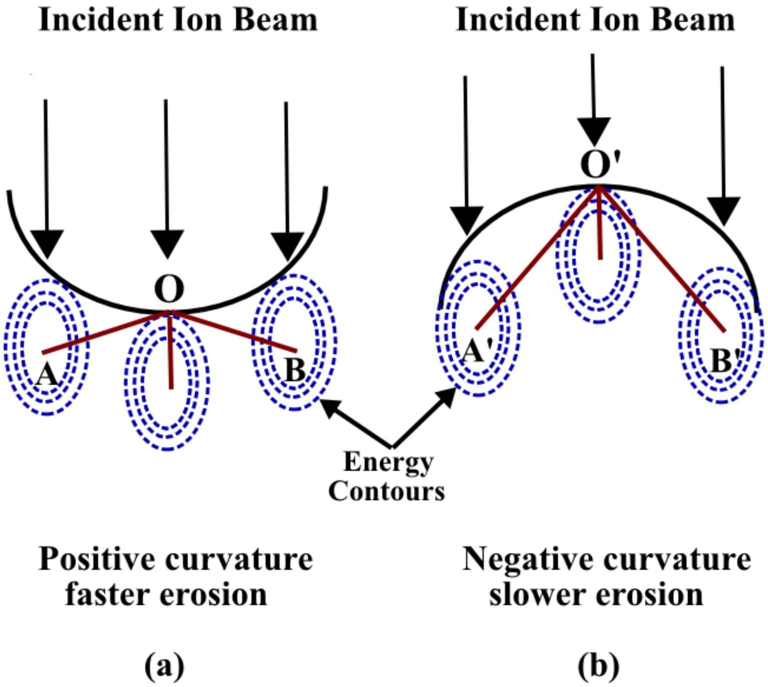

Figure 1.6: Schematic of Ion energy deposition profile for two ((a) concave and (b) convex) different surfaces. The energy deposited at O is larger than at O', since $O'A' > OA$.

Figure 1.6, shows two ion bombarded ((a)concave and (b) convex) surfaces. Following the Eq. 1.3, the energy density deposited at O for the ion penetrated at A is larger than the energy deposited at O' due to the ion penetrated at A', since $O'A' > OA$. Thus it implies that the valleys are more quickly erosion prone than the crests and it amplifies the initial differences in heights of the valleys and crests leading to the presence of a negative surface tension on the eroding surface. This different rates of erosion thus create the surface instability. To overcome this instability, Sigmund proposed an alternative flattening process which plays in parallel to the above roughening process and finally stabilizes the surface.

Based on the theory by Sigmund, Bradley and Harper (BH) [48] have proposed a linear differential equation for the description of surface evolution after ion beam erosion. The height modulation $h(x,y,t)$ of the eroding surface is given by:

$$\frac{\partial h}{\partial t} = -v_o + \nu \nabla^2 h - D\nabla^4 h \tag{1.6}$$

where v_o is the constant erosion velocity, ν is the effective negative surface tension and the term D is related to various surface smoothening processes like surface diffusion, etc. The realistic solution of Eq. 1.6 predicts the exponential growth of the surface with the fluence, along with a characteristic wavelength which is independent of the fluence. But in most of the cases after the sputtering very different types of the surface morphologies are observed, which do not follow the above linear BH model. To describe the ion induced pattern morphology of a semiconductor or amorphous material surface, in 1995, Cuerno and Barabasi (CB) [58] developed a model which maps very nicely to the early time scale of BH model, but the latter time scale dynamics is dominated by the nonlinear term proposed by Kuramoto-Tsuzuki [59]. Taking care of the nonlinear effects, the modified characteristic equation describing the surface evolution is:

$$\frac{\partial h}{\partial t} = -v_o + \nu \nabla^2 h - D\nabla^4 h + \frac{\lambda}{2}(D\nabla h)^2 + \eta \tag{1.7}$$

where the term η is the uncorrelated noise with zero mean, i.e.; the randomness resulting from the stochastic nature of the incident ions striking the surface. The term $\frac{\lambda}{2}(D\nabla h)^2$ accounts for the slope dependent erosion yield which eventually stabilizes the surface by saturating the surface roughness with time. Depending on the sign of the nonlinear term the surface evolution may show kinetic roughening [60–62].

1.3.3 Theoretical Aspects of Pattern Formation via Physical Vapor Deposition Technique

Physical Vapor Deposition (PVD) is one of the basic methods to create nanostructures and thin films. The PVD technique is based on vaporization process from a solid source in the form of atoms or molecules. The process requires vacuum conditions (at least 10^{-4} mbar) to prevent collisions of the vapor flux with gas molecules as it is transported from the source to the substrate. Typically, PVD processes are used to deposit films with thicknesses in the range of a few nanometers to dozens of micrometers; however they can also be used to form multilayer coatings, graded composition deposits, very thick deposits and aligned structures.

The term *physical vapor deposition* originally appeared in the 1966 book "Vapor Deposition" by C. F. Powell, J. H. Oxley and J. M. Blocher Jr., but as far back as 1838, Michael Faraday used PVD technique to deposit coatings). PVD is a variety of vacuum deposition methods namely:

- *Cathodic Arc Deposition*: In which a high power electric arc discharged at the target (source) material blasts away some into highly ionized vapor to be deposited onto the substrate.

- *Electron beam physical vapor deposition*: In which the material to be deposited is heated to a high vapor pressure by electron bombardment in "high" vacuum and is transported by diffusion to be deposited by condensation on the substrate.

- *Evaporative deposition*: In which the material to be deposited is heated to a high vapor pressure by electrically resistive heating in "low" vacuum.

- *Pulsed laser deposition*: In which a high power laser ablates material from the target into a vapor.

- *Sputter deposition*: In which a glow plasma discharge (usually localized around the “target" by a magnet) bombards the material sputtering some away as a vapor for subsequent deposition.

PVD processes are carried out under vacuum conditions. The whole process involved three steps:

- **Evaporation**

  In this process the source material atoms get heated and convert to gaseous state from condensed solid or liquid state. According to the *Kinetic theory of gas* the impingement rates are proportional to the equilibrium vapor pressure (P) of the evaporant at T. The evaporation flux can be expressed (in unit of $molecules/cm^2sec$) as:

  $$\frac{1}{A_e}\cdot\frac{dN_e}{dt}=\frac{P}{\sqrt{2\pi m k_B T}} \tag{1.8}$$

  where, A_e is the area of evaporation, m is the molecular weight, and k_B is the Boltzmann constant. Hence, the mass evaporation rate (in g/cm^2sec) of the evaporant Γ, is:

  $$\Gamma = m\frac{1}{A_e}\cdot\frac{dN_e}{dt}=P\left(\frac{m}{2\pi k_B T}\right)^{\frac{1}{2}} \tag{1.9}$$

  and the mass of the evaporated material is:

  $$M_e=\int_0^t\int_0^{A_e}\Gamma\, dA_e\, dt \tag{1.10}$$

- **Transportation**

  In this stage of transportation of the evaporated material from source to the substrate, the important entity is the directional distribution of evaporant material along the substrate. If directions are random, only $dA_s\cos\theta/4\phi r^2$ atoms are headed in the direction towards the area dA_s (see fig. 1.7(a)), where the volume of the possible atoms escaping towards

dA_s, from the source of evaporant area dA_e is = $vdt\cos\phi\, dA_e$ (v is the average velocity of the atoms).

Hence the distribution of mass (dM_s) hitting the area dA_s (integrating over whole source area and time), with the density ρ is:

$$\frac{dM_s}{dA_s} = M_e \frac{\cos\theta \cdot \cos\phi}{\pi r^2} \tag{1.11}$$

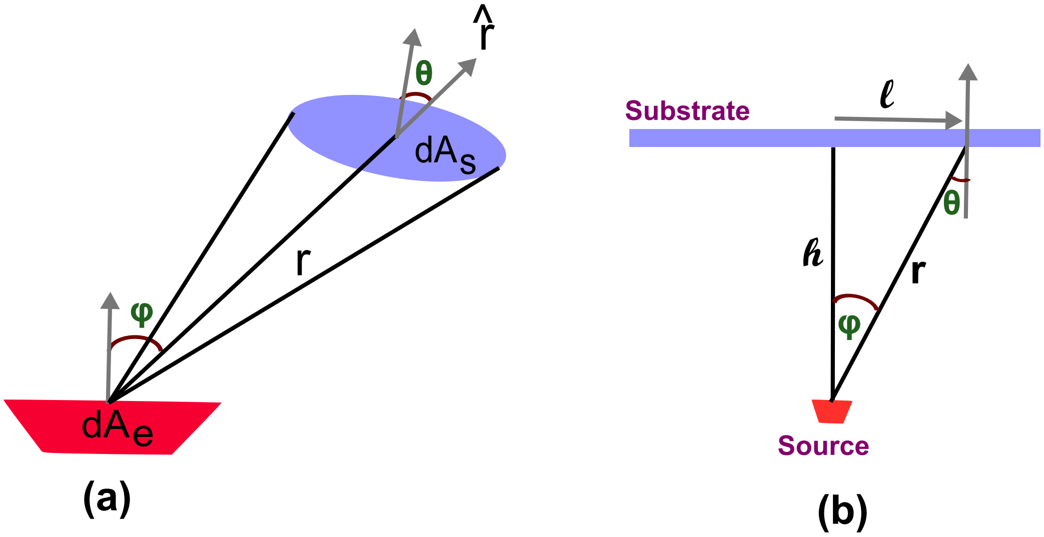

Figure 1.7: Schematic of (a) directional distribution of evaporant source, and (b) Physical thermal deposition on a flat substrate.

- **Deposition onto substrate**

  In this phase, the evaporant is condensed onto a substrate. Considering a flat substrate, perpendicular to the source as shown in fig. 1.7(b), we have the conditions, $\theta = \phi, \cos\theta = cos\phi = h/r,$ and $r = \sqrt{h^2 + l^2}$; The local thickness of the evaporant deposition can be expressed as:

$$d_l = \frac{1}{\rho} \cdot \frac{dM_s}{dA_s} = \frac{1}{\rho} \cdot \frac{M_e \cos\theta \cdot \cos\phi}{\pi r^2} \tag{1.12}$$

where, $d_0 = \frac{1}{\rho} \cdot \frac{M_e}{\pi h^2}$, is the maximum film thickness. Hence,

$$\frac{d_l}{d_0} = \left[1 + \left(\frac{l}{h}\right)^2\right]^{-2} \tag{1.13}$$

This shows the film deposited on a substrate will have a small thickness non-uniformity. As for example, a 3inch diameter wafer suspended 18 inches above the source the $d_l/d_0 = 0.986$, or a non-uniformity of 1.4 %.

Depending on eq. 1.12, deposition on the substrate can lead to the formation of discontinuous/continuous films. Early stage of this growth can also demonstrate formation of variety of nanostructures pattern on the substrate. The substrate crystallinity can also influence the size and shape of the nanostructures.

1.4 Interaction of Nanostructures with DNA

Nano-bio interfaces are getting importance due to their versatile and vivid application possibilities in many disciplines. The metal oxides are emerging as important materials because of their versatile properties such as high-temperature superconductivity, ferroelectricity, ferromagnetism, piezoelectricity and semiconductivity. The appropriate mixing of these properties along with the biological species will thus definitely become blueprints to control many unsolved mysteries. The emerging sensor technology based on nanostructure and nanoparticle composites with chemical and biological molecules is expected to be extremely beneficial for bio-applications. For example, the recent study by Paunesku et al. [63] has shown that the bio-nanocomposites formed from tiny ($\sim$ 4.5 nm) TiO_2 nanoparticles with oligonucleotide DNA can be used as new tool for gene therapy where the TiO_2 nanoparticles not only retain the intrinsic photocatalytic property and the oligonucleotide DNA retains its bioactivity, but the composites also possess the chemically and biologically unique new property of a light-inducible nucleic acid endonuclease. The recent advances in the hybrid nanotechnology mainly focus towards the cellular imaging or DNA microarray developments [64–67] involving nucleic acids which are predominantly linked with sequence-specific nucleic acid interactions. The thionin incorporated bi$-$layer of DNA/nano$-$$TiO_2$ film modified nanocomposite electrode surfaces have been applied as a biosensor for the detection of H_2O_2 [68]. Recently it has been found that the biological effect of ultrafine TiO_2 was different from that of fine TiO_2 [69].

TiO_2 is extensively used in bioimplants due to its anticorrosion characteristics. Biological species have been known to interact mainly with the outermost atomic layers of the implant surface [70]. Also their interaction are most likely mediated at the molecular level by a combination of specific molecule-surface interactions. The surface properties of the implant, specifically the surface chemistry, topography, roughness and wettability can affect the type, and quantity of conformation of the biological molecule. Metal oxides are strong adsorbants of organic compounds and show extensive interactions [71]. Thus, controlling the chemical and physical properties of the metal oxide surfaces is very important for bio- applications.

ZnO semiconductor nanostructures have displayed unique and useful properties in the field of nano-biotechnology. They have demonstrated exceptional behavior as biosensing devices [72, 73]. The material receives extra attention due to its wide band gap and large exciton energy along with the possibilities of being fabricated in a variety of different nanostructures like; nanowires, nanotubes, nanorods, nanoribbons, nanoneedles, nanocables, etc. [74]. The electrochemical behavior of hemoglobin entrapped in Nafion/nano-ZnO film on the surface of an ionic liquid-modified carbon paste electrode was investigated by Sun et al. [75]. Liu et al. [76] have fabricated carbon- decorated ZnO nanowire arrays which can be used to monitor the direct electrochemistry and act as biosensor for different enzymes like; glucose oxidase, horseradish peroxidase. The same group has also succeeded to form an amperometric glucose biosensor based on aligned ZnO nanorod films [77].

In a pioneering work, Alivisatos et al [78] in 1996, showed that the DNA molecules can be successfully used either to organize nanoparticles into arrays via base pairing or as linear templates for the fabrication of metallic or semiconducting nanowires. Similar kind of interesting controllable template was designed by Cofffer et al. in the same year [79] and they were able to dictate the overall structure of an assembly of individual nanoparticles with the control on the size and shape of a polynucleotide. One of the major advantages regarding DNA-assisted nanofabrication is the availability of various well-developed techniques concerning the synthesis, manipulation, assembly, and structural tailoring of these DNA molecules. Thus, excellent control of the nanostructures derived from precursory DNA scaffolds is expectable. The DNA templated fabrication could be performed not only in solutions but also on surfaces.

The organization of this thesis is as following. Chapter 2 discusses the various experimental techniques that have been utilized in this thesis. In chapter 3 we discuss the fabrication of nanostructures on TiO_2 surfaces by ion irradiation method. The surface morphology and optical absorption properties of the patterned surfaces have also been investigated. The interaction of DNA with the ion irradiated and nanodot patterned surfaces of TiO_2 are discussed in chapter 4. The investigations of the modification in surface morphology, persistence length of DNA and its correlation length will also be reported. Chapter 5 discusses the growth of ZnO nanostructures by Physical vapor Deposition method. The chapter also reports on the magnetic studies carried out on these nanostructures. The interaction of DNA with the nanostructures will also be discussed. In chapter 6 we discuss the conjugation properties of Hg nanostructures with DNA. This chapter also demonstrates that DNA can act as a *tiny sensor* of mercury. The conclusions are presented in Chapter 7.

References

[1] George M. Whitesides and Bartosz Grzybowski, Science, 295, 2418 (2002).

[2] K. K. Nanda and S. N. Sahu, Appl. Phys. Lett. 79, 2743-2745 (2001).

[3] J. Grabowska, A. Meaney, K. K. Nanda, J. -P. Mosnier, M. O. Henry, J. -R. Duclere and E. McGlynn, Phys. Rev. B 71, 115439 (2005).

[4] J. Zhang, Y. Liu, Y. Ke, and H. Yan, Nano Lett. 6, 248 (2006).

[5] L. Berti and G. A. BurLey, Nat. Nanotechnol. 3, 81 (2008).

[6] G. Springholz, V. Holy, M. Pinczolits, G. Bauer, Science 282, 734 (1998); E. R. Glaser, B. R. Bennett, B. V.Shanabrook, R. Magno, Appl. Phys. Lett. 68, 3614(1996); M. Grundmann et al., Phys. Rev. Lett. 74, 4043(1995).

[7] S. Facsko, T. Dekorsy, C. Koerdt, C. Trappe, H. Kurz, A. Vogt, H. L. Hartnagel, Science 285, 1551 (1999).

[8] Fujishima, T.N. Rao, and D.A. Tryk, J. Photochem. Photobiol. C, 1,1 (2000).

[9] Li D, Haneda H., Chemosphere. Apr; 51 (2): 129-37 (2003).

[10] M. Qamar, M. Muneer, Desalination 249, 535-540 (2009).

[11] Kwang-Soon Ahn, Yanfa Yan, Sudhakar Shet, Kim Jones, Todd Deutsch, John Turner, and Mowafak Al-Jassim, Appl. Phys. Lett. 93, 163117 (2008).

[12] Yu Q, Cao C., J Nanosci Nanotechnol. 2012 May;12(5):3984-9.

[13] Franco Decker, J. F. Juliò, and M. Abramovich, Appl. Phys. Lett. 35, 397 (1979)

[14] B. Karunagaran, Periyayya Uthirakumar, S.J. Chung, S. Velumani, E.K. Suh, Materials Characterization 58 (2007) 680-684.

[15] Qi Qi, Tong Zhang, Qingjiang Yu, Rui Wang, Yi Zeng, Li Liu, Haibin Yang,Sensors and Actuators B 133 (2008) 638-643

[16] N. Huang, Y.R. Chen, J.M. Luo, J. Yi, R. Lu, J. Xiao, Z.N. Xue, and X.H. Liu, J. Biomater. Appl. 8, 404 (1994).

[17] A.L. Linsebigler, G.Q. Lu, and J.T. Yates, Chem. Rev. 95 (1995) 735.

[18] M. Stomme, A. Guatarra, G. A. Niklasson, abd C. G. Granqvist, J. Appl. Phys. 79 3749 (1996).

[19] C. C. Hsieh, K. H. Wu, J. Y. Juang, T. M. Uen, J. Y. Lin, and Y. S. Gou, J. Appl. Phys. 92 2518 (2002).

[20] H. Matsui, H. Tabata, N. Hasuike, H. Harima, and B. Mizobuchi, J. Appl. Phys. 97 123511 (2005).

[21] D. Caiteanu, E. Gyorgy, S. Grigorescu,I. N. Mihailescu, G. Prodan, and V.Ciupina Appl. Surf. Sci. 252 4582 (2006).

[22] E. Gyorgy, A. P. Pino, G. Sauthier, A. Figueras, F. Alsina, and J Pascual, J.Phys. D: Appl. Phys. 40 (2007) 52465251.

[23] Y. Gao, S. Thevuthasan, D. E. McCready, and M. Engelhad, J. Cryst. Growth 212 178 (2000).

[24] G Perillat-Merceroz, P H Jouneau, G Feuillet, R Thierry, M Rosina and P Ferret, J. Phys.: Conf. Ser. 209, 012034 (2010).

[25] D. S. Bohle, and C. J. Spina, J. Am. Chem. Soc. 129, 12380 (2007).

[26] B. S. Liu, X. J. Zhao, Q. N. Zhao, X. He, and J. Y. Feng, J. Electron Spectrosc. Relat. Phenom. 148, 158 s(2005).

[27] M.T. Carter, M. Rodriguez, A.J. Bard, J. Am. Chem. Soc. 111 (1989) 8901-8911; A.J. Bard, X.H. Xu, J. Am. Chem. Soc. 117 (1995) 2627-2631.; S.R. Mikkelsen, K.M. Millan, Anal. Chem. 65 (1993) 2317; S.R. Mikkelsen, K.M. Millan, A. Saraullo, Anal. Chem. 66 (1994) 2943; J. Wang, X. Cai, G. Rivas, P. Farias, Anal. Chem. 68 (1996) 2629; J. Wang, E. Palecek, P. Nielsen, G. Rivas, X. Cai, H. Shiraishi, N. Dontha, D. Luo, P. Farias, J. Am. Chem. Soc. 118 (1996) 7667; J. Wang, P.E. Nielsen, M. Jiang, X. Cai, J.R. Fernades, D.H. Grant,M. Ozsoz, A. Beglieter, M. Mowart, Anal. Chem. 69 (1997) 5200; J. Wang, M. Jiang, W.N. Thor, C.G. Robert, J. Am. Chem. Soc. 120(1998) 8281; J. Wang, G. Rivas, M. Jiang, X. Zhang, Langmuir 15 (1999) 6541; P.C. Pandey, H.H. Weetall, Anal. Chem. 66 (1994) 1236; D.J. Caruana, A. Heller, J. Am. Chem. Soc. 121 (1999) 769; Y.D. Zhao, D.W. Pang, Z.L. Wang, J.K. Cheng, J. Electroanal. Chem.431 (1997) 203; P.M. Armistead, H.H. Thorp, Anal. Chem. 72 (2000) 3764; and H. Lee, S.K.R. Williams, S.D. Allison, T. J. Anchordoquy, Anal.Chem. 73 (2001) 837.

[28] N. Dhiman, R. Bonilla, D. O Kanej, G.A. Poland, Vaccine 20, 22-30 (2002).

[29] L.K. Adams, D.Y. Lyon, P. J. J. Alvarez; Water Res., 40, p. 3527 (2006).

[30] L. Zan, W. Fa, T. Peng, Z.k. Gong; J. Photochem. Photobiol. B, 86, p. 165 (2007).

[31] Roger J. Narayan, Nancy A. Monteiro-Riviere, Robin L. Brigmon, Michael J. Pellin, Jeffrey W. Elam, J Miner Met Mater Soc, 61, 6, 12 (2009).

[32] K. Keren, M. Krueger, R. Gilad, G. Ben-Yoseph, U. Sivan, and E. Braun, Science 297, 72 (2002).

[33] L.C. Feldman, J.W. Mayer and S.T. Picraux In: Material Analysis By Ion Channeling, Academic Press, New York (1982), p. 1.1.

[34] U. Littmark, J. F. Ziegler, “Handbook of Range Distributions for Energetic Ions in All Elements”, Vol. 6, Pergamon Press, New York (1980); J. F. Ziegler, “Handbook of Stopping Cross Sections for Energetic Ions in All Elements”, Pergamon Press, 1980; and J. F. Ziegler, J. P. Biersack, U. Littmark, Proceedings of the US-Japan Seminar on Charged Particle Penetration Phenomena, ORNL report CONF820131 (1982), p.88.

[35] J. P. , L. G. Haggmark, The Transport and Ranges in Matter. Nucl Instrum. Meth 174, 257 (1980), Available from www.srim.org.

[36] P. Sigmund, Ion Sputtering by Particle Bombardment, I , R. Behrisch, ed. (Springer-Verlag: Berlin (1981)).

[37] Z.L. Liau, J.W. Mayer, W.L. Brown, J.M. Poate: J. Appl. Phys. 49, 5295 (1978).

[38] Andersen H H and Bay H L, Radiat. Eff. 19, 139 (1973), J. Appl. Phys. 46 2416 (1975).

[39] G. Carter, B. Navinsýek, L. Whitton, in Sputtering by Particle Bombardment II, vol. 64 of Topics in Applied Physics, R. Behrisch, Ed. (Springer-Verlag, New York,1991), pp. 231.

[40] E. Chason, T. M. Mayer, B. K. Kellermann, D. E. McIlroy, and A. J. Howard, Phys. Rev. Lett. 72, 3040 (1994).

[41] G. Carter and V. Vishnyakov, Phys. Rev. B 54, 17647 (1996).

[42] T. M. Mayer, E. Chason, A. J. Howard, J. Appl. Phys. 76, 1633 (1994).

[43] S. Rusponi, C. Boragno, U. Valbusa, Phys. Rev. Lett.78, 2795 (1997); S. Rusponi, G. Constantini, C. Boragno, U. Valbusa, ibid. 81, 4184 (1998).

[44] Munoz-Garcia J, Vazquez L, Cuerno R, Sanchez-Garcia J A, Castro M and Gago R, Lecture Notes on Nanoscale Science and Technology: Self-Organized Surface Nanopatterning by Ion Beam Sputtering, Ed. Z Wang (Berlin: Springer) (Preprint 0706.2625).

[45] S. Rusponi, G. Constantini, C. Boragno, and U. Valbusa, Phys. Rev. Lett.81,4184 (1998).

[46] S. Habenicht, W. Bolse, K. P. Lieb, K. Reimann, and U. Geyer, Phys. Rev. B 60, R2200 (1999).

[47] G.W. Lewis, M.J. Nobes, G. Carter, and J.L. Whitton, Nucl. Instr. Meth. 179, 363 (1980).

[48] R. M. Bradley and J. M. E. Harper, J. Vac. Sci. Technol. A 6, 2390 (1988).

[49] Navez M., Chaperot D. and Sella C., C R Hebdomadaires Seances Acad Sci 254, 240 (1962).

[50] Erlebacher J.D. and AzizM.J., Mater Res Soc Symp Proc 440, 461-466 (1997).

[51] Habenicht S. Phys Rev B 63, 125419 (2001).

[52] Makeev M.A., Cuerno R. and Barabasi A.-L., Nucl Instrum Meth B 197, 185-227 (2002).

[53] Valbusa U., Boragno C. and de Mongeot F.B., Mater Sci Engrg C 23, 201-209 (2003).

[54] Brown A.D., Erlebacher J., Chan W.L. and Chason E., Phys Rev Lett 95, 056101 (2005); Brown A.D. and Erlebacher J., Phys Rev B 72, 075350 (2005).

[55] T. Bobek, S. Facsko, T. Dekorsy, H. Kurz, Nucl. Instr. and Meth. in Phys. Res. B 178 (2001) 101.

[56] Sigmund P. , J Mater Sci 8, 1545 (1973).

[57] Peter Sigmund, Phys. Rev. 184, 383 (1969).

[58] R. Cuerno and A.-L. Barabasi, Phys. Rev. Lett. 74, 4746 (1995); R. Cuerno et al., ibid. 75, 4464 (1995).

[59] Y. Kuramoto and T. Tsuzuki, Prog. Theor. Phys. 55, 356 (1976).

[60] Rodolfo Cuerno, Hernan A. Makse, Silvina Tomassone, Stephen T. Harrington, and H. Eugene Stanley; Phys. Rev. Lett. 75, 4464(1995)

[61] Martin Rost and Joachim Krug; Phys. Rev. Lett. 75, 3894(1995).

[62] S. Park, B. Kahng, H. Jeong, and A.-L. Barabasi; Phys. Rev. Lett. 83, 3486(1999).

[63] T. Paunesku, T. Rajh, G. Wiederrecht, J. Maser, S. Vogt, N.A. Stojicevic, M. Protic, B. Lai, J. Oryhon, M. Thurnauer, and G. Woloschak; Nat. Mater., 2 (2003), pp. 343-346

[64] W.C.-W. Chan, S.M. Nie; Science, 281 (1998), pp. 2016-2018

[65] T.A. Taton, C.A. Mirkin, R.L. Letsinger, Science, 289 (2000), pp. 1757-1760

[66] S. J. Park, T.A. Taton, C.A. Mirkin; Science, 295 (2002), pp. 1503-1506

[67] Y. Wei, C. Cao, R. Jin, C.A. Mirkin; Science, 297 (2002), pp. 1536-1540

[68] Po-Hsun Lo, S. Ashok Kumar, and Shen-Ming; Colloids and Surfaces B: Biointerfaces 66 (2008) 266.

[69] I. Iavicoli, Leso, L. Fontana, A. Bergamaschi, European Review for Medical and Pharmacological Sciences, 15, 481-508 (2011).

[70] B. Kasemo, J. Lausmaa; Int. J. Oral. Maxillofac. Implants, 3 (1988), pp. 83.

[71] Sverjensky, D.A., Jonsson, C.M., Jonsson, C.L., Cleaves, H.J., and Hazen, R.M.; Environ. Sci.Technol. 42:6034-6039 (2008).

[72] Kim E K, Lee H Y, Moon S E, Park J, Park S J, Kwak J H, Maeng S, Park K H, Kim J, Kim S W, Ji H J, Kim G T, J Nanosci Nanotechnol. 8(9), 4698-701 (2008).

[73] Jin Suk Kim, Won Il Park, Chul-Ho Lee and Gyu-Chul Yi, Journal of the Korean Physical Society, 49(4), 0, (2006).

[74] A. Eftekhari, F. Molaei, and H. Arami; Mater. Sci. Eng. A 437 (2006) 446.

[75] W. Sun, Z. Zhai, D. Wang, S. Liu, K. Jiao, Bioelectrochemistry 74 (2009) 295.

[76] J. Liu, C. Guo, C.M. Li, Y. Li, Q. Chi, X. Huang, Electrochem. Commun. 11 (2009) 202.

[77] X. Liu, Q. Hu, Q. Wu,W. Zhang, Z. Fang, Q. Xie, Collod. Surf. B: Biointerfaces 74 (2009) 154.

[78] A. Paul Alivisatos, Kai P. Johnsson, Xiaogang Peng, Troy E. Wilson, Colin J. Loweth, Marcel P. Bruchez Jr, and Peter G. Schultz, Nature, 382 (609) 1996.

[79] Jeffrey L. Coffer, Shelli R. Bigham, Xin Li, Russell F. Pinizzotto, Young Gyu Rho, Robert M. Pirtle, and Irma L. Pirtle, Appl.Phys.Lett. 69 (3851) 1996.

Chapter 2

Experimental Techniques

2.1 Introduction

The present thesis explores the formation of TiO_2, ZnO, and Hg nanostructures and their interaction with DNA. The nanostructures have been fabricated by a variety of methods and have been investigated using techniques like X-ray Photoelectron Spectroscopy (XPS), Atomic Force Microscopy (AFM), Ultra Violate - Visible Spectroscopy (UV-Vis) etc. The techniques of ion irradiation through Electron Cyclotron Resonance (ECR) source as well as a Low energy Ion source, in UHV, have been utilized to create crystalline nanostructures on single crystals of TiO_2. ZnO nanostructures, here, have been produced through Physical Vapor Deposition (PVD) technique. The mercury (Hg) nanostructures have been fabricated within the DNA double strand through the conjugation of the Hg salt with plasmid DNA. The interaction of TiO_2 and ZnO nanostructures with DNA have also been investigated here.

In section 2.2, we will discuss the experimental techniques related to Ion irradiation and Physical Vapor Deposition. Section 2.3 discusses the various characterization techniques utilized in this thesis. Structures of TiO_2, ZnO, Mercury (Hg), and DNA are discussed in section 2.4.

2.2 Ion Irradiation Techniques:

2.2.1 Ion irradiation with ECR source

The low energy keV ion irradiation of TiO_2 (110) samples was performed using an Electron Cyclotron Resonance (ECR) ion source at NIMS, Tsukuba, Japan. This is also called the *hot-plasma* ion source. The ultra high vacuum (UHV) ECR dry etching system (Shimadzu system, type SLEC-050S) was used for creating patterns on TiO_2 (110) surfaces. The schematic diagram of the sputtering setup is shown in fig. 2.1 [1]. The system consists of an ECR plasma section and an etching section separated by two grids and a load-lock section.

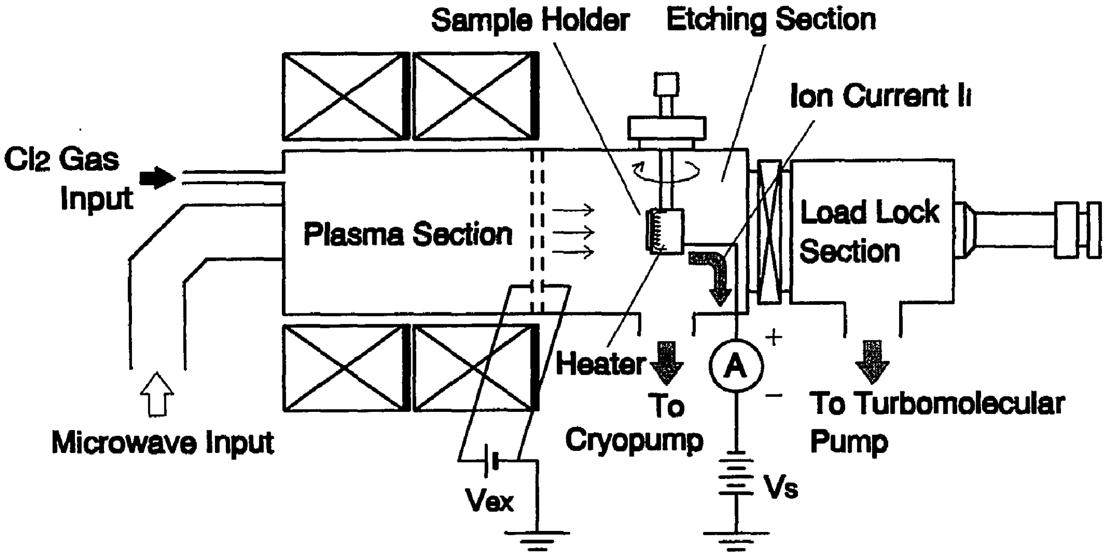

Figure 2.1: Operation and Schematic illustration of the ECR ion source set up (from Ref. [1])

In principle, when electrons move in a magnetic field (B) they gyrate around the magnetic field lines due to the Lorentz force. The gyration frequency is called the cyclotron frequency ω_{cyc}. If simultaneously an external microwave radiation of the same frequency

(ω_{hf}) propagates into such a region, the electrons are resonantly accelerated or decelerated depending on the phase of their transversal velocity component with respect to the electric field vector. This needs to fulfill a condition called the electron cyclotron resonance condition which states:

$$\omega_{hf} = \omega_{cyc} = \frac{e}{m} \cdot B \tag{2.1}$$

where, e and m are the charge and mass of the electron, respectively. The plasma electrons are confined in a superposition of an axial magnetic field component (produced by solenoids or permanent magnets) and the radial magnetic field of a multipole magnet. This results in a so-called *minimum* - B-structure [2] because the magnetic field has a minimum in the middle of the structure and from there increases in all directions. Thus, a closed surface is created where the electron cyclotron resonance condition is fulfilled and electrons passing through that surface can be accelerated resonantly. Furthermore, a high mirror ratio (the maximum field strength divided by the minimum field strength) of the magnetic field results in long confinement time for the plasma electrons. These electrons can pass the resonance region very often and gain high energies, which ionize plasma atoms and ions into high charge states via successive single ionization process.

In general owing to their large mass, the ions in the plasma do not get accelerated, and hence remain in thermal condition. Therefore they are not confined by the magnetic field but by the space charge potential of the electrons. This magnetic confinement, however, is not perfect and electrons can leave the plasma, for example in axial direction. Since the plasma tends to stay neutral, ions will effectively follow the electrons. By using a suitable extraction geometry and by applying a high voltage, these ions can be finally extracted from the ion source. The fig. 2.2 shows the simulation of Ar^+ ion beam inside the ECR. The accelerated beam quality is determined by the parameters like extraction voltage and geometry, intensity, magnetic field in the extraction region, etc. After the extraction (at +10kV), the beam widens up because of space charging. However, finally the beam is focused by using an additional ion-optical slit alignment.

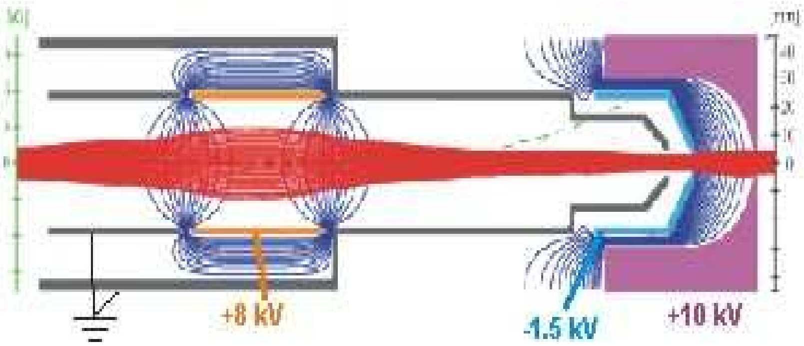

Figure 2.2: Simulation of an argon ion beam

2.2.2 Ion irradiation using Low Energy Ion Source in UHV

The ion irradiation of $TiO_2(110)$ surfaces was also performed by using Ar ion source (model EX03) from Thermo Scientific corporation. The detailed schematics of the Ar ion sputtering setup is given in fig. 2.3. The EX03 ion gun is an electron impact source which is designed to be used with the inert gases. This source is installed in a UHV system with a vacuum of 10^{-11} Torr. The vacuum is achieved by utilizing the ion, turbo (70 liter/sec), and rotary pumps.

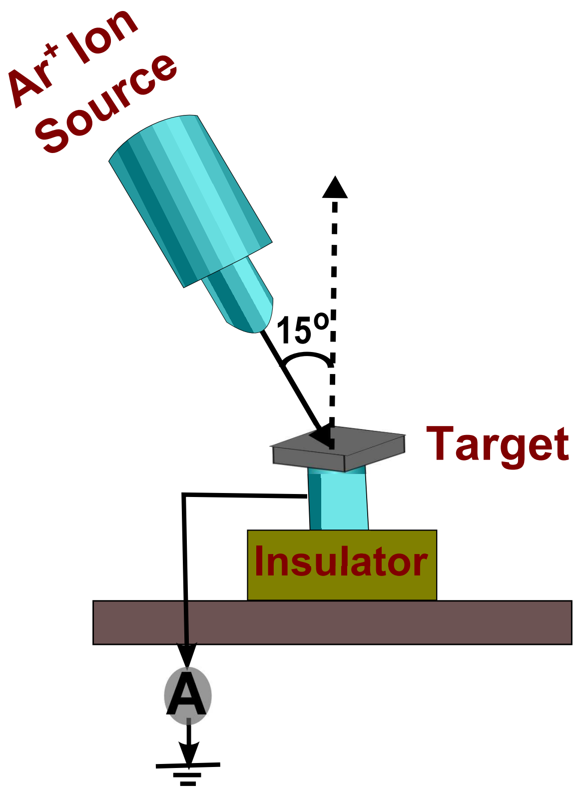

Figure 2.3: Schematic diagram of irradiation with Ar^+ ion source.

The general function of the EX03 ion gun is to ionize gas atoms in the source region of the ion gun, accelerate them and transfer these ions to the sample via the lens column. Ions are produced at a high positive potential and are accelerated through the gun to produce a beam of energy between 500eV - 3keV ions. Gas is fed directly into the source region at a higher pressure relative to the surrounding system. One of the two filaments within the source region is heated to emit electrons. The electrons are accelerated in the source cage to an energy called the electron energy. The electrons traverse the source cage and collide with gas atoms removing negatively charged electrons and leaving the gas atoms positively charged (IONS). The target current is adjustable in the range from $10\mu A$ to 20 μA. Ions produced in the source region are accelerated through an aperture in the extractor lens element by the positive potential. The beam is then shaped and focused onto the sample with control being given to the focus lens potential to vary the diameter of the ion beam.

The beam current measures the number of ions striking the target and is dependent on the several factors, but essentially can be controlled by the pressure and emission current. The emission current is the electron current flowing from the filament to the source cage and gives an indication of the number of electrons flowing through the ionization region. The pressure determines the number of atoms within the ionization region. A schematic presentation of the EX03 ion gun system is shown in fig. 2.4.

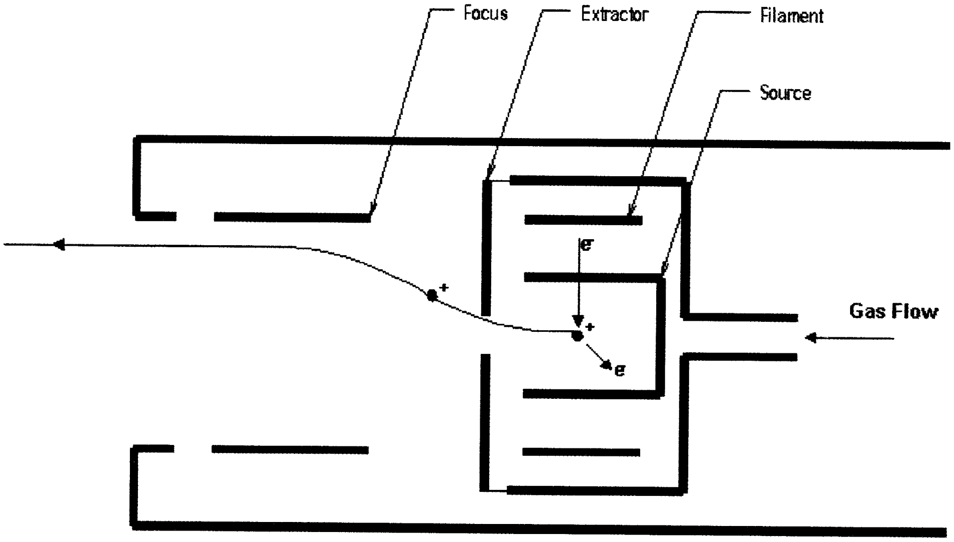

Figure 2.4: Schematic diagram of EX03 ion gun.

Utilizing the above setup the $TiO_2(110)$ single crystal surfaces were sputtered at an angle of 15°. The flux for the Ar ion source was 1×10^{13} ions/cm^{2}sec. The beam size was about 30mm in diameter.

2.2.3 Physical Vapor Deposition Technique

Physical Vapor Deposition (PVD) is a process to vaporize source material at certain temperature and condense the vapor phase source material to form the desired products like, thin films or nano scale objects. PVD can be induced using thermal evaporation, sputtering, cathodic arc discharge or laser ablation of the source material. Among all the synthesis methods, thermal evaporation is the most popular method because of the low cost and easy setup. The material to be evaporated, target, is usually evaporated by passing a high current through a highly refractory metal containment structure (e.g. a tungsten or graphite "boat"). This method is also called resistive heating. The cold water is circulated around the chamber to control the temperature of the boat. The physical vapor deposition has a limitation. In general, it is limited to elements or simple compounds whose vapor pressure ranges from 1 to 10^{-2} Torr, in the temperature interval from 600 to 1200°C. Inside the evaporation chamber, the mean free path of the vaporized gas species is (from kinetic molecular theory):

$$\lambda = \left(\frac{\pi RT}{2M}\right)^{\frac{1}{2}} \frac{\eta}{p} \tag{2.2}$$

where R is the ideal gas constant, T is the temperature, M is the mass of the evaporating specie, p is the pressure inside the chamber, and η is the gas viscosity respectively. The growth rate of the material (thin film), A on the substrate for a typical distance between substrate and target, d, in an evaporation chamber is (see fig.2.5):

$$A \propto \frac{\cos\theta \cdot \cos\phi}{d^2} \tag{2.3}$$

where, θ and ϕ are defined in fig. 2.5.

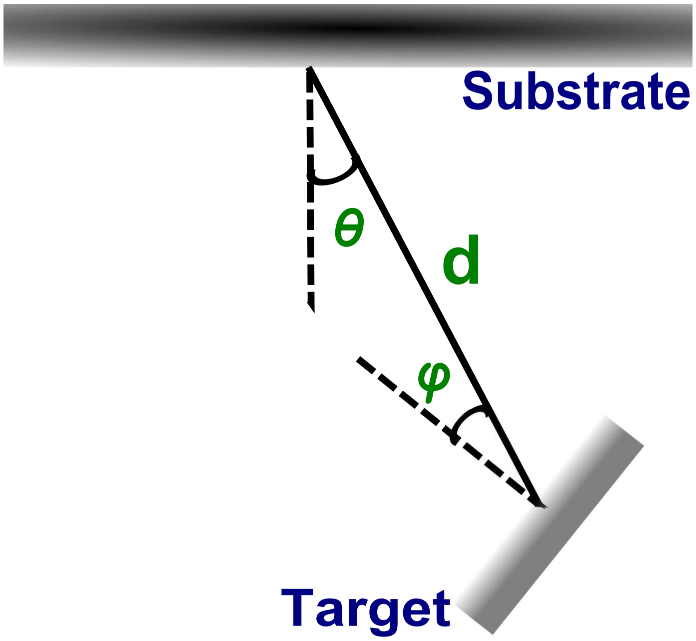

Figure 2.5: Geometry of target and substrate during evaporation

The ZnO films were deposited using Hind Hivac made thermal evaporator (model 12A4-D). This system consists of a thermal evaporator that uses an electric resistance heater to melt the material and raise the vapor pressure to a useful range. This is done in High Vacuum so that the vapor can reach the substrate without any scattering against other gas-phase atoms in the chamber. The most important requirement for thin film deposition is that the mean free path of the deposited material atoms must be greater than the distance between the source and the substrate. The material (preferably in powder form) to be deposited is placed in a Molybdenum boat. A large current is passed through the boat to heat it up so that the material gets melted and deposited on the substrate. The system has a cylindrical stainless steel vacuum chamber which is connected to the double stage pumping system. Pirani and Penning gauges are used to measure the vacuum level during the deposition. A Quartz Crystal Microbalance is used to measure the thickness of the deposited thin films. The working principle of the Quartz Crystal Microbalance is based on the Piezoelectric effect. The resonance frequency of oscillations is dependent on the mass of the film deposited onto it. The crystal can measure the thickness of film to nearly a single atomic layer with relatively high accuracy. The experimental setup of the Physical Vapor Deposition system is shown in fig. 2.6.

Figure 2.6: The Physical Vapor Deposition system.

2.3 Characterization Techniques

2.3.1 X-ray Photoelectron Spectroscopy (XPS)

X-ray photoelectron spectroscopy (XPS) is a spectroscopic technique which quantitatively measures the elemental composition, empirical formula, chemical state and electronic state of the compositional elements that exist in a material. Thus it is also abbreviated broadly as the *Electron Spectroscopy for Chemical Analysis* (ESCA). XPS spectra are obtained by irradiating a material with a beam of X-rays while simultaneously measuring the kinetic energy and number of electrons that escape from the top 1 to 10 nm of the material being analyzed. XPS requires ultra-high vacuum (UHV) conditions.

During 1887, in a pioneering work, **Heinrich Rudolf Hertz** first discovered the most interesting light -matter phenomena the *photoelectric effect* which was successfully explained later in 1905 by **Albert Einstein**. After several significant improvements **Kai Siegbahn** and his group in 1954 from Uppsala University (Sweden) developed and recorded the first high-energy-resolution XPS spectrum of the cleaved sodium chloride (NaCl) material [3]. Later in 1969, Siegbahn and his collaborators produced the first commercial monochromatic XPS instrument. In 1981, Siegbahn was recognized with the Nobel Prize to acknowledge his extensive efforts to develop the XPS techniques which has become a useful comprehensive analytical tool in all scientific fields in general [4]. Now it is widely used to measure the different physical and chemical entities of a material, whether in isolated or in composite form [5–10]. The key aspects of the XPS are:

- The elemental composition of the surface (top 1–10 nm usually)
- Elements that contaminate a surface
- Empirical formula of pure materials
- Chemical or electronic state of each element in the top region of the surface
- Uniformity of elemental composition across the outer most top surface (or line profiling or mapping)
- Uniformity of elemental composition as a function of ion beam etching (or depth profiling)

XPS has some limitations also. While it can detect all elements with an atomic number, $Z \geqslant 3$ (lithium). It can not detect the Hydrogen ($Z = 1$) or Helium ($Z = 2$) because of the short diameter of orbitals of these materials which reduce the emission probability to almost zero. Also, the detection limits for most of the elements are in the parts per thousand range. However in modern systems the detection limits can be approached to a parts per million (ppm) range, but again it requires special conditions like good concentration in the top surface layers and/or very long collection times.

In an atom the electrons are distributed in specific energy levels, and they have specific binding energies. When energetic X-rays strike the sample surface, the energy of the X-ray photon may gets completely absorbed by a core valance electron of the atom inside the sample (fig. 2.7).

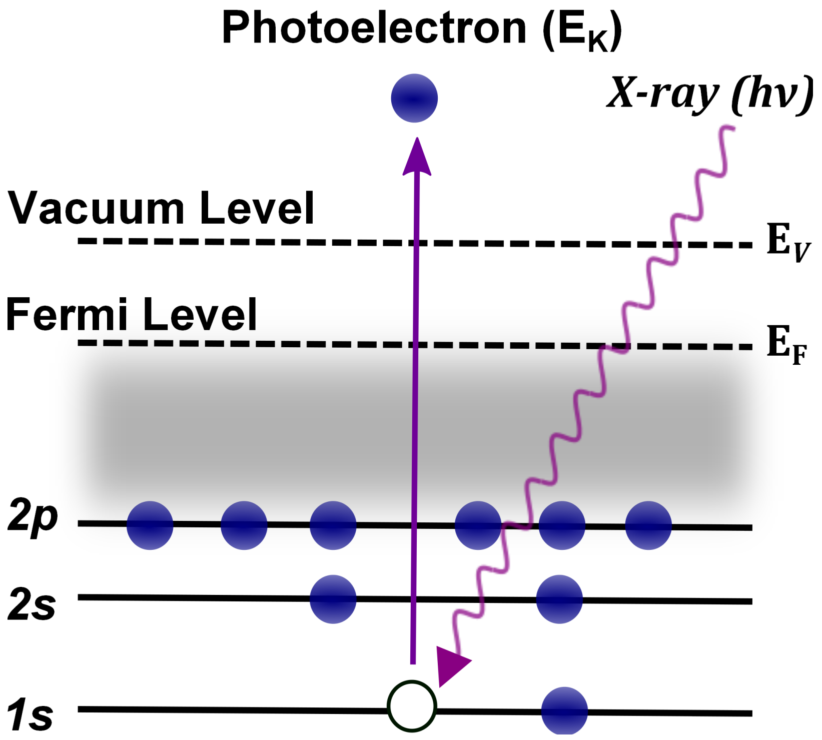

Figure 2.7: Schematic of core level X-ray photoelectron emission process

Now if the energy of the incident X-ray photon is higher than the binding energy of the electron of the atom, the electron can escape from the sample surface. The photoelectron gets emitted out with a kinetic energy (E_k). The binding energy (E_B) of this phototelectron can be evaluated by:

$$E_B = h\nu - E_K - \Phi_S \tag{2.4}$$

where, $h\nu$ is the incident X-ray photon energy, E_K is the kinetic energy of the emitted photoelectron (see fig. 2.8) , and Φ_S is the spectrometer work function. In fig. 2.8(b), the final energy of the emitted electron is dependant only on the spectrometer work function, since the spectrometer and the sample Fermi surfaces are at the same energy level during the measurement.

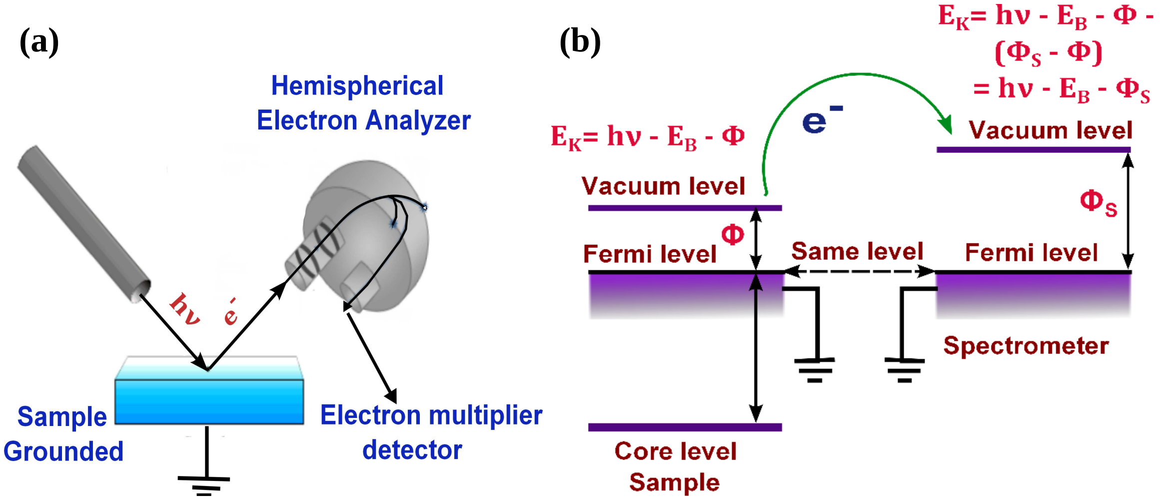

Figure 2.8: (a) The incident X-ray –surface interaction produces photoelectron, and (b) the typical schematic to evaluate the *Binding energy*, E_B of the electron inside the atom

X-ray photons can penetrate up to few micrometer below the surface. However, the inelastic scattering of the electrons in deep results in the background. The sharp XPS peaks are produced by photoelectron emitted by elastic scattering from the top (∼10nm) surface. This makes XPS a very surface sensitive characterization technique. The intensity of the emitted photoelectrons from an element is strongly dependent on the density of atoms of that specific element inside the material. Hence XPS technique can be utilized to quantify the chemical composition of the material. In a typical experiment for an element *i*, if the peak intensity after the background removal, is found to be I_i, the atomic concentration of the element, C_i can be evaluated as:

$$C_i = \frac{\frac{I_i}{S_i}}{\sum_i \frac{I_i}{S_i}} \tag{2.5}$$

where the term S_i is the atomic sensitivity factor, for the element i, and $\sum\limits_i$ is the summation over all elements.

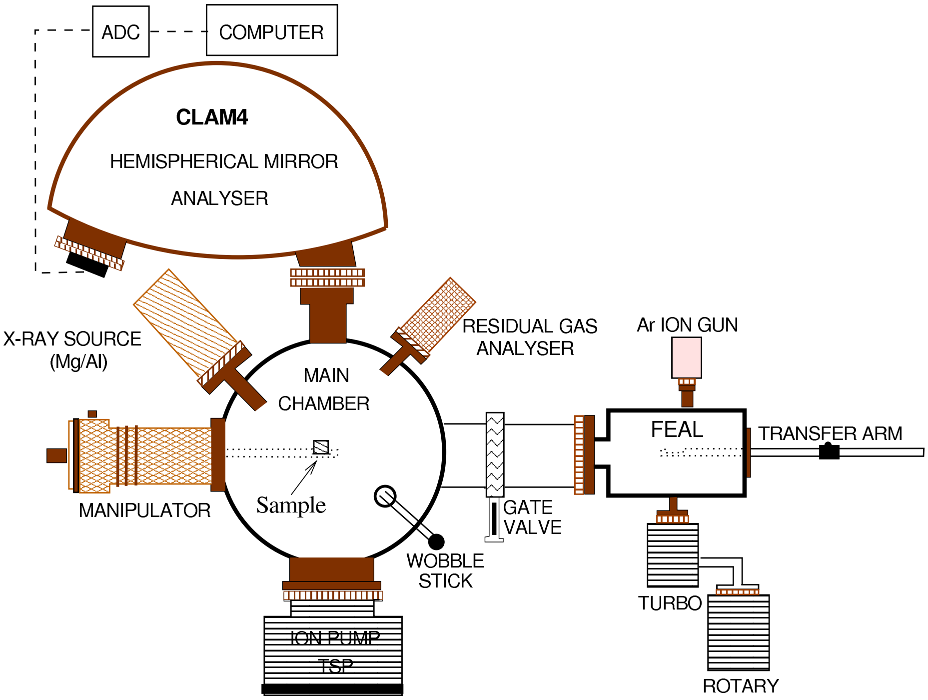

Figure 2.9: The schematic of the XPS setup in our laboratory

In the present thesis, the XPS experiments were done using a VG microtec system (the schematic of the system setup is shown in fig. 2.9). The base pressure of the main chamber is maintained at 1×10^{-10} *Torr*. The load lock chamber, as shown in the fig. 2.9, is equipped with an Ar ion gun. The XPS system is equipped with twin Mg-Al anodes, a hemispherical analyzer, and a channeltron unit. The dual anodes generate *non-monochromatic* X-ray emissions of energies 1253.6eV for Mg-K_α, and 1486.6 eV for the Al-K_α lines. Analyzer was operated with the pass energy of 200 eV for the large survey scans of $1-1000$eV, and 20eV for the higher resolution scans. The instrumental resolution of the setup is 0.9eV. The data were acquired at a 30° angle between the sample normal and the analyzer axis. The background (Shirley/Linear) was removed from the data and it was referenced with respect to the binding energy of the adventitious Carbon *1s* peak, positioned at 284.6 eV. The final spectra were fitted using the VGX-900 software to get the binding energy positions of the elements.

2.3.2 Transmission Electron Microscopy (TEM)

Transmission Electron Microscopy (TEM) is a microscopy technique, where a high energy beam of electrons is transmitted through an ultra thin specimen, interacting with the specimen as it pass through it. It is the most versatile instrument available for the examination and analysis of nanomaterials. TEM allows the observation and analysis of materials down to nanometer scale. In the present work high resolution transmission electron microscopy (HRTEM) with Resolution (i) Point to Point : 0.19 nm, and (ii) Lattice : 0.14 nm (make from JEOL, Model:2010 (UHR version with URP 22 Polepiece)) operating at 200keV was used. The system is equipped with an electron gun "LaB6" associated with the vacuum Pumps of rotary, diffusion and Ion. The standard procedure was followed to prepare the samples. The liquid nitrogen was used for imaging the DNA samples. The tilt angles is restricted to $15\,^\circ$C maximum. Two stages (1) Double tilt Cryo stage (LN_2 cooled) GATAN-636, and (2) Single tilt Hot stage (up to $1000\,^\circ$C) GATAN-628 UHR can be used for the characterization. The recording is done through conventional film camera, GATAN TV camera-622, and GATAN CCD Camera-832($4k \times 2k$). The data/images are acquired with (i) DT3152 image grabber card, and (ii) Digital Micrograph.

2.3.3 Field Emission Scanning Electron Microscope(FESEM)

A Field Emission Scanning Electron Microscope(FESEM) consists a gun with a field-emission cathode, which provides narrower probing beams at low as well as high electron energy, resulting in both improved spatial resolution and minimized sample charging and damage. In the present work an FESEM system (model S-4800, Manufacturer: Hitachi High-Technologies Corporation) with various resolutions of 1.0nm at 15kV (normal mode), 1.4nm at 1.0kV (retarding mode), and 2.0nm at 1.0kV (normal mode) was used. The electron beam gun is of ZrO/W field emission type with irradiation voltage of 0.5 to 30kV in normal mode, and 0.1 to 2.0kV in retarding mode. The system offer the magnifications from 20 to 800,000 range, with the sample stage moving area: X: 0 to 110mm, Y: 0 to 110mm, and Z: 1.5 to 40mm. It can handle samples with maximum size of 6”. The stage can rotate up to 360° and tilt from -5° to 70°. Both secondary electron and backscattering electron detectors are available for imaging. It features an image capture system for digital storage of images and image files can be transferred through network or USB drive.

2.3.4 Scanning Probe Microscopy (SPM)

Scanning Probe Microscopy (SPM) [11] is a family of microscopy techniques for studying surface structure, where a physical probe scans a surface and generate a 2 or 3 dimensional image of the surface with very high resolution. In the process of generating the surface topography, a probe mechanically moves over the surface making a raster scan line by line, and records the probe-surface interactions as a function of position. The different types of probe-surface interaction (tunneling current, inter-atomic force, magnetic force, electric force, frictional force) lead to different modes of the microscopy. In the early 1980’s two IBM scientists, G. Binnig and H. Rohrer [12, 13], developed the first technique for studying surface structure by probing the surface tunneling current which led to the technique of Scanning Tunneling Microscopy (STM). It is based on a quantum mechaniccal phenomena, where the electron go “right through” the barrier (potential gap), a process known as tunneling. When an electrical voltage V is applied between surface and the tip, this electron tunneling results in a net electrical current, the “tunneling current” I. This current depends on the tip to surface distance x, on the voltage V, and on the height of the potential barrier (work function) Φ, which can be evaluated approximately using the quantum mechanics:

$$I(x) = A \cdot eV \cdot exp\left(-\frac{\sqrt{8m\Phi}}{\hbar}x\right) \tag{2.6}$$

where m and e are the mass and charge of the electron respectively. Φ is the height of the barrier and is actually some mixture of the work functions of the tip and sample.

G. Binnig and H. Rohrer achieved the sub-atomic resolution in the surface imaging by using the STM technique, and for this pioneering contribution, they were awarded the Nobel prize in 1986. This invention was quickly followed by the development of a whole family of related techniques which, together with STM, are classified as Scanning Probe Microscopy (SPM).

An important feature of STM is the possibility to perform Scanning Tunnelling Spectroscopy (STS). To this end, the tunnelling current is measured as a function of gap voltage at a fixed tip position x. The feedback loop is opened to keep the tip at a constant distance, and the bias is ramped stepwise in the range of interest. The averaging time within one step influences the energy resolution of the spectrum. Such a special curve, $I(V)$, contains information about the local electronic structure of the sample.

The most important extension of the STM technique is the Atomic Force Microscopy (AFM), invented by G. Binnig, C. Quate, and C. Gerber [14]. The essential feature of this technique lies in the fact that it can image the surface topography even of a non-metal surfaces in the ambient environment, while for the STM technique the surface needs to be conductive in nature. In atomic force microscopy, a tip mounted on a cantilever is scanned over the surface. The topographic variations on the surface are detected due to the force acting between the atoms of the tip and the surface. The radius of curvature of the tip is usually between 10−50nm. A tip is typically made of silicon or silicon nitride, and is attached to a 100−200μm long cantilever. The silicon nitride tips are more flexible and less stiff than the silicon tips, which make them perfect for contact mode AFM imaging. The silicon tips are best suitable for the tapping mode AFM imaging.

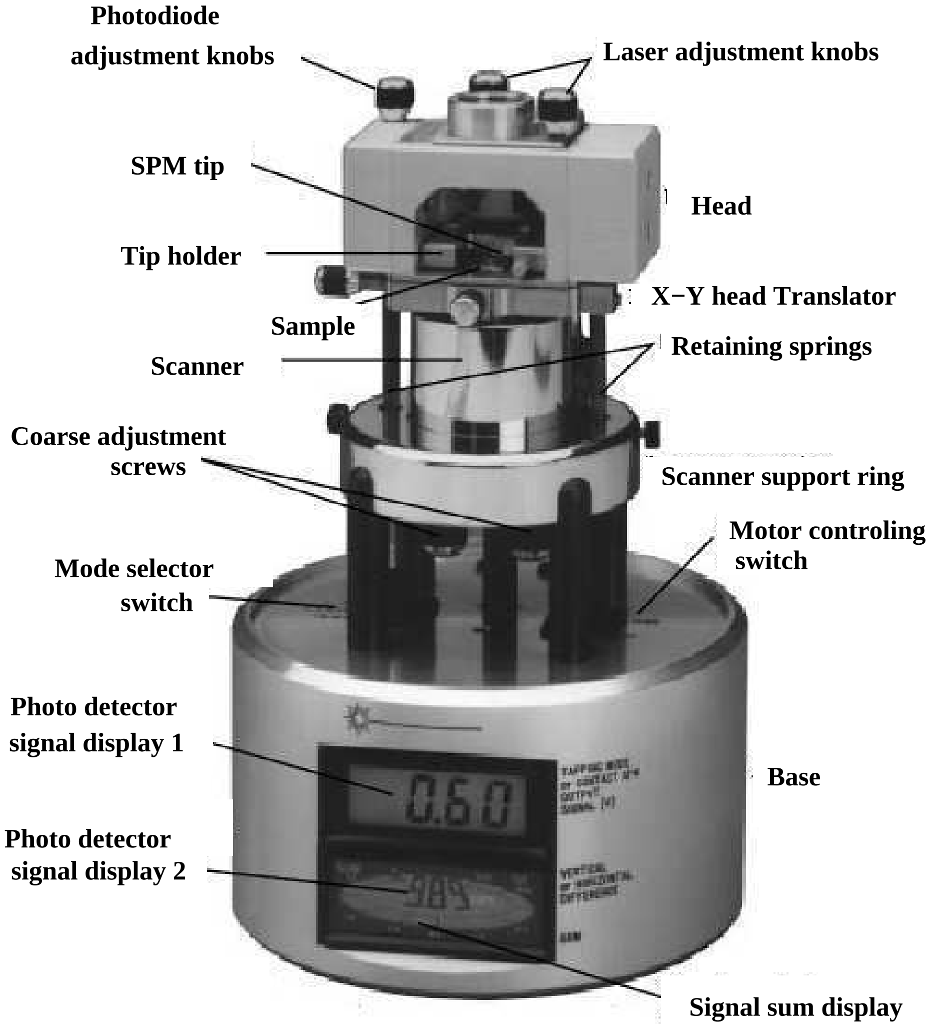

Figure 2.10: Multimode SPM in our laboratory

The main parts of AFM consists of Head, Scanner, and Base. The laser and photo diode are attached in the head. Tip holder is mounted to the head. The electronics adjustments are displayed in the base. The sample is attached on piezoelectric translators (PZT) (made of Lead Zirconium Titanate compound) and is scanned in x, y directions under the AFM tip. During the scan a feedback loop is used to maintain either a constant deflection (contact mode) or oscillatory amplitude (tapping mode) of the cantilever. A laser is focused onto the tip and is reflected back to a position-sensitive photo-detector. The force between the tip and the surface changes according to the sample topography resulting in a varying deflection of the cantilever. This is imaged by the deflection of the laser light. fig. 2.11 shows a schematic of the scheme used to image the surface topography using AFM.

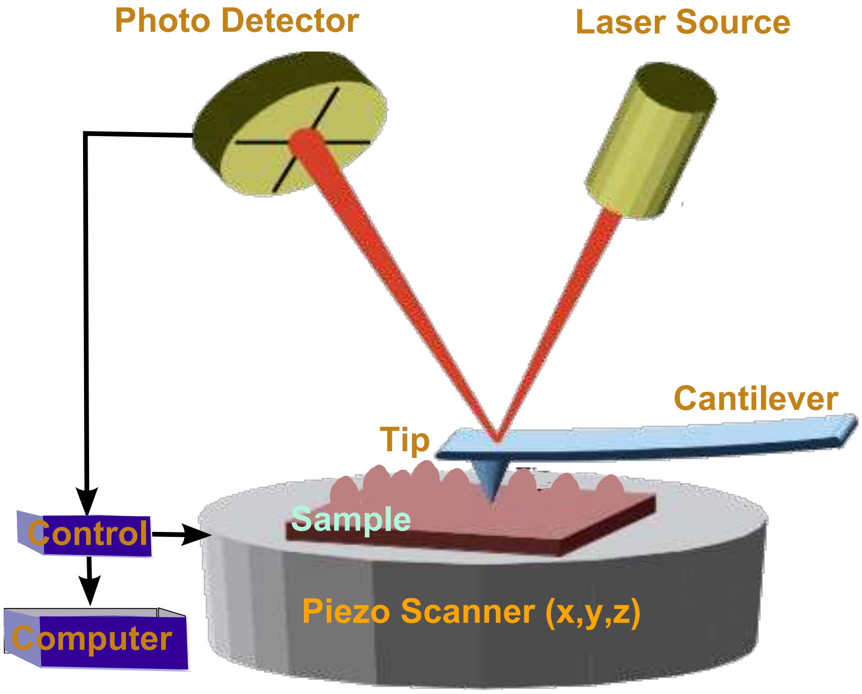

Figure 2.11: The schematic representation of the AFM operation

There are several types of forces acting between the atoms of the tip and the surface. Repulsive and Long range (Van der Waals (VdW) type) attractive interactions are most prominent. Other interactions like capillary, electrostatic, magnetic, polarization forces etc. are significantly dominant at long separations. In fig. 2.12 the tip−sample interaction force is represented through force−distance curve. Interatomic Lennard-Jones force $F(r)$ can be expressed as:

$$F(r) = -\frac{A}{r^7} + \frac{B}{r^{13}} \tag{2.7}$$

where, A, B are constant parameters, and r is the separation between tip and the sample.

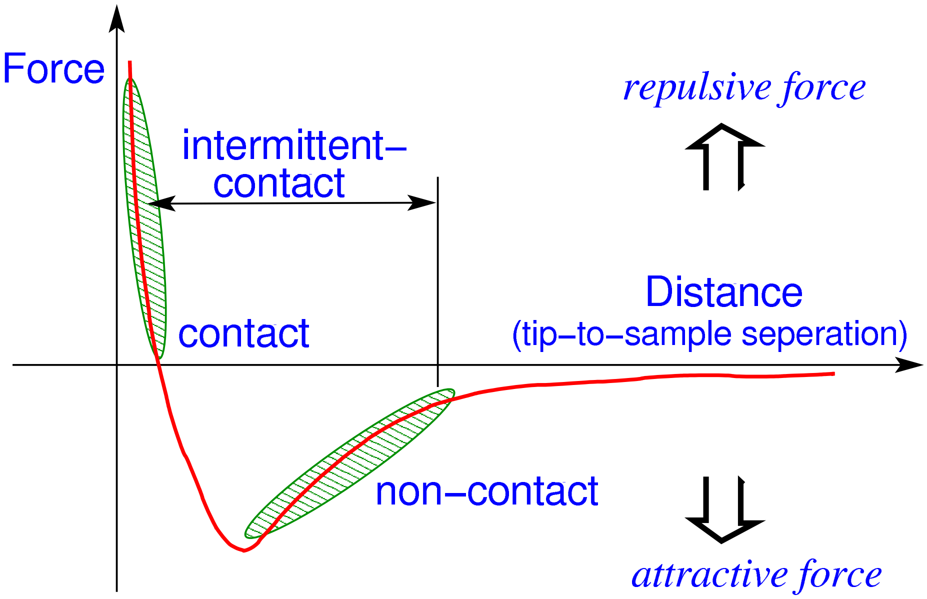

Figure 2.12: The graphical construction of an AFM force-displacement curve.

During contact with the sample, the probe predominately experiences repulsive forces (contact mode). As the tip moves further away from the surface the attractive forces are dominant (non-contact mode). Out of these two, varying repulsive interatomic force can offer very high resolution imaging of surfaces. Long range attractive forces pull the tip towards the sample surface and give rise to an increase in the local repulsive force which disturbs the motion of the tip and generates noise in the image. Thus it is important to minimize those long range forces in order to achieve very low repulsive forces (nano-Newton and less) in the contact area between tip and the sample. This is especially important for imaging of soft materials, which can be deformed or destroyed easily by the load of the tip.

With this nature of the interactions between the atoms of the tip and the surface, there are three modes of operation used in AFM. They are described below:

i. Contact mode operation :

In the contact mode, the tip makes soft "physical contact" with the sample surface. The deflection of the cantilever "δr" is linearly proportional to the force acting on the tip (F) and maintains the Hook's law, $F = -k\ \delta r$, where k is the spring constant of the cantilever. The system can be operated under constant height mode or constant force mode. In the constant height mode the height of the tip is fixed. The typical separation between the tip and the sample is < 0.5 nm. In the constant force mode the deflection of the cantilever is fixed and the motion of the scanner in z-direction is recorded. Since the tip traces across the surface gently, the constant force mode guides the cantilever to bend to accommodate the changes in the topography of the surface. Thus, contact mode is suitable for hard materials and not for soft materials, where the surface is very fragile. The tips mainly used for this mode are silicon nitride probes.

ii. Non-Contact mode operation :

In the non-contact mode of operation, the probe operates in the attractive force regime and the tip$-$sample interaction is minimized at a separation of $\sim$10 to 100 Å. The use of non-contact mode allows scanning the surface without influencing the shape of the sample by the tip-sample forces. The suitable cantilever for this kind of mode is the one having high spring constant of 20-100 N/m so that it does not stick to the sample surface at small amplitudes. The tips mainly used for this mode are silicon probes.

iii. Tapping mode operation :

The tapping mode of operation is the intermittent contact mode. Here in general a 0.5 to 2 nm of probe to surface separation is maintain. In this mode the cantilever tip is stimulated to vibrate near its resonance frequency ($\sim$ 300kHz). When the tip approaches to the surface, the vibration amplitude, the resonant frequency and the phase of the cantilever change due to the interaction force between the atoms of surface and the tip. Then, instead of scanning the sample at constant deflection, the surface is scanned at constant reduction of the oscillation amplitude and hence the tip does not remain in mechanical contact with the surface during the scan. The amplitude used for the feedback and the vertical adjustments of the piezoscanner are recorded as a height image.

The information on phase modifications is present in phase image. In the context of Magnetic Force Microscopy, a magnetic tip is utilized. The imaging is performed in tapping mode and the phase image provides the information regarding the magnetic domains.

Resolution of the AFM:

The resolution of the AFM mainly depends on the sharpness of the tip which can currently be manufactured with an end radius of a few nanometers. A close enough high resolution image can show that any AFM tip is rounded off. Hence the “end radius” of the tip is a vital parameter for getting a good resolution in the AFM experiments. In combination with tip-sample interaction effects, this end radius generally limits the resolution of AFM. In ideal conditions, on a freshly cleaved mica surface the AFM is capable to offer better than 3 Å in lateral resolution and of 0.1 Å resolution in height measurement.

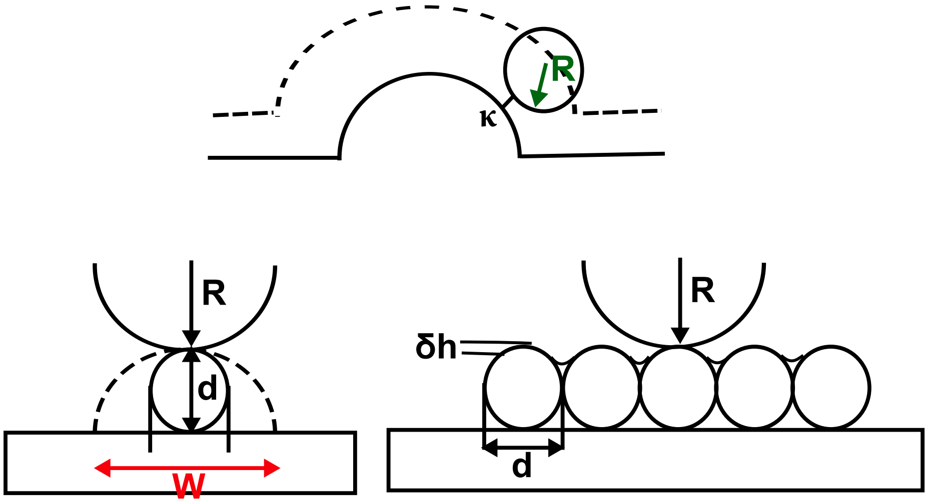

Figure 2.13: Dependency of AFM resolution on tip dimension

The dependency of the resolution of the tip is illustrated in fig. 2.13. If we consider the tip as a sphere of radius R to roll over a particle of radius $d/2$ on the surface, and if the interaction decay length $\kappa << R$, the tip geometry determines the resolution; in the most simple approximation the width of the resultant image of the particle scanned by the tip can be expressed as:

$$W = \sqrt{8d\left(R + \frac{d}{4}\right)} \tag{2.8}$$

The practical resolution, however, is also determined by the sensitivity of the height detector, i.e., the noise level.

Analysis of Power Spectral Density through AFM:

The Power Spectral Density (PSD) is the square norm of the Fourier transform of the AFM image taken on the surface, and it contains the information of the spatial distribution of the fluctuations over the surface across the multiple length scales. It basically represents the contribution of each spatial frequency to the topography of the surface. For an isotropic surface, one-dimensional PSD data is obtained by averaging the Fourier transformed AFM images taken in the fast scan direction (in our experiments x axis). For each scan length L, the spatial frequencies range between $1/L$ and the Nyquist frequency $N/2L$, where the image is scanned at N pixels. The mathematical form of the 1D-iso PSD can be represented in the following expression:

$$PSD(\nu) = \frac{1}{L}\left|\int_0^L dx\, h(x)\, e^{i2\pi\nu x}\right|^2 \tag{2.9}$$

Here ν is the spatial frequency, x is the fast axis direction, and $h(x)$ is the apparent topological height with respect to the mean height $<h> = 0$. The corresponding spatial wave vector to the spatial frequency can be written in the form, $\kappa = 2\pi\nu$.

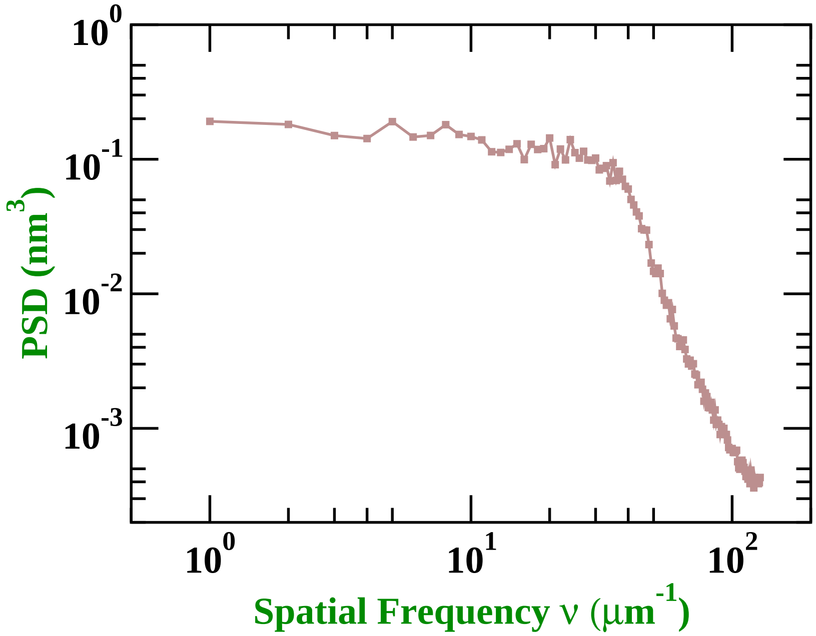

Figure 2.14: One dimensional isotropic *PSD* presentation for fast x axis scan.

A typical example of a PSD plot is shown in fig. 2.14. The PSD data is plotted against the spatial frequency ν. The PSD plot exhibits typical features consisting of a plateau at the low spatial frequencies and a decaying slope at high spatial frequencies. The inherent features of the PSD can be extracted by using the $k-$correlation model [15], which can be expressed as:

$$PSD(\nu) = \frac{A}{(1+B^2\nu^2)^{(C+1)/2}} \tag{2.10}$$

where, A, B, C are the function parameters. A is the magnitude at low spatial frequency, which is related to the height of the rough surface [16]. B relates the mean grain size, and C is the slope at high special frequencies, which provide information about correlations in the system.

In the present thesis, the surface topographies have been acquired using a multimode AFM (fig. 2.10) with nanoscope IIIa and V controllers from Digital Instrument (Bruker). All the images reported here were acquired in tapping mode with constant force mode. The Nanoscope software was used to analyze the images.

2.3.5 UV-VIS Spectroscopy :

In a molecule, the atoms overlap their atomic orbitals to form the molecular orbitals. These orbitals are occupied by the electrons of different energy levels. Upon the interaction with the external energy source, the ground state molecular orbitals can be excited to anti-bonding molecular orbitals. The electrons in the molecule can be of one of three types: namely σ (in single bond), π (in multiple-bond), or in non-bonding (*n*- caused by lone pairs). These electrons when imparted with external energy source can get excited from the *highest occupied molecular orbital* (HOMO) to the *lowest unoccupied molecular orbital* (LUMO) and the resulting species is known as the *excited or anti-bonding* state. The characteristic features of these electrons can be summarize below (see fig. 2.15):

- σ bond electrons: These type of electrons are the ground state, lowest energy level electrons and are the most stable electrons. They require a lot of energy to be displaced to the higher energy levels. As a result these electrons generally absorb light in the lower wavelengths of the ultraviolet light and these transitions are rare.

- π bond electrons: These type of electrons are already in higher energy levels of the ground state. They are relatively unstable and can be excited more easily and would require less energy for excitation. They would therefore absorb energy in the ultraviolet and visible light radiations.
- *n or non – bonding*: These electrons are generally electrons belonging to lone pairs of atoms. They are of higher energy levels than π electrons and can be excited by both the ultraviolet and visible light as well.

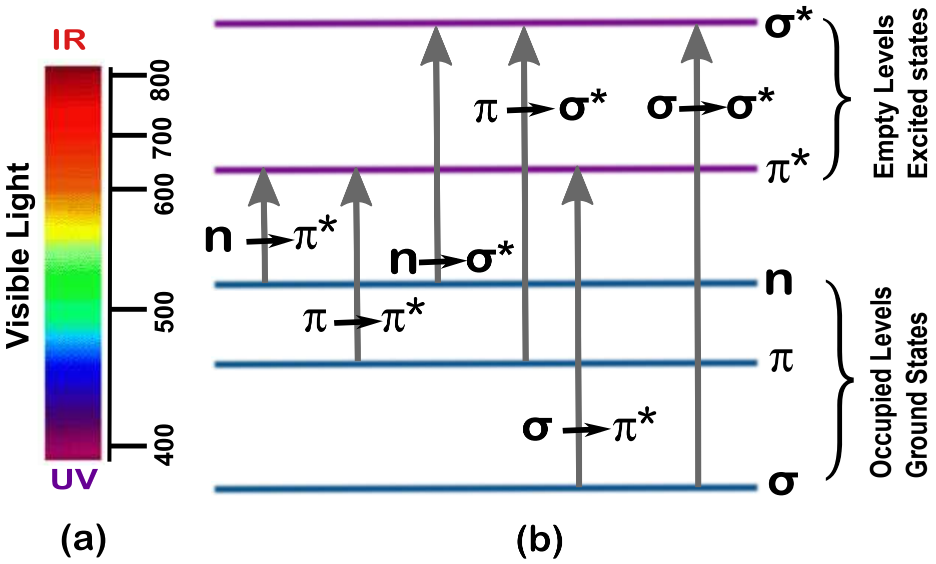

Figure 2.15: Different energy levels in a molecule and their possible transitions

The word “spectroscopy” is used as a collective term for all the analytical techniques based on the interaction of light and matter. “Spectrophotometry” is a one of the branches of spectroscopy for the absorption of light by ions or molecules which are either in gas or vapor state or the dissolved molecules/ions. Ultraviolet and visible (UV-Vis) absorption spectroscopy is the measurement of the attenuation of a beam of light after it passes through a sample or after reflection from a sample surface. In spectrophotometry, the absorption property of the different substances is measured within the wavelength ranges from 190 nm to 900 nm. The *visible spectroscopy* is restricted to the wavelength range of the electromagnetic radiation (easily detectable by the human eye), which is above 360 nm and the *ultraviolet spectroscopy* is used for the shorter wavelengths. Absorption of the electromagnetic radiation in the ultraviolate range by a substance is primarily caused by the electronic excitation i.e. the transition to a higher energy level from the lower binding level of the bonding and non-bonding electrons of the ions or molecules. A graphical presentation of absorbance against the wavelength gives the absorption spectrum of the substance. However, it is interesting to note, that the measured spectrum is continuous, which is due to the fact that the different vibration and rotation states of the molecules make the absorption band wider.

Absorption spectra is used for both qualitative and quantitative investigations of the substance electronic property. The wavelength at the maximum of the absorption will give information about the structure of the molecule or ion and the extent of the absorption is proportional with the amount of the species absorbing the light. The proposition of the absorption of the radiation by a medium is defined by two laws;

(a) *Lambert's law* : which states that the proportion of incident light absorbed by a transparent medium is independent of the intensity of the light (provided that there is no other physical or chemical change to the medium). Hence, successive layers of equal thickness will transmit an equal proportion of the incident energy.

(b) *Beer's Law* : which states, the absorption of light is directly proportional to both the concentration of the absorbing medium and the thickness of the medium in the light path.

Therefore, the quantitative measurements of the absorption by a medium can be combinedly expressed in the form, popularly known as the “Beer-Lambert Law” (which also known as “Lambert-Beer-Bouguer Law”) [18–20]. This expresses the linear relationship between absorbance and concentration of an absorbing species.

From the above, combinedly the "*Beer-Lambert*" law can be expressed as:

$$A = \varepsilon_\lambda \cdot c \cdot l = \alpha \cdot l \tag{2.11}$$

where, the term ε_λ is the wavelength dependant molar absorptivity coefficient with unit of $M^{-1}cm^{-1}$, c is the concentration of the compound in solution, expressed in $molL^{-1}$, and l is the path length of the substance, expressed in cm. The term α is the absorption coefficient of the substance.

For solid samples, if the incident radiation intensity is I_i and the intensity after it passes through the substance is I_o, then, the amount of radiation absorbed may be measured in a number of ways:

Transmittance, $T = I_o/I_i$, and the $\%T = 100T$

and the *Absorbance* (unit less) can be expressed in the form as:

$A = log_{10}I_i/I_o = -log_{10}T = 2 - log_{10}(\%T)$,

Measurement of the Electronic Bandgap of Semiconductor Materials :

In semiconductor material the conduction band is separated by the valance band by some bandgap energy "E_g". The term "band gap" refers to the energy difference between the top of the valence band to the bottom of the conduction band. In order for an electron to jump from a valence band to a conduction band, it requires a specific minimum amount of energy for the transition, which is called the band gap energy [21] . If the semiconductor material is exposed to some energetic radiation, it will show high absorption for the energies of radiation with energies $> E_g$, where as it will show no absorption for the radiation with energies $< E_g$. Hence near energies of E_g, the material will show a sharp increase of absorption of the radiation that manifests itself as an absorption edge (or "reflection threshold") in the UV-Vis absorbance spectrum.

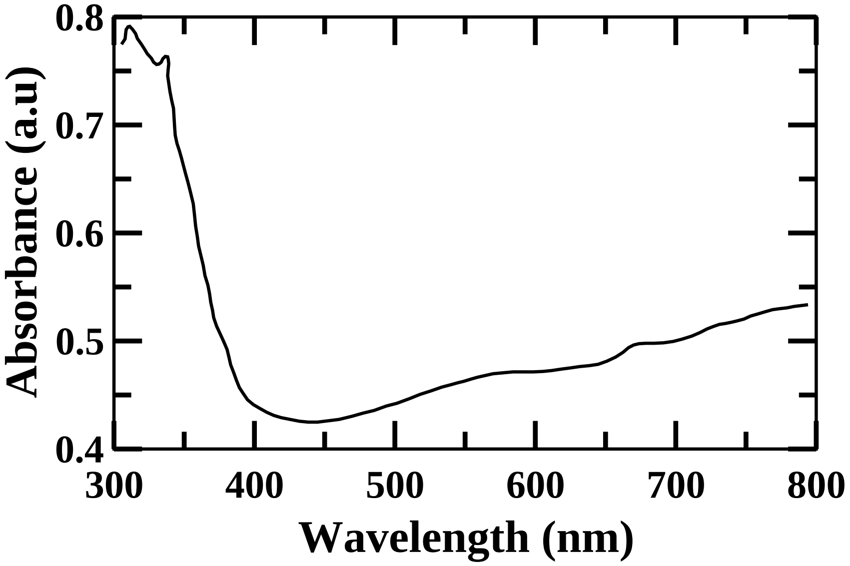

Figure 2.16: Example of a typical UV-Vis spectra for a material with E_g= 3.0 eV

A typical absorbance spectra is shown in fig. 2.16 for a material with bandgap energy $\sim$ 3.0eV, for which it can be seen the absorption edge occurs at about 400 nm. Thus, the absorbance spectra can play a vital role in evaluation of the bandgap energy of an unknown material. While the absoption edge can predict the approximate location of the bandgap energy of a material, the actual value can be estimated from a plot between absorption coefficient (α) and energy, called the *Tauc plot* [22]. Which can be expressed for direct and indirect bandgap material as:
for *Direct bandgap* material:

$$\alpha(h\nu) \propto \frac{\sqrt{h\nu - E_g}}{h\nu} \tag{2.12}$$

where, $h\nu$ is the incident external radiation energy, and the bandgap is the intercept of the straight line obtained by plotting $[\alpha(h\nu)]^2$ vs. $h\nu$.
and for *Indirect bandgap* material:

$$\alpha(h\nu) \propto \frac{(h\nu - E_g)^2}{h\nu} \tag{2.13}$$

where, $h\nu$ is the incident external radiation energy, and the bandgap of the semiconductor (direct or indirect) is the intercept of the straight line obtained by plotting $[\alpha(h\nu)]^{1/2}$ vs. $h\nu$.

In a double beam spectrometer, the radiation coming from the monochromator is split into two beams with the help of a beam splitter. These are passed simultaneously through the reference and the sample cell. The transmitted radiations are detected by the detectors and the difference in the signal at all the wavelengths is suitably amplified and sent for the output.

In this thesis, UV$-$Vis spectroscopy experiments were carried out using Perkin-Elmer Lambda 650 UV$-$Vis Spectrophotometer. In fig. 2.17 the schematics of the spectrophotometer is shown. The set up consists of two light sources, one is a deuterium arc discharge lamp which can generate high intensity radiation in the 190$-$380nm range (for UV range measurements), and another a tungsten-halogen lamp which can emits the radiation in the range from 320$-$900 nm (for visible range measurements). The instruments automatically swap lamps when scanning between the UV and visible regions. The wavelengths of these continuous light sources are typically dispersed by a SiO_2 coated reflecting optical system with holographic grating mono-chromator (1440 Lines/mm UV/Vis blazed at 240 nm). The spectral bandpass is then determined by the mono-chromator slit width or by the array$-$element width in array-detector spectrometers. Spectrometer designs and optical components are optimized to reject stray light, which is one of the limiting factors in quantitative absorbance measurements. The detector is the photomultiplier tube (PMT), R955, which can give high energy throughout in the whole UV/Vis range. The extreme resolution in the measurement offered by this system is ≤ 0.17 nm.

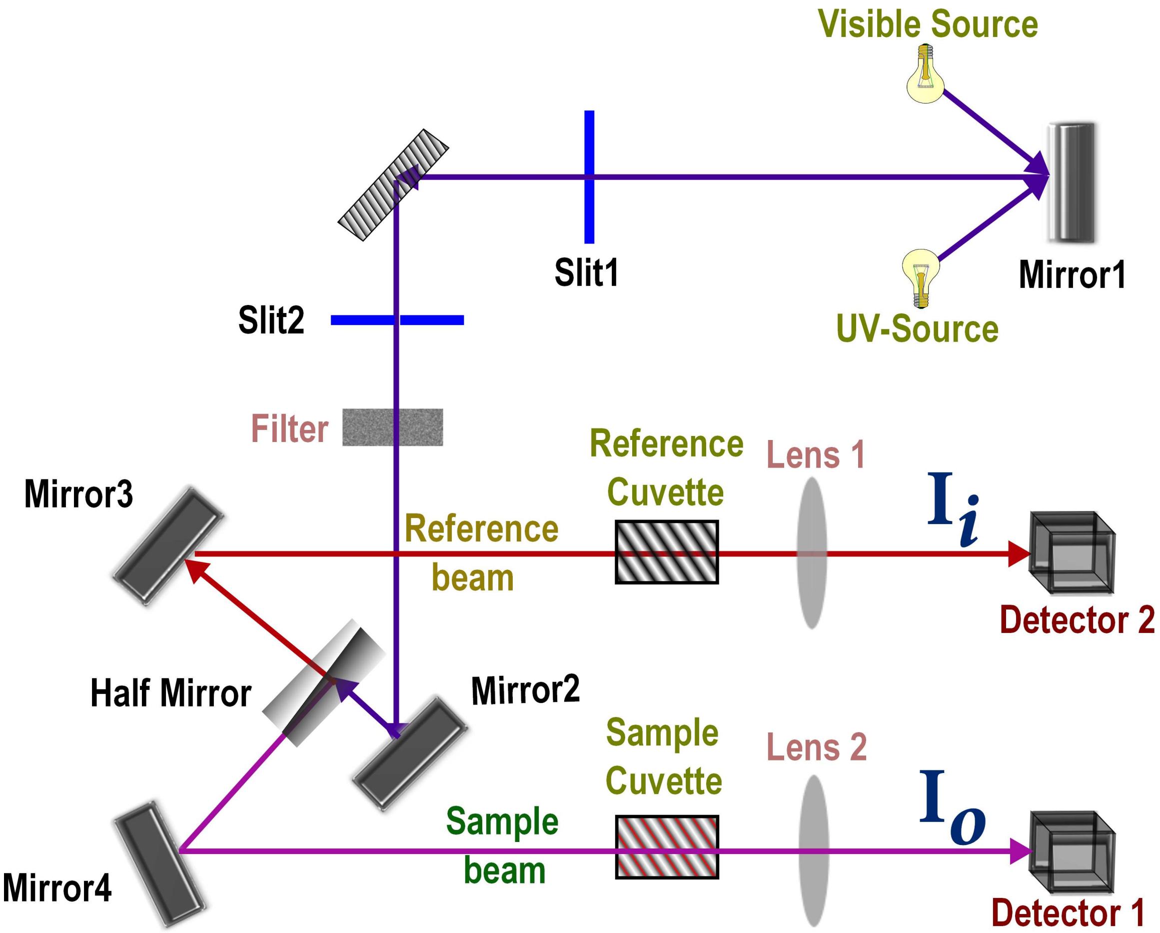

Figure 2.17: The schematic of UV−Vis spectroscopy set up

2.3.6 Magneto Optical Kerr Effect (MOKE):

Magnetic Anisotropies

The magnetic behavior of the thin films and nanostructures depends on the magnetic anisotropy phenomena. The origin of the spontaneous magnetism is explicitly related to the exchange interaction between the spins in the materials. The energy required to magnetize a demagnetized ferromagnetic material from saturated state depends on the direction of the external magnetic field. In a crystalline material, the magnetization prefers to orient itself along certain axes, and tries to avoid orienting itself along certain other axes. This tendency of a magnetic crystal to prefer certain orientations of its magnetization vector, that breaks the spherical magnetic symmetry of the free energy of the crystal is known as magnetic anisotropy. In a study by Mermin et al [23], it has been proved that this anisotropy is necessary in two dimensional ferromagnetic system to obtain the long range order of spin interaction.

In 1845 Michael Faraday observed the famous *Faraday effect*, where the polarization of the light is rotated through a transparent material subjected to a magnetic field. An analogous phenomena is also observed for a magnetic material, where the linearly polarized light which is reflected off magnetic materials alters the state of polarization of the light and its polarization rotates and becomes slightly elliptical. These effects are popularly known as the *Magneto Optical Kerr Effect* (MOKE) which were observed by John Kerr in 1887 [24, 25]. The magneto optical effects arise due to the *optical anisotropy* inside the materials. The source of this optical anisotropy is the magnetization M within the surface domains which can be influenced by the external magnetic fields. In a more descriptive way, the Kerr Effect is the coupling between the electric field of the light and the electronic spin of the magnetic domains originating from the spin-orbit coupling inside the magnetic material. Since the left and right polarized light have different directional electronic motion inside the medium, the interaction with the magnetic spin will be different for both the types of polarized lights.

It is obvious from the above discussion that, the magneto optical effects depend linearly on the magnetization. This makes it very useful in the study of surface magnetism since it is highly sensitive to the magnetization within the skin depth region, typically $10-20$nm in most metals [26]. The effect has been utilized to obtain hysteresis loops or domain images and is a relatively simple technique to implement.

Practical Measurement of the Kerr effect of thin films

The optical property of a medium is determined by its dielectric function, which is a tensor determined from the motion of the electrons in the medium. Thus the right and left circularly (electric field) polarized light will have different responses to the magnetic medium. When a linearly polarized light, (which is a combination of a left and right circular electric field polarization) propagates through a medium, in absence of any external magnetic field, the left polarized electric field will drive the electrons in the left circular direction and the right polarization electric field will drive the electron in the right circular direction, and both with the same radius of electron orbit. Since the electric dipole moment is proportional to the radius of the electron orbit, hence there will be no change in the dielectric constant of the medium, and so no Kerr rotation of the light.

Now, if after the magnetic field is applied to the medium, there will be an extra Lorentz force acting on each electrons, which points towards (outwards) the center of the radius of the left (right) circular motion. Thus effectively the radius of the left circular motion will decrease, while the right circular motion will increase, and the resultant polarization of the light after the magnetic field is applied will be elliptical. The axis of polarization (the major axis of the ellipse) is then rotated by an angle θ_k from the linearly polarized light, which is called the Kerr angle [27].

In a MOKE set up, the polarizer controls the polarization of the incident light, whereas the analyzer is used to produce an intensity variation at the photo detector from changes in the polarization. The Kerr angle θ_k is usually very small, and this only produces a very small change in the intensity. Since the relative change in the intensity due to the Kerr rotation is more important, the analyzer is generally set at an extinction angle (δ) to detect the Kerr rotation and this will be a maximum when the normal component of reflection is screened out.

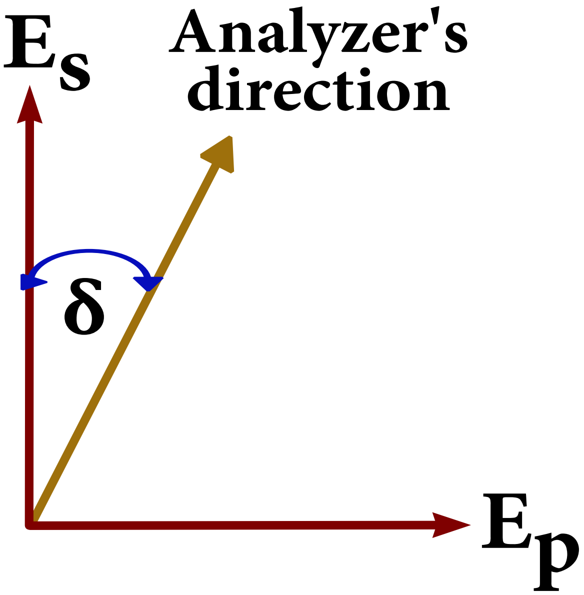

Figure 2.18: The analyzer's actual orientation. The reflected light has two component waves E_p and E_s which are normal to each other.

Now, if I_o is the intensity of the reflected light in absence of the magnetic field, and δ is the angle between the polarization of I_o and the pass plane of the analyzer (see figure 2.18), with ε_k as the ellipticity; then:

$$\begin{aligned} \frac{E_s}{E_p} &= \theta_k + i\varepsilon_k \\ I_o &= E_p^2 \sin^2\delta \approx E_p^2\delta^2 \end{aligned} \tag{2.14}$$

where, E_s and E_p are the components of the electric field *perpendicular* and *parallel* to the plane of incidence. And the intensity at the detector is :

$$\begin{aligned} I &= \left| E_p \sin\delta + E_s \cos\delta \right|^2 \\ &= E_p^2 \left| \sin\delta + \frac{E_s}{E_p}\cos\delta \right|^2 \\ &\approx E_p^2 \left| \delta + \theta_k + i\varepsilon_k \right|^2 \\ &\approx E_p^2 \left(\delta^2 + 2\delta\theta_k\right) \\ &= I_o \left(1 + \frac{2\theta_k}{\delta}\right) \end{aligned} \tag{2.15}$$

Hence,

$$\theta_k = \left(\frac{\delta}{2}\right)\left(\frac{\Delta I}{I_o}\right) \tag{2.16}$$

Since, for a magnetic medium; $\theta_k = \kappa M$, we can readily get:

$$M \propto \theta_k \propto \Delta I (= I - I_o) \tag{2.17}$$

Thus variation of the Kerr rotation angle θ_k $ie, (I - I_o)$ with the varying external magnetic field gives the *Hysteresis* curve, and present the magnetic state of the material.

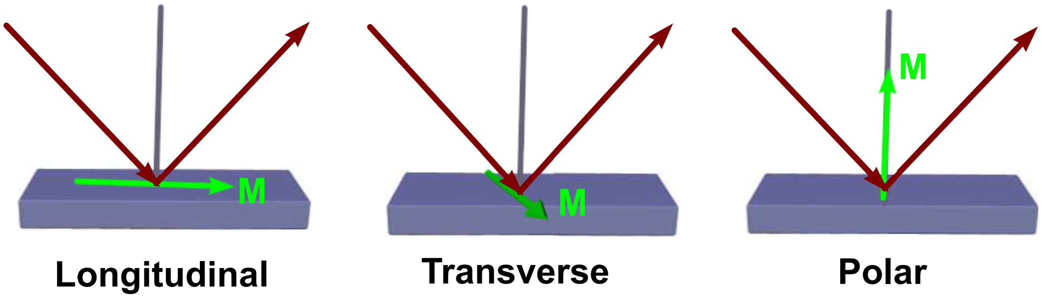

Figure 2.19: The different orientation mode of MOKE set up

In general, the MOKE experiments can be performed in three different geometries (shown in fig. 2.19), they are :

- Polar MOKE : The external magnetic field is applied perpendicular to the surface of the medium and parallel to the plane of incidence.
- Longitudinal MOKE : The external magnetic field is applied parallel to the surface of the medium and parallel to the plane of light incidence.
- Transverse MOKE : The external magnetic field is applied parallel to the surface of the medium and perpendicular to the plane of light incidence.

For this thesis work, the longitudinal mode MOKE facility at IUAC−Indore was utilized. The schematic of the MOKE setup is shown in fig. 2.20. A commercial He-Ne laser ($\lambda =$ 632.8nm), with average power incident of 1mW on the sample surface were used. Two Glan-Taylor prism (with anti -reflector coating) were used as a polarizer and analyzer. An electromagnet with copper windings around a high purity U- shaped TATA-A grade low carbon steel core were used to generate the external magnetic field.

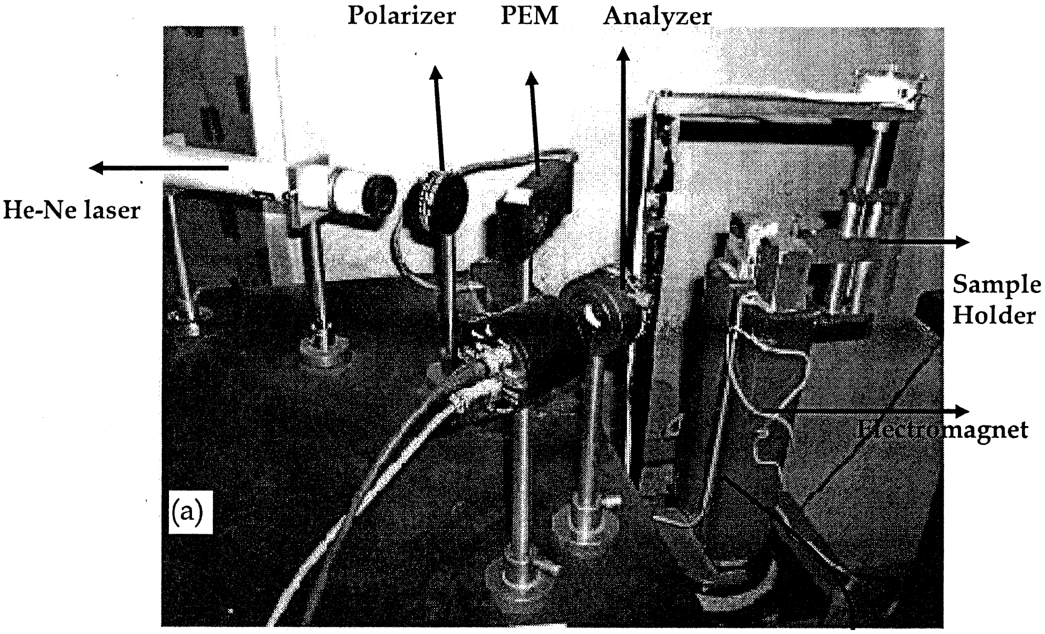

Figure 2.20: The schematic of longitudinal MOKE set up

2.3.7 X-Ray Diffraction (XRD)

X-ray diffraction (XRD) technique is used to analyze the phase identification as well as crystal structure of the materials. X-rays are electromagnetic radiation with photon energies in the range of 100 eV to 100 keV. For diffraction applications, only short wavelength x-rays in the energy range of 1 keV to 120 keV are used. X-rays are ideally suitable for probing the atomic structures of materials because, their wavelengths (0.1 to 2 Å) are comparable to the radii of the atoms and they are sufficiently energetic to penetrate most materials to provide information about the structure of the material. In powder samples, the crystalline domains are randomly oriented in 3-D space. Therefore, when the 2-D diffraction pattern is recorded, concentric rings of scattering peaks corresponding to the various lattice spacings (d) in the crystal are observed. The positions and the intensities of the peaks are used for identifying the underlying structure (or phase) of the material. In case of single crystalline sample, the crystalline domains are oriented, rather in single planes. X-ray diffraction analysis uses the property of crystal lattices to diffract monochromatic X-ray light. This involves the occurrence of interferences of the waves scattered at the successive planes (see fig. 2.21a), which is described by Bragg's equation:

$$n\lambda = 2d\sin\theta(n = 1, 2, 3...) \tag{2.18}$$

where λ is the wavelength, d is the lattice plane separation and θ is half of the diffraction angle.

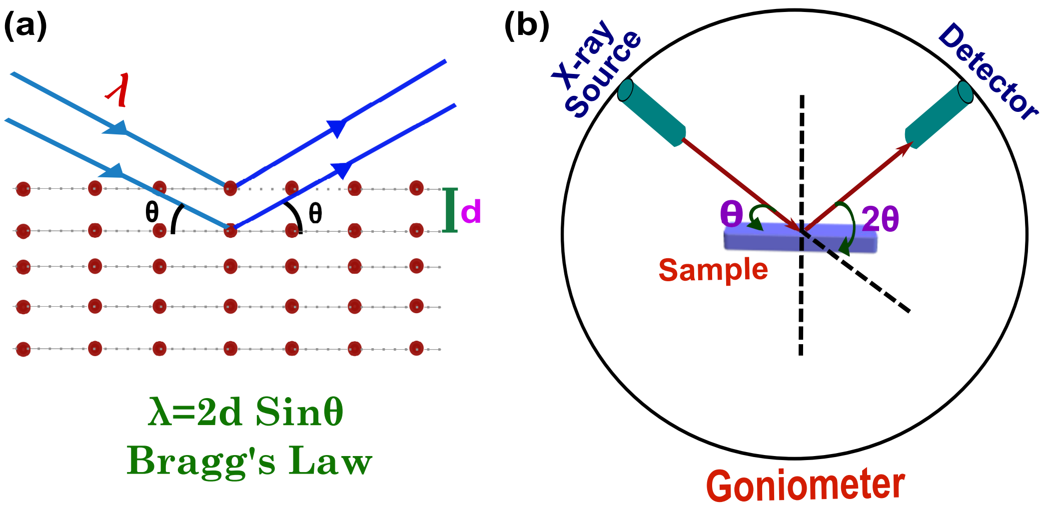

Figure 2.21: The schematic showing (a) the Bragg's diffraction in single crystal and (b) XRD powder diffractometer setup.

The diffractometer consists of a Goniometer, X-ray source, and a detector. CuK_α radiation (1.5415Å) is used as the X-ray source and scintillation counter as the detector. The goniometer consists of a fixed X-ray source, which requires that the detector and the sample tilt simultaneously to render the $\theta - 2\theta$ angular relationship between source and the detector (see fig. 2.21b). The system has a wide-ranging step and continuous scan capability with programmable step rotation.

2.3.8 Photoluminescence (PL) Spectroscopy

Photoluminescence (PL), in general, refers to the emission of light that results from optical excitation. It is a non destructive technique and easy parameter control of temperature and laser excitation makes PL spectroscopy a powerful technique for materials characterization. For PL studies of semiconductors, the general approach is to use a suitable laser that has a photon energy output larger than the energy band gap of the semiconductor. It will create electron-hole pair in the lattice. These electron-hole pairs will recombine, often through radiative transition back to the ground state of the atom. The emitted light is detected as photoluminescence and the spectral dependence of its intensity is analyzed to provide information about the band gap, donor and acceptor levels, defect types, impurities, crystalline quality, and defect densities within the materials system. In the present thesis, Fluromax spectroflurometer setup excited with 320nm wavelength, at room temperature, was used.

2.4 Crystal Structures

2.4.1 Structure of TiO_2

Titanium dioxide (TiO_2) is a highly investigated transition metal oxide. The reason of its superiority lies in the facts that it is a wide bandgap semiconductor and can offer different phases like, bulk [29], nanoparticles [30] and nano- surfaces [31] for various applications. In dye-sensitized solar cells the TiO_2 surfaces play a major role not only through anchoring of the dye molecules, but also due to their photocatalytic properties [32, 33]. This ability is also utilized in applications like wastewater treatment [29] or heterogeneous catalysis [31,35]. Due to their availability, low cost and photochemical stability [36], these materials are preferred over other semiconductor materials. Three primary crystalline structures of TiO_2 are [37–41]: rutile (tetragonal), anatase (tetragonal) and brookite (orthorhombic). Their variations can be understood in terms of (TiO_6^{2-}) octahedral differing by the distortion and connectivity of the octahedral chains [29]. Report on the stability of the different modifications of the TiO_2 crystal structures are discussed in detail by Navrotsky et al. [35], where the following order of stability have been found: **rutile** $>$ **brookite** (+0.7 $kJmol^{-1}$) [42]$>$ **anatase** (+2.6 $kJmol^{-1}$) [43] with an error of $\pm$ 0.4 $k\ J\ mol^{-1}$.

The unit cell structures of TiO_2 are shown in fig. 2.22. The coordinate system for the rutile TiO_2 is also presented in fig. 2.23. The different crystal lattice parameters of TiO_2, and their respective other physical characteristic parameters are shown in Table 2.1.

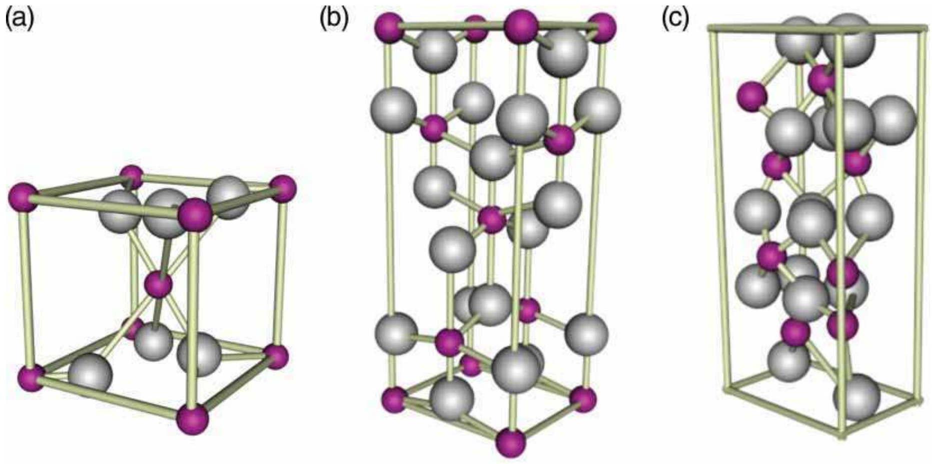

Figure 2.22: Unit cells of TiO_2 crystal structure modifications (a) rutile, (b) anatase and (c) brookite. Grey (big) and red (small) spheres represent the oxygen and titanium atoms, respectively (from ref [48])

.

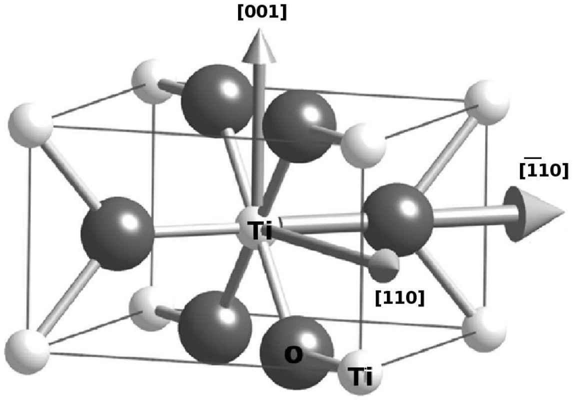

Figure 2.23: Crystal structure of rutile TiO_2 (from ref [28]).

Table 2.1: Lattice parameters of TiO_2 crystal modifications.

	Rutile [44, 45]	Anatase [45–47]	Brookite [45–47]
Z^a	2	4	8
a (Å)	4.587	3.781	9.174
b (Å)	a	a	5.449
c (Å)	2.954	9.515	5.138
Volume^b	31.21	33.98	32.17
Formula Wt.	79.89	79.89	79.89
Crys. System	Tetragonal	Tetragonal	Orthorhombic
Point Group	4/mmm	4/mmm	mmm
Space Group	$P4_2$/mnm	$I4_1$/amd	Pbca
Bandgap (eV)	3.2	3.0	2.96

a, b, c are the lattice parameters of the unit cell

[a] Z is the number of asymmetric units in the unit cell.

[b] Volume is in $Å^3$ per TiO_2 formula unit.

2.4.2 Structure of ZnO

The Zinc Oxide (ZnO), is a wide direct bandgap (3.4 eV) II-VI compound semiconductor. It has a stable hexagonal wurtzite (WZ) structure with lattice spacing a = 3.258 Å and c = 5.22 Å. It can also exist in rocksalt (RS) and zinc blende (ZB) structures, but the WZ symmetry is thermodynamically most stable under the ambient condition. The ZB structures can be stabilized by growing on cubic substrates whereas the RS structures only exist at high pressure. ZnO has applications in transparent electronics, thin film transistors, UV light emitters, piezoelectric devices, chemical sensors and spin electronics. It exhibits catalytic efficiency, strong absorption ability, high isoelectric point, biocompatibility and fast electron transfer for biosensing. The most important parameters of the different ZnO crystal structures are presented in Table 2.2, and the unit cell structures are shown in fig. 2.24.

Table 2.2: Lattice parameters of ZnO crystal modifications

	Wurtzite [49, 50]	Rockslat [49, 50]	Zinc Blende [49, 50]
a (Å)	3.258	4.271	4.62
b (Å)	a	a	a
c (Å)	5.220	a	a
Volume[a]	23.81	19.60	24.551
Crys. System	Hexagonal	Cubic	Cubic
Point Group	6mm	4/m -32/m	$\bar{4}3m$
Space Group	$P6_3mc$	Fm3m	$F\bar{4}3m$
Bandgap (eV)	3.4	4.27	2.7

[a] Volume is in $Å^3$ per ZnO formula unit

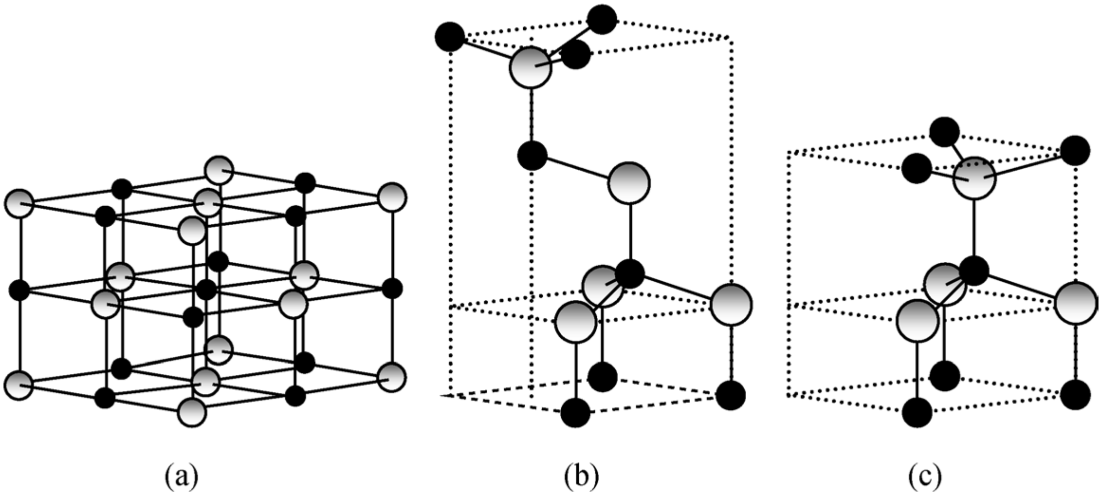

Figure 2.24: Unit cells of ZnO crystal structure modifications: (a) cubic rocksalt (b) cubic zinc blende, and (c) hexagonal wurtzite. Shaded gray and black spheres denote O and Zn atoms, respectively. (from ref [50])

.

2.4.3 Structure of Mercury (Hg)

Mercury is a metal and displays several interesting properties. It is liquid at room temperature and the metal solidifies only below 234K into αHg phase. This is a rhombohedral structure with one atom per unit cell and primitive vectors at an angle of $70^\circ 44.6'$ [51]. Below 79K, mercury usually crystallizes in βHg phase which is a body centered tetragonal phase with a c/a ratio of 0.7071 [52]. Near room temperature, αHg phase can transform to βHg phase under pressure. A third, metastable phase, γHg is rhombohedral with one atom per unit cell with the primitive vectors at an angle of 50° [52]. Exposure to mercury or its compounds can cause toxic effects also known as “mercury poisoning”. Mercury is a heavy metal and all its forms are known to be hazardous. Toxic effects include damage to brain, kidney, and lungs [53]. Toxic nature of mercury also denatures the DNA structure. This poses a serious concern and stresses the need for understanding the interaction properties of mercury with DNA.

2.4.4 Structure of Deoxyribonucleic Acid (DNA)

DNA Subunits : Oligonucleotide

DNA is the acronym of a molecule called Deoxyribonucleic Acid [54], which contains the whole biological instruction inside the cell that make each species very unique. During 1800, the German biochemist Frederich Miescher first observed the DNA. For many years, scientists debated on the issue searching the molecule which carry life’s biological instructions. In the initial time it was thought that the proteins are more likely to carry out this vital function instead of the DNA. It is because of the more complex nature and wider variety of forms of the protein than the DNA available in nature. But gradually as the structure of the DNA molecule was revealed, it became clear that this molecule controls each aspects of the cell, and thus it became of central importance to biology.

After a century from discovering the DNA, the secret of the molecule got revealed by the pioneering discovery of James Watson and Francis Crick in 1953. Watson and Crick suggested the first most successful corrected double-helix model of DNA structure in the journal *Nature* [55]. The model of the double-helix of DNA was constructed based on single X-ray diffraction image taken by Rosalind Franklin and Raymond Gosling in May 1952. Thus the most strange chemical structures of all time that enable it to carry biological information from one generation to the next were discovered.

The fundamental components of DNA are monomeric units called nucleotides [54, 56, 57]. Each nucleotide consists of a sugar, a nucleobase and a phosphate group (see fig. 2.25(a)). The sugar in DNA is the deoxyribose as the hydroxyl group on the $2'$ carbon of the ribose ring is replaced with hydrogen. Figure 2.25(b) shows the chemical structures of the four major nucleobases found in DNA which are derived from the two parent groups purine (5C + 4N group) and pyrimidine (4C + 2N group). The bases **adenine** (A) and **guanine** (G) are from **purine** group, whereas **cytosine** (C) and **thymine** (T) bases are from **pyrimidine**. Each nucleobase is attached to the sugar through β-glycosyl C'-N linkage (which is N1 of pyrimidines and the N9 of purines). The phosphate group is attached to the sugar through an ester bond at the 5/ carbon of the sugar (see fig. 2.25(a)). Thus a nucleotide is formed though phosphate-sugar-base compound.

The as formed nucleotides now if joined together successively forms a single strand of DNA which is called the *oligonucleotide*. The nucleotides in this chain linked covalently to each other through a phosphodiester bond in which the $5'$-phosphate group of one nucleotide is attached to the $3'$ hydroxyl group of the next nucleotide. The direction of this chain is pointed from $5'$ to $3'$ for the sake of description. A four base DNA oligonucleotide with the sequence $5'$-CTAG- $3'$ is shown in fig. 2.26.

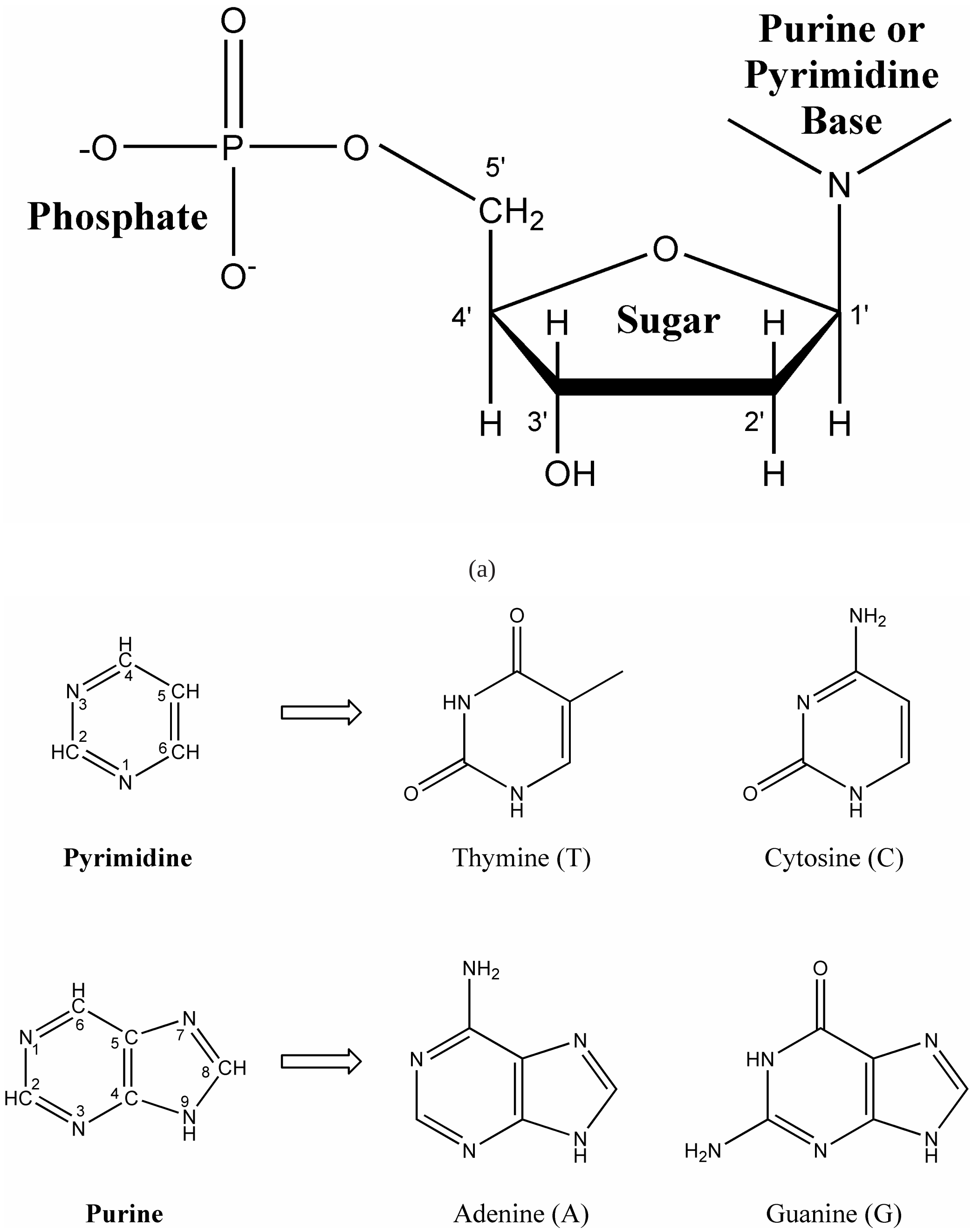

(a)

(b)

Figure 2.25: (a) The chemical structure of a single nucleotide unit (phosphate-sugar-base) is shown. (b) The chemical structure of the Purine and Pyrimidine group bases of the DNA are represented. The pyrimidine structure is a six-carbon, two-nitrogen molecule whereas purine is nine-carbon, four-nitrogen molecule.

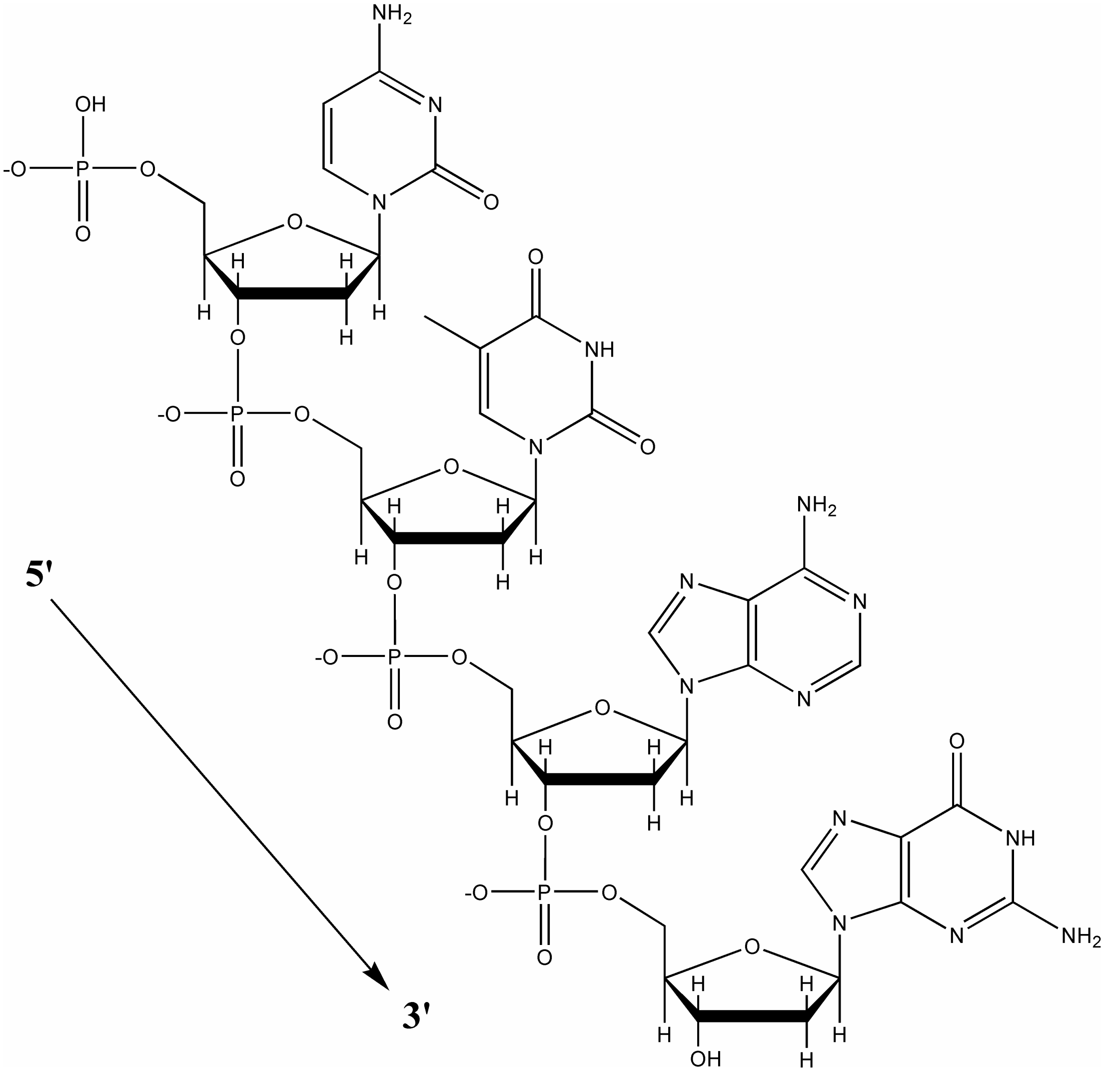

Figure 2.26: Formation of a de-oxy-tetranucleotide (dCTAG) chain. The direction of the chain is represented along 5′ phosphate end to 3′ hydroxyl end.

.

DNA double strand structure: Base pairing

A complete DNA double strand (which is called the DNA double helix) is formed by simply joining together two strings of nucleotides side by side. This conjugation is not random, but rather is very systematic, which follow a specific chemistry. The joining process is referred to as hybridization and is mediated through specific base pairing. The basic rule that governs this hybridization process can be summarized as following:

- The smaller base (pyrimidine)always pairs with a bigger one (purine). The effect of this is to keep the two chains at a fixed distance from each other all the way along.
- adenine (A) always pairs with thymine (T).
- guanine (G) always pairs with cytosine (C).

This specificity of base pairing is due to the fact that, the bonding of these combinations give a stable DNA structure. This has been the most pioneering discovery in 1953 by Watson and Crick, who first proposed this very specific type of pairing of the DNA bases inside the DNA double helix structure, and is popularly named as Watson-Crick (WC) model. This pairing of the nitrogen bases is called complementarity, and is achieved through the formation of intermolecular hydrogen bonds between the two DNA strands. In the DNA helix structure, the two single strand chains run in opposite directions, with the right-hand chain essentially upside-down. The WC base pairing is shown in fig. 2.27.

The hydrogen bonds are formed from noncovalent type of interaction. In order for hydrogen bonding to occur between the bases, a hydrogen bond donor in one base must have a complementary hydrogen bond acceptor in the complementary base. The most common hydrogen bond donors are the primary and secondary amine groups or hydroxyl groups, whereas the most common acceptor groups are the carbonyls and tertiary amines.

Hydrogen bond donors	Hydrogen bond acceptors
Primary amine ($>$N—)	Carbonyl (C=O)
Hydroxyl (—O—H)	Tertiary amine (C≡N)

The base pairings of the DNA structure for the A, T, G, C bases are shown in fig. 2.27(a). The hydrogen bonds are formed through the dipole-dipole interactions appearing due to the result of the attractive force between hydrogen atoms containing a partial positive charge of one base interacting with the electronegative keto oxygens or nitrogens of the complementary base. GC base-pairs have three hydrogen bonds, whereas the A-T has only two base pairs.

Apart from the above WC model of DNA base pairing, one can find several other hydrogen bonding patterns that have been discovered after WC, and which can also make stable structure. But they have very severe limitations as opposed to WC model. As for example, the model proposed by Karst Hoogsteen in 1963 [58], where the adenine and thymine can form hydrogen bonds involving the N7 atom of the purine ring compared to the N1 atom found in the WC base pairing. It has been seen, this Hoogsteen geometry is the most favorable one for only AT base-pairs in solutions, whereas the GC base-pairs are only able to form this geometry in acidic pH where protonation of the C is essential for pairing. Inside the DNA the parallel stacking of the base pairs maximizes the van der Waals interactions between bases. Most duplex DNA structures have the bases separated by 0.34 to 0.37 nm, which is the average sum of van der Waals radii of the base atoms (shown in fig. 2.27(b). The helicity of the DNA is almost 10 base pairs. The radii of the DNA is about 2nm.

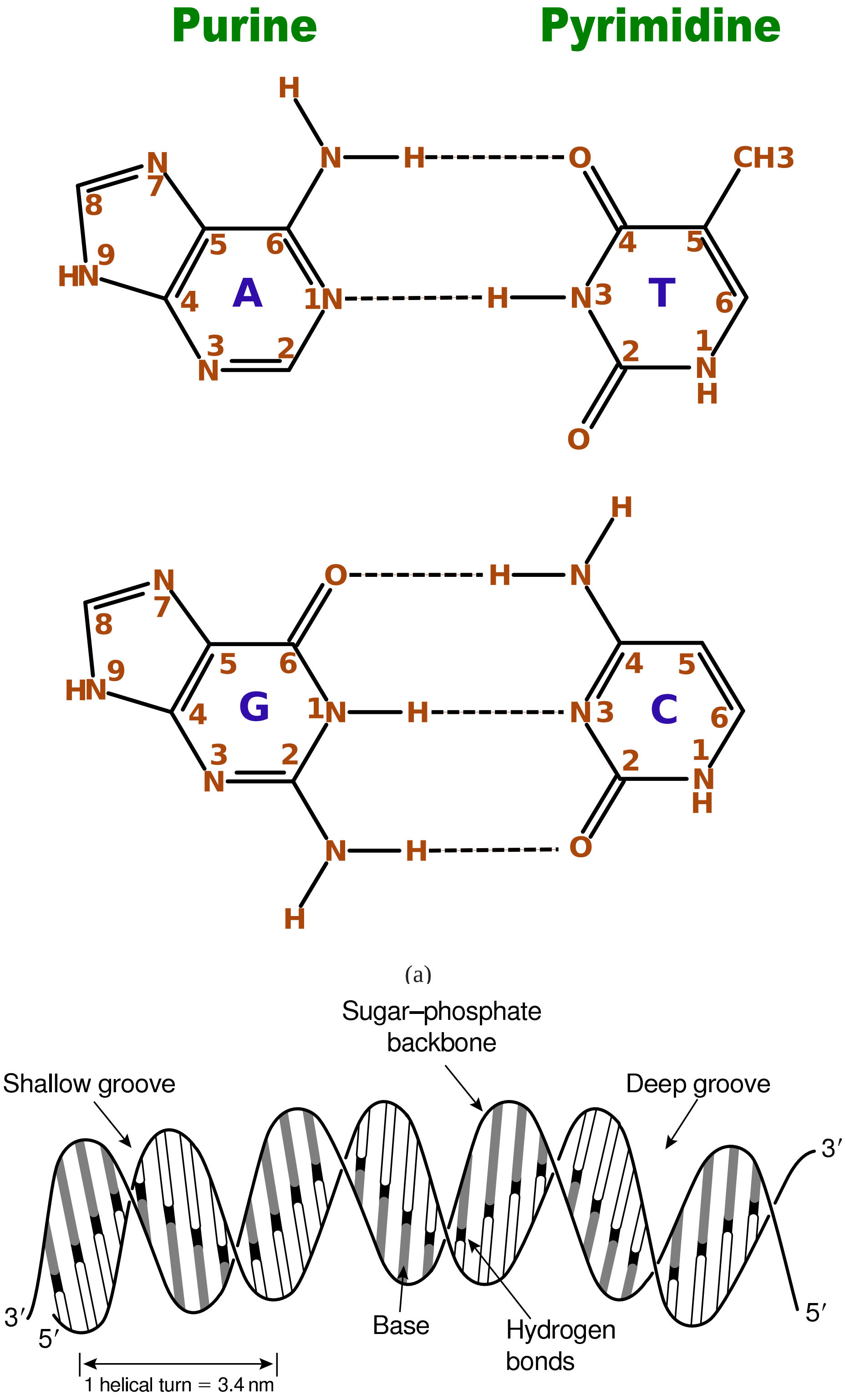

(a)

(b)

Figure 2.27: (a) The WC base pairing of the DNA double strand. **A** complimentarily pairs with **T** and **G** with **C**. (b) The double stranded DNA (helix) structure.

References

[1] Koji Kudo, Yasuaki Nagashima, Munehisa Tamura, Shigeo Tamura, Akinori Ubukata, and Shigehisa Arai, Jpn. J. Appl. Phys. 33 pp. L1382-L1385 (1994).

[2] P. Suominen and F. Wenander, Rev. Sci. Instrum. 79, 02A305 (2008).

[3] Siegbahn, K., and Edvarson, K. I. Al, Nuclear Physics 1 (8): 137-159 (1956).

[4] Siegbahn, K. "Electron Spectroscopy for Atoms, Molecules and Condensed Matter", Nobel Lecture, December 8, 1981

[5] Handbook of X-ray photoelectron spectroscopy, edited by C. D. Wagner, W. M.Rigs, L. E. Davis, J. F. Moulder, and G. E. Muilenberg, Perkin-Elmer, Eden Prairie, MN, 1978.

[6] V. I. Nefedov, X-ray Photoelectron Spectroscopy of Solid Surfaces, (Brill-VSP Pulishers, 1988)

[7] Physics at surfaces edited by Andrew Zangwill, Cambridge University Press, 1988.

[8] “Practical Surface Analysis- Auger and X-ray Photoelectron Spectroscopy”, edited by D. Briggs and M. P. Seah, Wiley Interscience, 1990.

[9] “An introduction to surface analysis by XPS and AES”, edited by John F. Watts, John Wolstenholme, Wiley Interscience, (2003).

[10] T. A. Carlson, Academic Press, (1978).

[11] "Scanning Probe Microscopy and Spectroscopy: Methods and Applications", R. Wiesendanger (Cambridge University Press, 1998); "Scanning Probe Microscopy and Spectroscopy: Theory, Techniques, and Applications", 2nd ed., D. Bonnell, (Ed.), (Wiley-VCH, New York, 2001); "Introduction to Scanning Tunneling Microscopy", C.J. Chen (Oxford University Press, 1993). "Scanning Tunneling Microscopy", Vol. I, II, and III, H.-J. Guentherodt, R. Wiesendanger (Eds.), (Springer, 1993, 1995, 1996).

[12] G. Binning, H. Rohrer, Helv. Phys. Acta 55, 726 (1982)

[13] G. Binning, H. Rohrer, Ch. Gerber, and E. Weibel, Phys. Rev. Lett. 50(2), 120 (1983).

[14] G. Binnig, C. F. Quate and Ch. Gerber, Phys. Rev. Lett. 56, 930 (1986).

[15] J.F. Borrull, A. Duparre, E. Quesnel, Appl. Opt. 40 (13) 2190-2199 (2001) .

[16] J.P. Singh, R. Singh, N.C. Mishra, D. Kanjilal, V. Ganesan, J. Appl. Phys. 90 (12) 5968-5972 (2001) .

[17] Annalisa Calo, Pablo Stoliar, Eva Bystrenova, Francesco Valle, and Fabio Biscarini, J. Phys. Chem. B, 113, 15, (2009).

[18] Beer, Annalen der Physik und Chemie, vol. 86, pp. 78-88 (1852).

[19] Pierre Bouguer, Essai d’Optique, sur la gradation de la lumiere (Paris, France: Claude Jombert) pp. 16-22 (1729).

[20] J. D. J. Ingle and S. R. Crouch, Spectrochemical Analysis, Prentice Hall, New Jersey (1988).

[21] Hoffman, M., Martin, S., Choi, W., and Bahnemann, D., Chemical Review,vol. 95, pp. 69-96 (1995).

[22] N. F. Mott, R. W. Gurney, Electronic Processes in Ionic Crystals, Oxford Univ. Press,London, 1940.

[23] N. D. Mermin andH. Wagner, Phys. rev. Lett. 17, 1133 (1966).

[24] Kerr, John., Philosophical Magazine 3: 321 (1877).

[25] Weinberger, P., Philosophical Magazine Letters 88 (12): 897-907 (2008).

[26] J A C Bland, R Bateson and G Hird, J. Phys.: Condens. Matter 1 4399 (1989).

[27] R. M. A. Azzam and N.M. Bashra, North Holland, Amsterdam (1977).

[28] B. Jiang, J. M. Zuo, N. Jiang, M. O'Keeffec and J. C. H. Spence, Acta Cryst. A59, 341-350 (2003).

[29] Carp O, Huisman C L and Reller A, Prog. Solid State Chem. 32, 33-177 (2004).

[30] Zhou K B and Li Y D, Angew. Chem. Int. Edn 51, 602-13 (2012).

[31] Diebold U, Surf. Sci. Rep. 48 53-229 (2003).

[32] Wang M, Chen P, Humphry-Baker R, Zakeeruddin S M and Gratzel M, Chem. Phys. Chem. 10, 290-9 (2009).

[33] Oregan B and GrÃd'tzel M, Nature 353, 737âĂŞ40(1991).

[34] Comotti M, Li W C, Spliethoff B and Schuth F, J. Am. Chem. Soc. 128, 917-24 (2006).

[35] Navrotsky A, Chem. Phys. Chem. 12, 2207-15 (2011).

[36] J.-C. Sin, S.-M. Lam, and A. Mohamed, Korean J. Chem. Eng. 28, pp. 84-92 (2011).

[37] Y.R. Park, K.J. Kim; Thin Solid Films, 484, pp. 34-38 (2005).

[38] Z. Liu, L. Hong, B. Guo; Journal of Power Sources, 143, pp. 231 (2005).

[39] L.A. Brook, P. Evans, H.A. Foster, M.E. Pemble, A. Steele, D.W. Sheel, H.M. Yates; J. of Photochem. and Photobio A: Chemistry, 187, pp. 53 (2007).

[40] S. Banerjee, J. Gopal, P. Muraleedharan, A.K. Tyagi, B. Raj; Current Science, 90 (10), pp. 1378-1383 (2006). Y.L. Wang, K.Y. Zhang; Surface and Coatings Technology, 140, pp. 155-160 (201).

[41] X. Bokhimi, A. Morales, M. Aguilar, J.A.T. Antonio, F. Pedraza; Int. J. of Hydrogen Energy, 26, pp. 1279 (2001).

[42] S. Chen, A. Navrotsky, Am. Mineral., 95, 112 (2010).

[43] A. A. Levchenko, G. Li, J. Boerio-Goates, B. F. Woodfield, A. Navrotsky, Chem. Mater. 18, 6324 (2006).

[44] Swope R J, Smyth J R and Larson A C, Am. Mineral. 80, 448 (1995).

[45] V. Swamy, J.D. Gale, L.S. Dubrovinsky, Journal of Physics and Chemistry of Solids 62, 887-895 (2001).

[46] Meagher E P and Lager G A, Can. Mineral. 17, 77 (1979).

[47] Horn M, Schwerdtfeger C F and Meagher E P, Z.Kristallogr. 136, 273 (1972).

[48] A. R. Khataee, M. B. Kasiri, and L. Alidokht, Environmental Technology, 32:15, 1669-1684 (2011).

[49] Zinc Oxide: Fundamentals, Materials and Device Technology. Hadis Morkoc and Umit Ozgru, WILEY-VCH Verlag GmbH and Co. KGaA, Weinheim.

[50] U. Ozgur, Ya. I. Alivov, C. Liu, A. Teke, M. A. Reshchikov, S. Dogan, V. Avrutin, S. -J. Cho, and H. Morkoc, Journal of Applied Physics, 98, 041301 (2005).

[51] R. W. G. Wycoff, Crystal Structures Vol. 1, 2nd edition, (John Wiley and Sons, New York), pp. 17-18 (1963).

[52] J. Donohue, The Structures of the Elements, (John Wiley and Sons, New York), pp. 191-199 (1974).

[53] Clarkson, T. W., and Magos, L., Critical Reviews in Toxicology, 36(8) (2006), 609-662; Honda, S., Hylander, L., and Sakamoto, M., Environmental Health and Preventive Medicine, 11(4), 171-176 (2006); Tsubaki, T. and Takahashi, H.: Recent Advances in Minamata Disease Studies. Methylmercury Poisoning in Minamata and Niigata, Japan. Tokyo: Kodanska Ltd., (1986).

[54] Saenger, Wolfram, Principles of Nucleic Acid Structure. New York: Springer-Verlag. ISBN 0-387-90762-9 (1984).

[55] Watson J.D. and Crick F.H.C., Nature 171 (4356): 737-738 (1953).

[56] Alberts, Bruce; Alexander Johnson, Julian Lewis, Martin Raff, Keith Roberts and Peter Walters, Molecular Biology of the Cell; Fourth Edition. New York and London: Garland Science (2002).

[57] Butler, John M., Elsevier. pp. 14-15 (2001).

[58] Hoogsteen K., Acta Crystallographica 16: 907-916 (1963).

Chapter 3

Nano-Pattern formation on $TiO_2(110)$ Surfaces with keV ion Irradiation

3.1 Introduction

Titania (TiO_2) has received enormous attention for photocatalytic and photovoltaic applications [1] due to its excellent properties like chemical stability, high reactivity, biocompatibility, nontoxicity and good oxidative characteristics. However, the photocatalytic efficiency of TiO_2 in visible region is limited due to its large bandgap. Achieving narrower bandgap and high Visible light absorption have, thus, become critical issues for TiO_2 [2–5] and some of the important routes taken for addressing these involve its dye sensitization [2], doping [3–5], synthesis as thin films [1] and nanocrystals [5, 6]. Their performance, however, gets restricted due to several limitations like instability of the organic dye [7], thermal instability of dopants [7], complexity in sol-gel based methods [8] with multitude of experimental parameters [9, 10] and formation of mixed crystalline phases [8, 11, 12]. Although Anatase phase has received more attention due to its better photocatalytical properties, it is a metastable phase and transforms to more stable Rutile phase on high temperature sintering [13] during device fabrication. Since Rutile phase is also potentially cheaper to produce [10], it is of significant importance to investigate and explore routes for enhancing the photocatalytic properties of this phase. Dye -sensitized rutile TiO_2 thin films show that their photovoltaic characteristics, although comparable to anatase phase, suffer from smaller surface area per unit volume [10]. Ion beam sputtering technique can produce self assembled, regular arrays of close- packed nanodots in large scale, in a single technological step [14]. Formation of nanodots on Rutile TiO_2 surface through ion beam sputtering, thus, seems an attractive scheme to enhance visible light absorption. Moreover, sputtering can also create surface- vacancies which hold promise for becoming photoactive sites [6].

In this chapter, the formation of TiO_2 nanodots on rutile TiO_2(110) surface by ion beam sputtering technique is discussed. A narrower bandgap along with a significantly enhanced UV-Vis absorption and a higher PL are observed for the nanodot patterned surfaces. Narrowing of bandgap, supported by UV-Vis as well as PL spectroscopy results, has been achieved in the absence of any doping material [15, 16].

3.2 Experimental

TiO_2 nanodots have been formed on single crystals of Rutile TiO_2(110) (purchased from Commercial Crystal Inc., USA) by sputtering them with 3 keV Ar ions from Electron Cyclotron Resonance (ECR) source. The ion sputtering was performed at an incident angle of 60°, from sample normal, for 500 sec (flux = $3x10^{16}$ ions/ cm^2sec) to obtain a fluence of $1.5x10^{19}$ ions/ cm^2. Atomic Force Microscope (AFM- Nanoscope IIIa), in tapping mode, and Field Emission Scanning Electron Microscope (FESEM) from Hitachi were utilized for morphological investigations. X-Ray Photoelectron Spectroscopy (XPS) studies were performed using a VG instrument with a Mg Kα source. Grazing Incidence X-ray Diffraction (GIXRD) studies, at 3° incidence angle, and XRD studies have been performed by utilizing a Bruker system (Cu-Kα source). The resolution of XRD is 0.01°. Optical absorption (UV-Vis) spectroscopy and Photoluminescence (PL) studies were performed using Perkin Elmer spectrophotometer (Lambda-650) and Fluromax spectroflurometer (excitation wavelength

320nm), respectively.

3.3 Results and Discussions

The ECR sputtering of rutile TiO_2 (110) results in the formation of nanostructures on the surface. The processes leading to the formation of nanostructures via low energy (keV) ion beams are discussed in chapter 1 (section 3). Figure 3.1 shows the SEM images from the pristine (un-sputtered) as well as nanodot patterned TiO_2 single crystal surfaces after ECR sputtering. The image (fig. 3.1b) displays a large array of nanodots on a $10 \times 10\ \mu m^2$ surface after sputtering. The nanocrystals are uniform in shape and are about $\sim$ 45-60nm in diameter, with the average size of 50nm as shown in fig. 3.1(c).

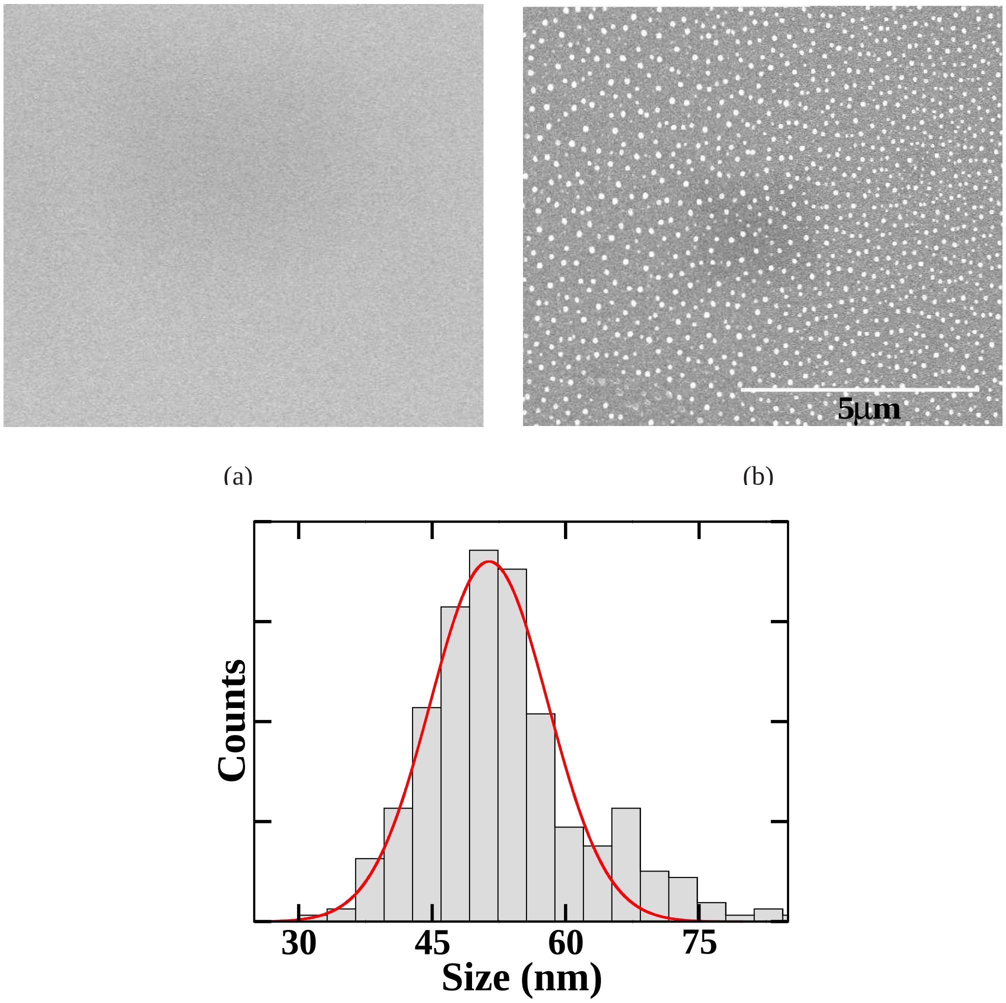

(a) (b)

(c)

Figure 3.1: The SEM images of 10×10 μm^2 TiO_2(110) (a) Pristine and (b) ECR sputtered surfaces. (c) The size distribution of the nanostructures with a mean nano-dot size ∼ 50nm is presented.

Figure 3.2 represents the AFM topographic images from the pristine (fig. 3.2a) as well as ECR sputtered TiO_2 surfaces (fig. 3.2b). The nanodots after sputtering, as shown by AFM in fig. 3.2(c), have columnar shapes and conical caps on top.

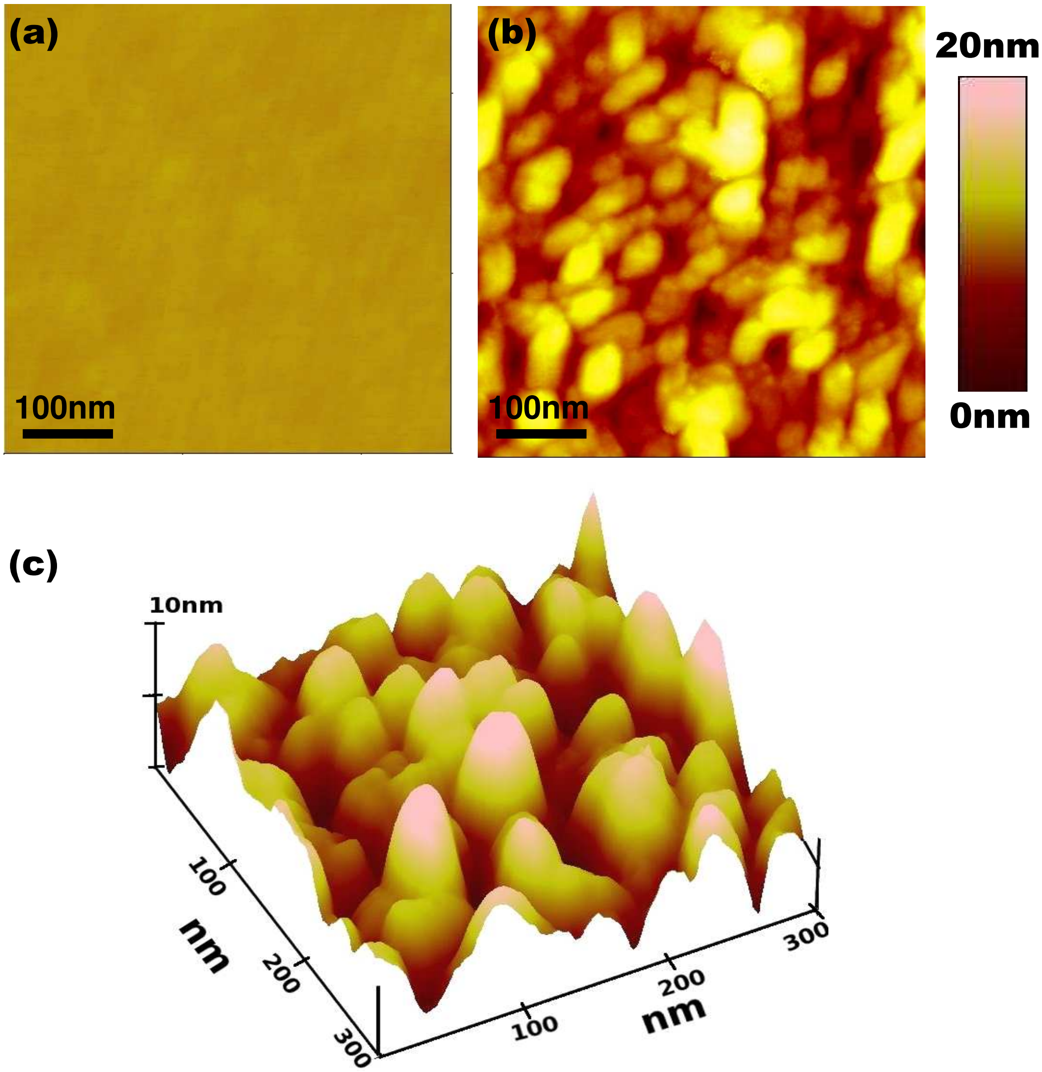

Figure 3.2: 500nm×500nm AFM images from TiO_2(110) surfaces for (a) pristine and (b) after ECR sputtering [height scale is shown]. (c) shows the 3D topographic image of the nanostructures after ECR sputtering on TiO_2(110) surface.

The XRD spectra from the pristine and the sputtered surfaces are shown in fig. 3.3. The XRD spectrum from nanodot patterned surface (Fig 3.3b) displays two extra, (200) and (310), rutile phases in addition to (110) and (220) phases [17] observed in pristine (unsputtered) rutile TiO_2(110) sample (Fig 3.3a). These new features are primarily from the caps of nanodots (see also Fig. 3.2c). Side walls of the nanodots, however, are mainly composed of (301) and (112) rutile planes as displayed by the GIXRD results in fig. 3.3c.

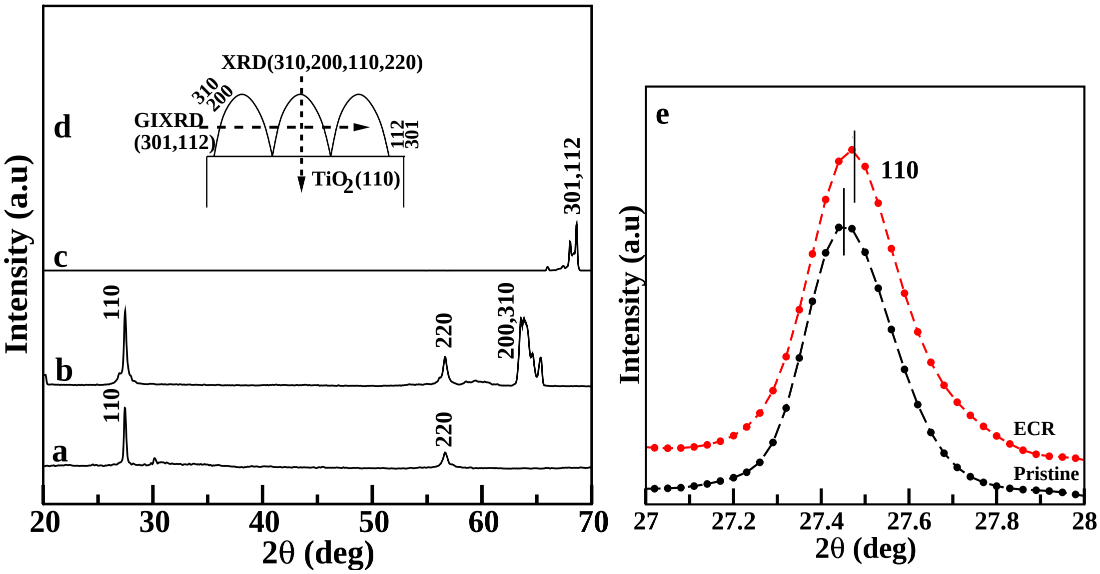

Figure 3.3: XRD from (a) pristine and (b) nanodot-patterned $TiO_2(110)$ surface. (c) GIXRD from nanodot-patterned surface and (d) is the model of nanodot-patterned surface with various planes that are observed in XRD and GIXRD plot. The shift in the (110) XRD peak after sputtering is represented in (e).

The sizes of the dots have been estimated, by applying the Scherrer formula to the strong (110) peak, and are found to be about 50 nm, similar to the SEM and AFM results from fig. 3.1. Figure 3.3e indicates a shift in (110) peak towards higher diffraction angles ($2\theta = 27.47^\circ$) for nanopatterned surface, compared to the virgin sample ($2\theta = 27.43^\circ$). This results a nearly 0.14% decreased inter-planar separation for sputtered TiO_2 compared to pristine sample. The creation of oxygen vacancy with the presence of Ti^{3+}, after sputtering, can cause the modification in the lattice spacings. The reduction in the interlayer spacing, however, will generate some residual stress (σ) which can be estimated by [18]:

$$\sigma = -\frac{E}{\nu}\left(\frac{d_s - d_0}{d_0}\right) \tag{3.1}$$

Here E, ν, d_s, and d_0 are the Young modulus (Pa), Poisson's ratio, d-spacing of the sputtered and pristine TiO_2, respectively. The values for E and ν are respectively 230 GPa and 0.27 for (110) plane in rutile TiO_2 [18]. With d_0 and d_s being 3.2484 and 3.2470 Å, respectively, the residual stress created, post sputtering, through the reduction in interlayer spacing is nearly 1.2 GPa and is of compressive nature.

Figure 3.4 represent the XPS spectra of the pristine and sputtered TiO_2 surfaces. XPS spectrum from pristine sample (fig. 3.4a) displays Ti(2p) features, $2p_{3/2}$ and $2p_{1/2}$, corresponding to Ti^{4+} coordination sites on rutile surface [4, 6]. Each of these features has also associated with it a lower BE component, F1 or F2, due to the Ti^{3+} coordinated (or Oxygen vacancy) sites on the surface [19]. The intensity of these components (F1, F2) though very weak for pristine surface, increases substantially for the nanodot patterned surface indicating a significant enhancement of Ti^{3+} coordinated sites on the surface after ion sputtering (see fig. 3.4b).

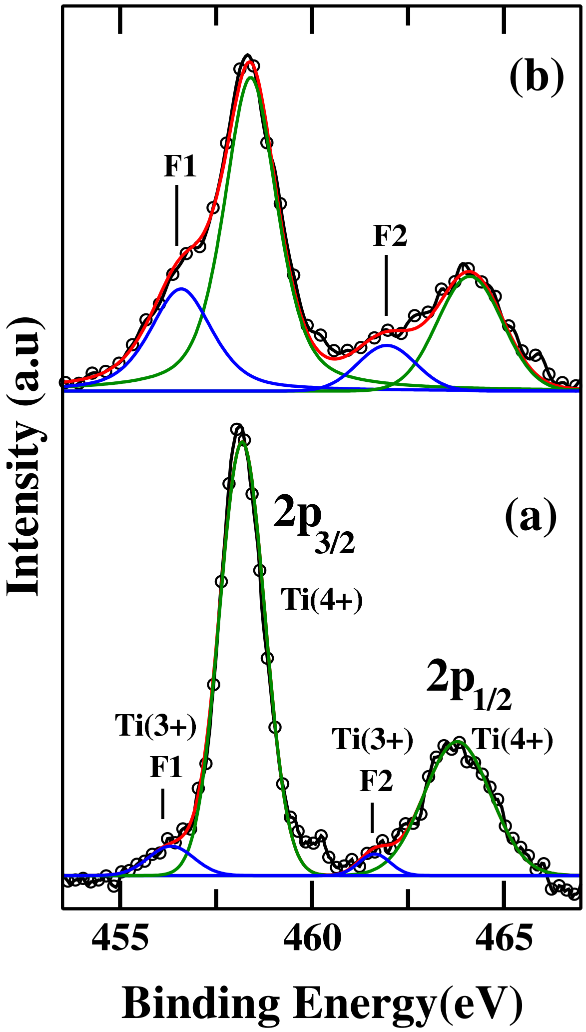

Figure 3.4: XPS spectra from Ti(2p) region for (a) pristine and (b) nanodot patterned surface.

Preferential sputtering of TiO_2 surface during ion beam sputtering creates Oxygen vacancy, with the two associated electrons getting transferred to the empty 3d orbitals of the neighboring Ti atom forming two Ti^{3+} sites. Ti-rich zones, thus formed, can promote nucleation of self assembled nanodots. Formation of nanodot- patterned surfaces by preferential ion sputtering [20] has been earlier shown for InP [14, 21, 22]. However, this is the first study where nanodots have been fabricated on an oxide surface like TiO_2 by ion beam sputtering technique.

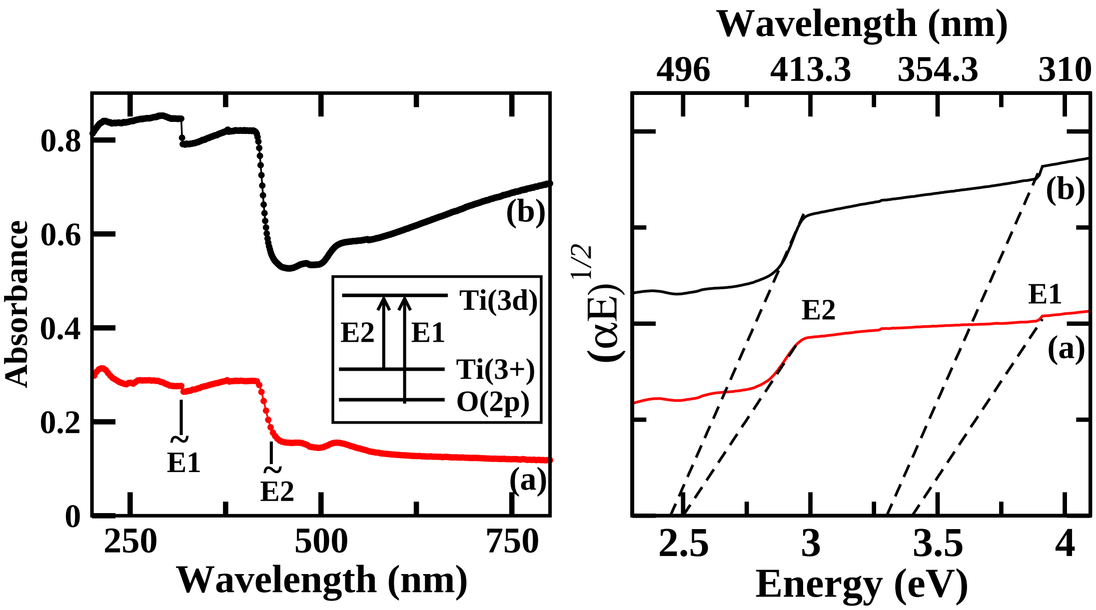

Figure 3.5: UV-Vis absorption spectra (left) and Tauc plots (right) are shown for (a) pristine and (b) nanodot patterned surface. α is the absorption coefficient and *E* the photon energy.

The UV-Vis absorption spectrum from pristine TiO_2, in fig. 3.5a (left) shows two absorption band edges, $\tilde{E}1$ and $\tilde{E}2$, with the former being related to the direct bandgap transition E1 [4], from O(2p) derived valence band to Ti(3d) derived conduction band (see inset), and the later to transition E2 due to a few Ti^{3+} sites present on the pristine surface (as F1, F2 in fig. 3.4a). Surprisingly, in the UV-Vis absorption spectrum from the nanodot patterned surface (fig. 3.5b (left)), in addition to some shifts in band edges which will be discussed later, we also observe a significant enhancement in the absorption of UV-Vis wavelengths compared to pristine sample. This enhancement, nearly 3 times in (280-400 nm) UV regime and almost 5-6 times for visible (450-800 nm) regime, is substantially higher than the absorption observed for N doped TiO_2 nanotubes [23]. The strong absorption, seen in the present study, is primarily due to the formation of nanodots with large surface area. Moreover, the results strongly suggest that the crystalline nanodots, with their exposed (112), (301),(310) and (200) planes (fig. 3.3), act as active sites and effective absorbers of UV-Vis, especially visible, radiation.

During a photocatalytic reaction, the oxygen vacancies also play an active role by becoming potential centers for the capture of photo-induced electrons which effectively inhibit the recombination of photoinduced charge carriers. Furthermore on nanodots, the mean free path of electrons is substantially reduced as they can be very effectively captured by any Oxygen vacancy decreasing their probability of recombination and promoting light absorbance. Thus, in addition to the formation of nanocrystalline dots, creation of excess Ti^{3+} centers on the surface (F1, F2 in fig. 3.4b), during ion sputtering, promote the strong UV-Vis light absorption seen here.

Tauc plots [24], generated using absorbance data (of fig. 3.5(left)) display bandgap energies, E1 and E2, for pristine sample in fig. 3.5a (right) at 3.41 and 2.51 eV, respectively. The bulk band gap seen here, 3.41 eV, is slightly higher than rutile bandgap [4]. However, the energy separation of 1.1 eV between E1 and E2, found here, is in good agreement with UPS studies [4]. The bandgaps, E1 and E2, for the nanodot patterned surface (fig. 3.5b(right)), at 3.29 and 2.44 eV, respectively, are surprisingly $\sim$ 0.1 eV smaller in comparison to pristine sample. This bandgap narrowing is more significant than the (0.07 eV) narrowing seen for N doped TiO_2 nanotubes [23] as in present study reduction in bandgap has been achieved in the absence of any dopant material. This can be explained by the creation of Ti interstitials during preferential sputtering. Results using First Principles and Partial Density Of State (PDOS) calculations show that Ti-rich surfaces promote the creation of Ti interstitials, having localized energy level nearly 0.2 eV below the conduction band minimum (CBM) of TiO_2 [25]. The narrowing of the bandgap by about $\sim$0.1 eV, as seen in the present study, is thus strongly related to excess Ti interstitials that are created during sputtering.

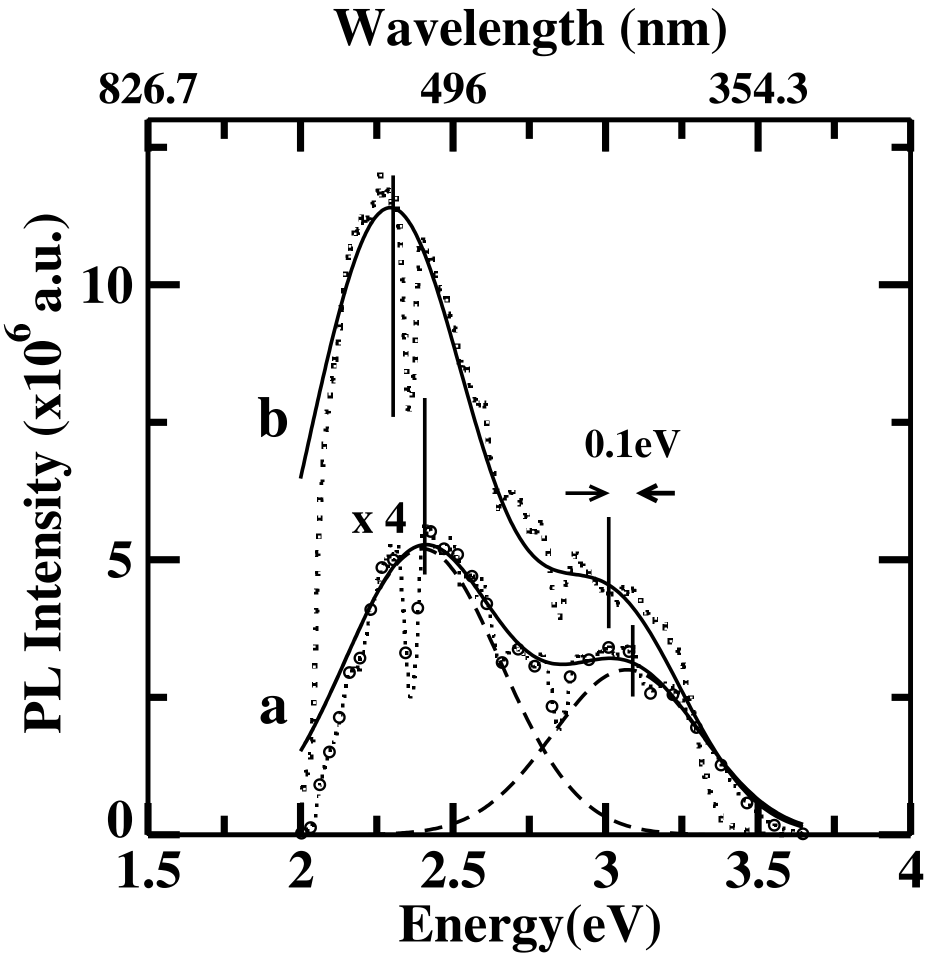

Figure 3.6: Room temperature PL for (a) pristine and (b) nanodot patterned surface (shifts in peak positions are also marked).

The PL spectrum for pristine sample, in fig. 3.6a, displays two components at 3.1 and 2.4 eV due to the direct and Ti^{3+} related transitions, respectively. For the nanodot patterned surface, both these features display a red-shift of $\sim$ 0.1 eV, (see fig. 3.6b) compared to the pristine. This supports the UV-Vis absorption results (seen in fig. 3.5) which also indicate the formation of a narrower bandgap after ion sputtering. Additionally, a significant ($\sim$5 times) increase in the PL intensity for the nanodot patterned surface is also observed.

3.4 Summary and Conclusion

In this chapter, Ar ion sputtering technique has been utilized to fabricate crystalline TiO_2 nanodots on rutile TiO_2(110) surfaces. The results show that the surface becomes Ti rich after sputtering. A reduction in the inter-planar separation after sputtering, indicates presence of a compressive stress in the lattice along [110] direction. The nanodot patterned surfaces display a remarkably enhanced UV-Vis absorption, higher PL as well as a distinct reduction in bandgap. These results, obtained in absence of any dopant material, will have potential for photocatalytic applications.

References

[1] A. Fujishima, T.N. Rao, and D.A. Tryk, J. Photochem. Photobiol. C, 1, 1 (2000).

[2] M. Kocher,T.K. Daubler, E. Harth, U. Scherf, A. Gugel, and D. Neher, Appl. Phys. Lett. 72, 650 (1998).

[3] T. Morikawa, R. Asahi, T. Ohwaki, K. Aoki, and Y. Taga, Jpn. J. Appl. Phys., 40, L561 (2001), J. Y. Lee, J. Park, and J. H. Cho, Appl. Phys. Lett., 87, 011904 (2005).

[4] A.K. Rumaiz, J.C. Woicik, E. Cockayne, H.Y. Lin, G. H. Jaffari, and S.I. Shah, Appl. Phys. Lett., 95, 262111 (2009).

[5] J. Wang, D. N. Tafen,J. P. Lewis, Z. Hong, A. Manivannan, M. Zhi, M. Li, and N. Wu, J. Am. Chem. Soc., 131, 12290 (2009).

[6] P.M. Kumar, S. Badrinarayanan, and M. Sastry, Thin. Sol. Films, 358, 122 (2000).

[7] W. Choi, A. Termin, and M.R. Hoffmann, J. Phys. Chem., 98, 13669 (1994).

[8] F. Dong, W. Zhao, and Z. Wu, Nanotechnology, 19, 365607 (2008).

[9] J. Gautierrez, A. Tercjak, and I. Mondragon, J. Am. Chem. Soc. 132, 873 (2010).

[10] N.G. Park, J. van de Lagemaat, A.J. Frank, J. Phys. Chem. B, 104,8989 (2000).

[11] A.K. Sharma, R.K. Thareja, U. Willer, and W. Schade, Appl. Surf. Sci. 206, 137 (2003).

[12] C. Wang, Z-X Deng, G. Zhang, S. Fan, and Y. Li, Powder Technol. 125, 39 (2002).

[13] W.F. Zhang, M.S. Zhang, and Z. Yin, Phys. Stat. Sol.(a), 179, 319 (2000).

[14] F. Frost, A. Schindler, and F. Bigl, Phys. Rev. Lett., 85, 4116 (2000).

[15] Subrata Majumder, D. Paramanik, V. Solanki, B.P. Bag, and Shikha Varma, App. Phys. Lett., 98, 053105 (2011).

[16] Subrata Majumder, D Paramanik, V Solanki, I Mishra, D.K. Avasthi, D Kanjilal, and Shikha Varma, Appl.Surf.Sci., 258, 4122 (2012).

[17] Y. Masuda and K. Kato, Jour. Ceramic Soc. Jap., 117, 373 (2009).

[18] R.S. Rawat, V. Aggarwal, M. Hassan, P. Lee, S.V. Springham, T.L. Tan, S. Lee, Appl. Surf. Sci. 255, 2932 (2008).

[19] V.E.Henrich, G. Dresselhaus, and H.J. Zeiger, Phys. Rev. Lett., 36, 1335 (1976).

[20] M. Nozu, M. Tanemura, and F. Okuyama, Surf. Sci. Lett., 304, L468 (1994).

[21] D. Paramanik, S. R. Sahoo, Subrata Majumder and Shikha Varma, Vacuum, 84, 602 (2010).

[22] D. Paramanik, S.N. Sahu, and Shikha Varma, Jour. Phys. D: Appl. Phys., 41, 125308 (2008).

[23] Y. Chen, S. Zhang, Y. Yu, H. Wu, S. Wang, B. Zhu, W. Huang, and S. Wu, J. Dispersion Sci. Technol., 29, 2, 245 (2008).

[24] H. W. Eng, P. W. Barnes, B. M. Auer, and P. M. Woodward, J. Solid State Chem., 175, 94-109 (2003).

[25] E. Cho, S. Han, H. S. Ahn, K. R. Lee, S. K. Kim, and C. S. Hwang, Phys. Rev. B, 73, 193202 (2006).

Chapter 4

Interaction of DNA with Nano-Patterned TiO_2(110) Surfaces

4.1 Introduction

In chapter 3, we discussed the creation of nanostructures on rutile TiO_2 surfaces through ion irradiation with low energy Ar ions. During the fabrication of these nanostructures, preferential sputtering of oxygen occurs which results in the creation of oxygen vacancies on the surface. In the process, surface also becomes Ti rich. This formation of nanodots as well as the creation of oxygen vacancies and development of Ti rich zones on TiO_2 surface after irradiation, become responsible, as discussed in the earlier chapter, for the observation of enhanced UV-Vis absorbance, increased PL and a slightly reduced bandgap. These properties display potential for photocatalytic applications. In the present chapter, we discuss the interactions and adsorption properties of DNA on these ion beam modified nanopatterned TiO_2 surfaces.

For DNA based biomolecular surfaces, considerable difference exists in the adsorption of the nucleobases and their derivatives on material surfaces, since adsorption properties crucially depend on the molecular architecture of the adsorbing species. Surface adsorption for even relatively simple species such as oxyanions or metal cations [1, 2], or amino acids

[3] can exhibit complex behavior. Being relatively more complex species, the nucleic acid components, which have complex geometries and multiple functional groups, should have considerably more complicated adsorption properties. Many organic compounds adsorb rapidly on the material surfaces in aqueous solution. The extent of adsorption is dependent on variables like material type, surface roughness, and the type of organic molecule getting adsorbed [4]. The basic adsorption is likely to be mediated at the molecular level by a combination of specific molecule- surface interactions. The interactions of nucleic acids and their components with material surfaces are especially interesting and of fundamental importance.

Recent research has focused on the development of nanostructured materials for the use in biomedical devices, including medical prostheses, implantable biosensors, and drug delivery devices [5]. Due to the small size and high surface area, nanomaterials can have unpredictable adsorption properties [6]. They may lead to excellent adsorption with increased biocompatibility or can cause damage to biomolecules. Thus, it has been of great concern to understand the influence of the nanostructured surfaces on the DNA morphology and its functionality.

Titanium dioxide (TiO_2) is considered to be an excellent and promising material for biomedical implants [7,8] due its nontoxic nature, corrosion resistance properties and compatibility with many biomolecules. Interaction of TiO_2, for example, with phosphate solutions [9] influences the bioactivity of the oxide surface remarkably, through the formation of the biocompatible hydroxyapatite [10, 11], after phosphate ions get incorporated in the oxide layer on titanium. The focus of research, presently, is not only on the bio-effect and interaction of TiO_2 with biomolecules, like DNA, but also on the modification of these interactions. Parameter like nature of the material, its surface, presence of nanostructures, their sizes etc. are essential components necessary for defining and estimating these interactions.

This chapter presents the studies of adsorption and interaction of plasmid DNA with the patterned TiO_2 surfaces. The TiO_2 surfaces have been patterned with the nanostructures, as discussed in chapter 1 and 3, by utilizing low energy Ar ions. The nanodot patterns are induced by sputtering and are generated through self assembly. These patterns get fabricated due to the competition between the roughening mechanisms, produced by curvature dependent radiation sputtering, and various smoothening phenomenon [12, 13]. In order to understand the influence of the nanopatterned surface on the DNA morphology, and its functionality, it is essential to understand the morphological parameters of DNA. Obtaining these parameters is especially important in the systems where DNA displays high packing or entangled networks like on a 2D cell surface where several complex geometries for DNA are observed [14, 15]. In this chapter, the interaction of nanopatterned TiO_2 surfaces with DNA have been investigated by estimating the parameters like *Persistence length* of DNA (P) and its *Correlation length* (ξ). The rigidity or the stiffness of any polymer, like DNA, is defined by P and an increase in this length suggests an enhancement of interactions. An increase in ξ, or the intermolecular separations, of DNA also indicates the promotion of interactions through an increased wetting at the surface.

The *persistence length* of DNA is an important morphological parameter and its definition depends on the chosen model [16]. The *Worm Like Chain* model, proposed by Kratky-Porod [17], has often been employed to describe the average conformation of long, intrinsically straight polymer molecules, including DNA [18]. In this model, DNA is considered to be an intrinsically straight polymer chain which is partly relaxed by the effect of a thermal bath [19] and the persistence length of DNA is the orientational correlation length along the length of the chain. This Persistence length, as shown by Landau and Lifshitz [20], can be expressed as $P = YI/\kappa_B T$ and it depends on Young's modulus (Y), inertial moment (I) of the chain, and the absolute temperature of the medium (T) with κ_B being the Boltzman constant. Another widely used, *Freely Jointed Chain Model* [21], considers the polymer as a chain of uncorrelated independent segments of length $2P$ (Kuhn segments). Independent of any model, P is the direct measure of the polymer's intrinsic physical property, its stiffness. The larger the value of P, the higher will be the stiffness or rigidity of the polymer [22, 23]. Evaluation of P can, thus, be used to assess the interaction of DNA with other molecules and surfaces.

Experimentally, the morphological parameters, P and ξ, of DNA polymer can be estimated by vectorization and analysis of individual DNA molecule imaged by AFM, and then averaged over the full statistical set of discrete images. This process, however, has several limitations like choice of statistical model and dimensionality [23]. Thus, while it is very important to focus on each single DNA molecule with very high pixel of information, it is a tedious process especially if the surface is covered with a very large number of DNA molecules. Recently, studies by Calò et. al. [23] have shown that Power Spectral Density (PSD) [24] analysis, of AFM images, is a powerful technique to obtain the morphological parameters of DNA. Containing full information on the contribution of each spatial frequency to the topography, PSD can provide spatial distribution of the DNA molecules, over the surface, across a multiple length scales [25]. Owing to the isotropic nature of the surfaces adsorbed with DNA molecules, one-dimensional PSD data is obtained by Fourier transforming the AFM image line by line along the fast scan direction and averaging. The range of frequencies, ν, investigated by this method fall between $1/L$ (L being the image size)and the Nyquist frequency $N/2L$ (N being the number of pixels of the image).

4.2 Experimental

Single crystals of Rutile TiO_2(110) were sputtered in UHV (see section 2.2.2 for details), with 3 keV Ar^+ ions, at 15° incident angle. The flux of Ar ions was 1×10^{13} ions/cm^2·sec. The TiO_2 samples were irradiated for two different durations, 10min and 30 min, giving the respective fluences of 6×10^{15} and 1.8×10^{16} ions/cm^2. These ion beam modified surfaces were interacted with the plasmid DNA (pBR 322) that was isolated from DH5α bacterial cell. The plasmid DNA is circular in shape and consists of about 4361 base pairs. The surface morphology, both prior to and after interaction with DNA molecules (concentration of $1ng/nl$), has been investigated by AFM. Similar investigations on the ion beam modified surfaces have also been carried out. The AFMs (Nanoscope IIIa and V) were operated in the tapping mode under ambient conditions. X-Ray Photoelectron Spectroscopy (XPS) measurements were performed on a VG instrument with a Mg Kα source in UHV.

4.3 Results and Discussion

Figure 4.1 shows the AFM images of the morphological evolution of the TiO_2 surfaces, both prior to and after ion irradiation. The figure also displays the modification in morphology of surfaces after their interaction with DNA. The left panel (of fig 4.1), shows the AFM images for virgin TiO_2 as well as for sputtered surfaces. Although the virgin sample displays a smooth surface, after sputtering with a fluence of 6×10^{15} ions/cm^2 an increase in roughness is observed. The sputtered surface also exhibits the formation of some nanostructures but these, however, are not prominent at this stage and appear as small patches. After irradiating with higher fluence, 1.8×10^{16} ions/cm^2, the surface shows the presence of well defined nanostructures. These nanostructures are about 30 nm in size and, as discussed earlier, are self assembled. The rms surface roughness for the surfaces irradiated with the fluences of 6×10^{15} and 1.8×10^{16} ions/cm^2 are found to be 0.127 nm and 2.153 nm, respectively. Right panel in fig. 4.1 displays the AFM images of the surfaces after their interaction with DNA.

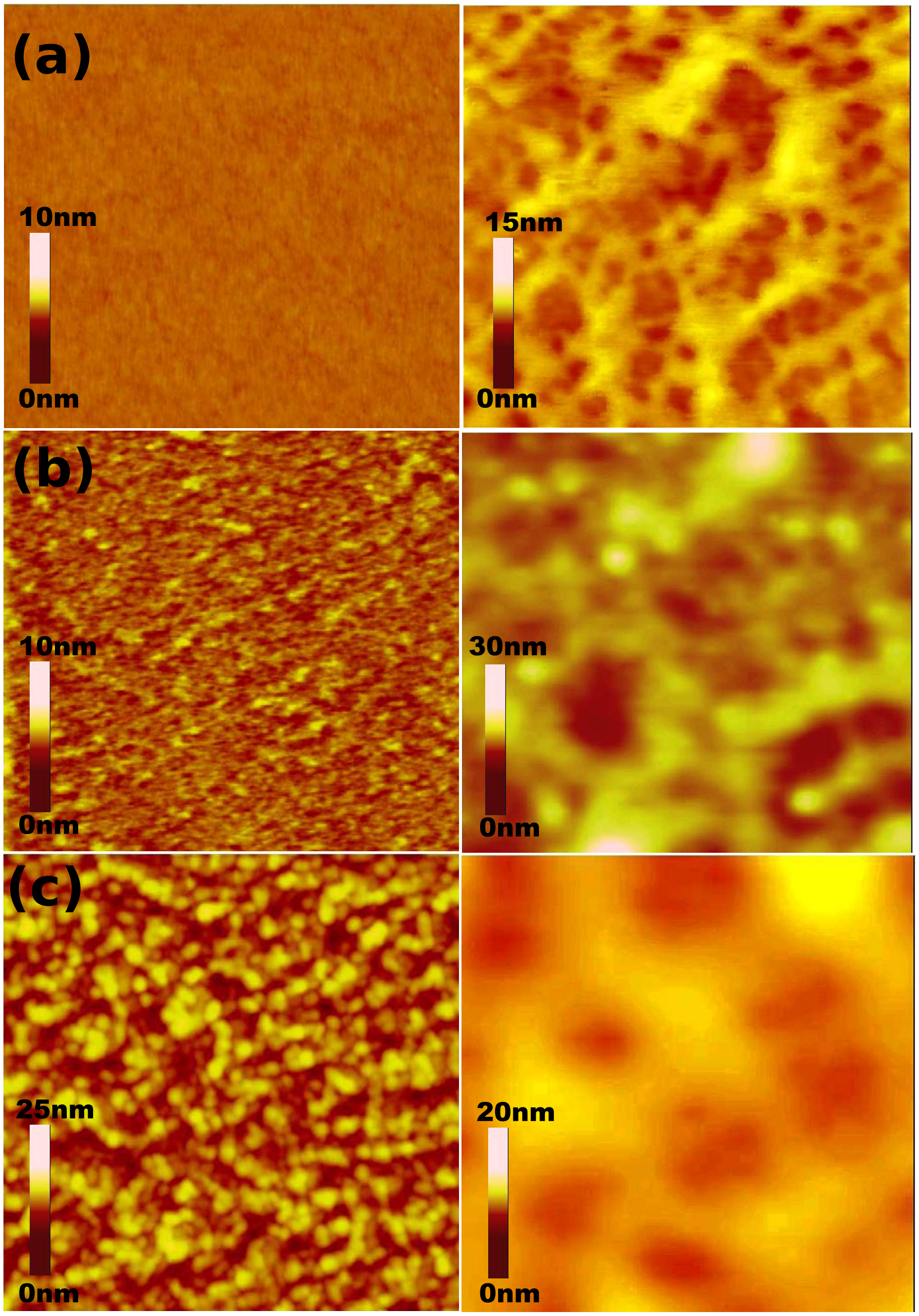

Figure 4.1: 1×1 μm^2 AFM images from un-reacted surfaces are shown in the left panel for (a) virgin TiO_2 and surfaces irradiated with fluences of (b) 6×10^{15} ions/cm^2, and (c) 1.8×10^{16} ions/cm^2. Right panel shows the AFM images of the corresponding surfaces after they are interacted with DNA.

The size (diameter) distributions of the plasmid DNA on the virgin as well as the sputtered surfaces are shown in fig.4.2. The average diameter of the DNA on the virgin surface is about 60 nm which increases to $\sim$ 220 nm and 350 nm on the surfaces irradiated with the fluences of 6×10^{15} and 1.8×10^{16} ions/cm^2, respectively. Figure 4.2 clearly demonstrates an increase in DNA- diameter on the sputtered surfaces compared to the virgin TiO_2 surface. Moreover the surface, sputtered with higher ion fluence, consists of DNA with larger average diameter. These results indicate the crucial effect of surface morphology on the DNA comformations. Also, the enhancement in DNA-diameter, after sputtering, suggests a decrease in contact angle between DNA and the surface. The surfaces, thus, become more hydrophilic, and so more biocompatible, as the irradiation fluence is increased. Better biocompatible and hydrophilic nature, which increases with ion fluence, is related to the higher rms roughness and the formation of nanostructures on the ion irradiated surfaces.

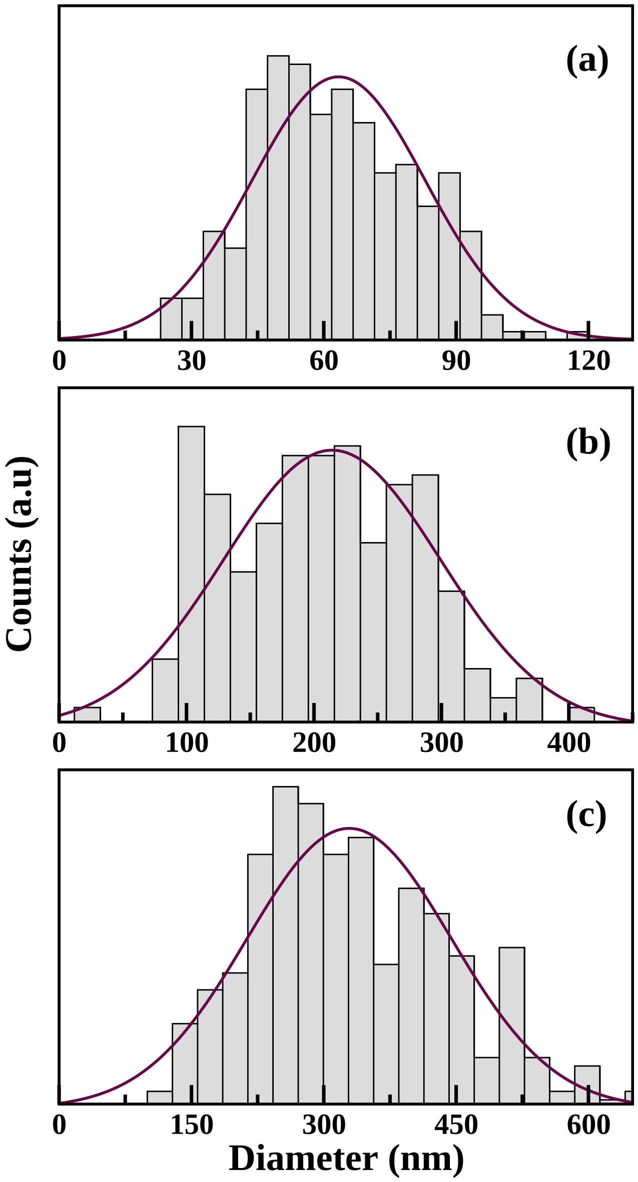

Figure 4.2: Size (diameter) distribution of plasmid DNA after it is interacted with (a) Virgin TiO_2 and surfaces irradiated with fluences of (b) 6×10^{15} ions/cm^2, and (c) 1.8×10^{16} ions/cm^2.

The AFM images similar to those shown in fig.4.1 were utilized to obtain the PSD plots for the virgin surface as well as from the ion sputtered surfaces after their interaction with DNA. Figure 4.3 displays these PSD plots in log-log representation as a function of spatial wave vector (κ) with $\kappa = 2\pi\nu$. The PSDs display a low frequency plateau which is related to the white spectrum. This flat region is followed by freqency -decaying region, that can be approximated by two power law decays, each spanning about 1 order of magnitude of κ, the spatial frequencies. The spatial correlations, or multiaffine behavior, in any system lead to power law decaying regions. The specific frequencies where the different regions intersect correspond to the inverse of correlation lengths. The larger correlation length, related to the smaller frequency, corresponds to the intermolecular separations (ξ) whereas the smaller correlation length is associated with the Persistence length (P) of the DNA.

The PSD from the virgin surface (see in fig.4.3), after it was interacted with DNA, provides two correlation lengths, the persistence length (P) of 41.5 nm (at κ= 151 μm^{-1}) and the intermolecular separations between plasmid DNA (ξ) of 174.4 nm (at κ= 36 μm^{-1}). The value of persistence length for DNA, obtained here, is consistent with the values reported in literature [26]. After the interaction of DNA with the surface, sputtered at lower fluence (6×10^{15} ions/cm^2), the correlation lengths were found to be P= 67.5 nm (at κ= 93 μm^{-1}) and ξ= 261.6 nm (at κ= 24 μm^{-1}). Interaction of DNA with surfaces sputtered at higher fluence (1.8×10^{16} ions/cm^2) also leads to two correlation lengths P= 89.7 nm (at κ= 70 μm^{-1}) and ξ= 483.0 nm (at κ= 13 μm^{-1}). The results indicate that both the correlation lengths, P and ξ, become larger, increasing with fluence, on the ion sputtered surfaces. The increased persistence length (P) indicates an enhanced stiffness and so higher interaction of the DNA molecule on the sputtered surfaces. The larger intermolecular separations (ξ) also suggest more interaction as well as an increased biocompatibility and hydrophilicity of the sputtered surfaces.

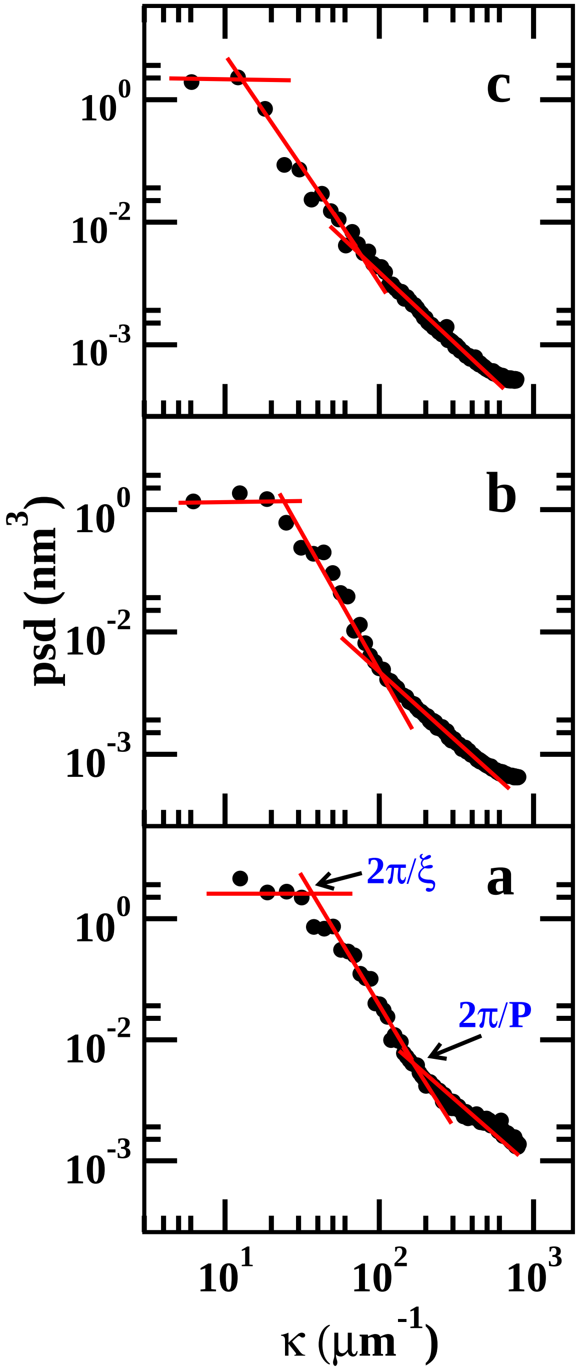

Figure 4.3: 1D-iso PSD plot from DNA interacted with (a) Virgin TiO_2 and surfaces irradiated with fluences of (b) 6×10^{15} ions/cm^2, and (c)1.8×10^{16} ions/cm^2.

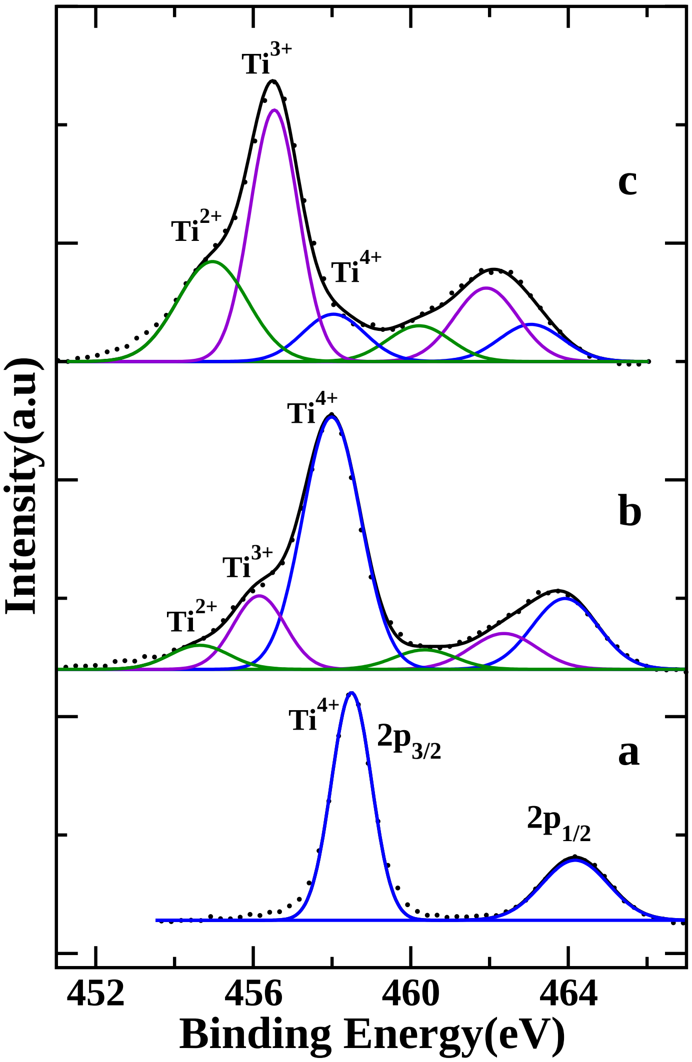

Figure 4.4: XPS spectra of Ti(2p) region for (a) virgin TiO_2 and surfaces irradiated with fluences of (b) 6×10^{15} ions/cm^2, and (c) 1.8×10^{16} ions/cm^2.

Figure 4.4 displays the Ti(2p) region of the XPS spectra from the virgin as well as ion irradiated surfaces. XPS spectrum from the virgin sample (in fig. 4.4(a)) shows the presence of the two spin orbit split Ti-2p features, $2p_{3/2}$ and $2p_{1/2}$. Both these features correspond to Ti^{+4} coordination sites on rutile surface. Very small amount of Ti^{3+} component may also be present on the surface of virgin sample. After irradiation of TiO_2 surface with 6×10^{15} ions/cm^2, in addition to Ti^{+4} sites, Ti^{+3} and Ti^{+2} features are also observed for both $2p_{3/2}$ and $2p_{1/2}$ states. However, Ti^{4+} component is most prominent with the ratio of Ti^{3+} and Ti^{4+} features being only about 0.3, as seen in fig. 4.5. For the surfaces, sputtered at the higher fluence, (1.8×10^{16} ions/cm^2) this ratio increases significantly to ~ 4.1 with the Ti^{3+} component becoming stronger than the Ti^{4+} (fig. 4.4(c) and fig. 4.5). The binding energy (BE) positions for various components of the $2p_{3/2}$ level, for virgin and the sputtered surfaces, are mentioned in Table 4.1 for unreacted surfaces as well as after their interaction with DNA.

Table 4.1: Binding Energy positions for various $2p_{3/2}$ states of TiO_2

	Ti^{+4}	Ti^{+3}	Ti^{+2}
Unreacted			
Virgin	458.5	-	-
6.0×10^{15} ions/cm^2	458.0	456.2	454.6
1.8×10^{16} ions/cm^2	458.0	456.5	455.0
Reacted with DNA			
Virgin	458.0	-	-
6.0×10^{15} ions/cm^2	457.3	-	-
1.8×10^{16} ions/cm^2	457.8	-	-

The TiO_2(110) surface consists of alternating [001] direction rows of five fold coordinated Ti^{+4} and two fold coordinated bridging O^{2-}. Preferential sputtering of TiO_2 surface during ion beam irradiation creates oxygen vacancy with its two associated electrons getting transferred to the empty 3d orbitals of the neighboring Ti atom. This leads to the formation of two Ti^{3+} or one Ti^{2+} state on the surface [27, 28]. With preferential sputtering of oxygen, Ti rich zones also get created that become the nucleation centers for the nanodots [13, 29–33]. Thus, the Ti^{3+} and Ti^{2+} features (in fig. 4.4(b)) are related to the excess O-vacancy that form on the TiO_2 surface after ion sputtering. Moreover, the higher irradiation fluence, 1.8×10^{16} ions/cm^2, leads to an increase in both, Ti^{2+} and Ti^{3+}, components as expected (see fig. 4.4(c)).

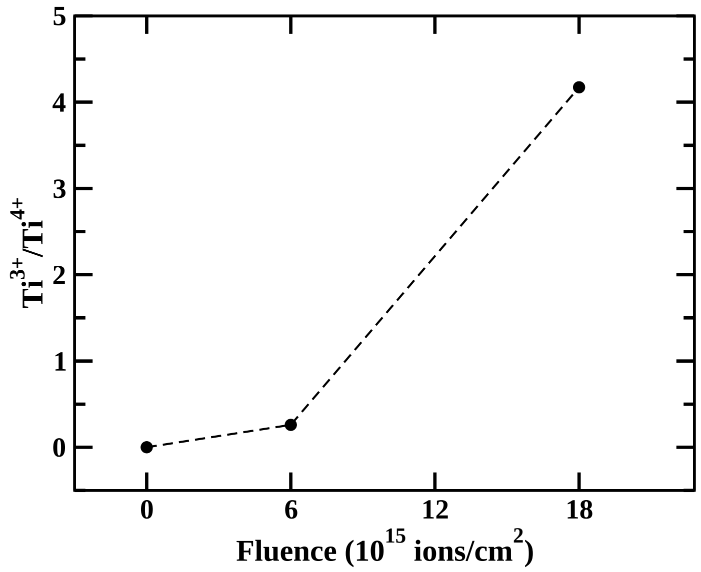

Figure 4.5: Ratio of Ti^{3+} and Ti^{4+} XPS intensities for the virgin and ion irradiated TiO_2 surfaces.

Figure 4.6 shows the XPS spectra of Ti(2p) region from the virgin and ion sputtered surfaces after they have been interacted with plasmid DNA. For reference, the XPS spectra (of fig.4.4) from the un-reacted surfaces have also been shown in this figure. The interaction of DNA with the virgin TiO_2 surface causes a slight shift of Ti^{4+} feature, compared to unreacted surface, towards the lower BE positions as seen in fig.4.6(a). This can be caused by the transfer of electrons from the negatively charged phosphate (PO_4^-) backbone of DNA to the surface. After DNA interacts with surface, irradiated with the smaller fluence (6×10^{15} ions/cm^2), the XPS results show a further shift of Ti^{4+} component towards lower BE indicating transfer of more electrons from DNA moiety to surface (fig. 4.6(b)). Gaining electron can impart some mixed (Ti^{3+} and Ti^{4+}) character to this state. Furthermore, it is noticed that there is no signature of any Ti^{2+} feature, after interaction, suggesting a saturation of this state after gaining electrons from DNA backbone (see fig. 4.6(b)). Both Ti^{3+} and Ti^{2+} states become saturated, as seen in fig. 4.6(c), after the interaction of DNA with surface irradiated at high fluence (1.8×10^{16} ions/cm^2). With these observations, it can be concluded that the initial transfer of electron from the DNA- phosphate backbone to the ion irradiated surfaces causes the saturation of Ti^{2+} and later of the Ti^{3+} states.

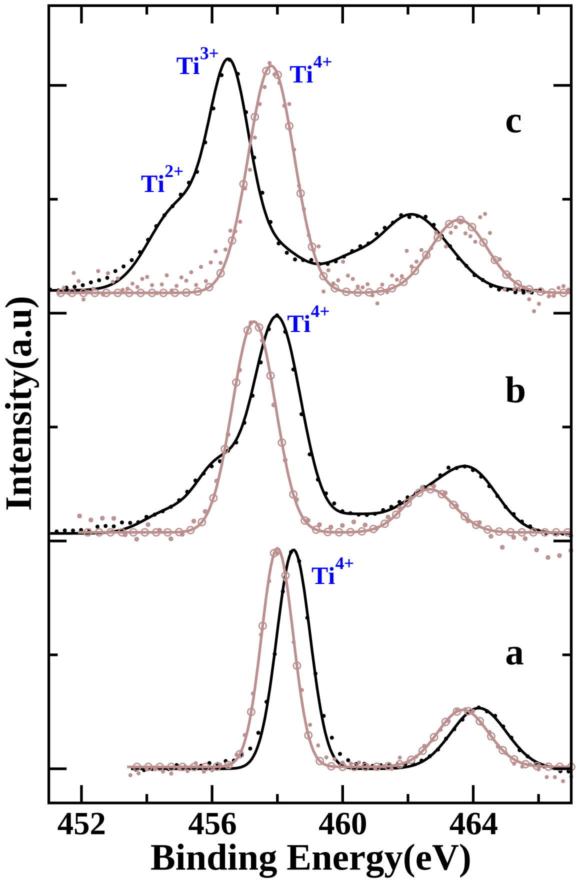

Figure 4.6: XPS spectra of Ti(2p) region for DNA interacted (red curve) surfaces of (a) virgin TiO_2 as well as surfaces irradiated with fluences of (b) 6×10^{15} ions/cm^2, and (c) 1.8×10^{16} ions/cm^2. For reference, XPS spectra from unreacted (black curve) surfaces are also included (see text).

The observed XPS results can be utilized to understand the AFM and PSD results discussed earlier in this chapter. On the virgin surface, the negative charge transferred from DNA is small leading to a relatively weak interaction between them. As a result the DNA exhibits a small size (in fig. 4.1,4.2), small internuclear separation (ξ) and small persistence length (P) (in fig. 4.3). An increased charge transfer, from DNA to surface, irradiated at small fluence (6×10^{15} ions/cm^2), is observed which saturates the Ti^{2+} sites of the surface. The presence of oxygen vacancies on the ion irradiated surfaces are responsible for the enhanced interaction, resulting in an increased size of plasmid DNA along with a larger ξ and P. Further increase in the diameter of plasmid DNA and larger morphological parameters, ξ and P, are observed after plasmid DNA interacts with the surface irradiated at higher fluence (1.8×10^{16} ions/cm^2). As the XPS results show, at this stage, charge transfer from DNA is strong enough to saturate both Ti^{3+} and Ti^{2+} states. The oxygen vacancies created on the surface, after irradiation, result in a strong conjugation of the DNA with the surface. Thus, ion irradiation leads to enhanced biocompatibility and hydrophilicity, increasing with fluence, of TiO_2 surfaces.

4.4 Summary and Conclusion

Here, the interaction of plasmid DNA with ion beam modified TiO_2 surfaces has been investigated. Results indicate that the diameter of the DNA as well as its morphological parameters, ξ and P, increase on the ion irradiated TiO_2 surfaces, indicating a higher biocompatibility and hydrophilicity, increasing with fluence, on these surfaces. An increased charge transfer from negatively charged phosphate backbone of DNA to the ion irradiated surfaces is observed to be crucially responsible for the observation of these properties. Oxygen vacancies created during ion irradiation become the significant centres which promote the conjugation of DNA with the surface.

References

[1] Davis, J. and Hayes, K., Geochemical Processes at Mineral Surfaces, American Chemical Society, Washington DC (1986).

[2] Stumm, W. (1992) Chemistry of the Solid-Water Interface: Processes at the Mineral-Water and Particle-Water Interface in Natural Systems, Wiley, New York.

[3] Sverjensky, D.A., Jonsson, C.M., Jonsson, C.L., Cleaves, H.J., and Hazen, R.M., Environ. Sci.Technol. 42:6034-6039 (2008).

[4] H. James Cleaves, Caroline M. Jonsson, Christopher L. Jonsson, Dimitri A. Sverjensky, and Robert M. Hazen, ASTROBIOLOGY, Volume 10, Number 3, 2010.

[5] Roger J. Narayan, Nancy A. Monteiro-Riviere, Robin L. Brigmon, Michael J. Pellin, Jeffrey W. Elam, Journal of the Minerals, metals, and Materials Society, June 2009, Volume 61, Issue 6, pp 12-16.

[6] Aillon KL, Xie Y, El-Gendy N, Berkland CJ, Forrest ML, Adv Drug Deliv Rev. 61: 457-466 (2009).

[7] H. Luckey, F. Kubli, Titanium Alloys in Surgical Implants, ASTM 796, 1981.

[8] J. Marciniak, Biomaterials, Technical University of Silesia Press, 2002.

[9] E. Krasicka-Cydzik, K. Kowalski, I. G..azowska, Proceedings of the 3rd Central European Conference “Chemistry Towards Biology” CHTB 2006, Cracow, 2006.

[10] T. Hanawa, O. Mamoru, Biomaterials 12 (1991) 767.

[11] Y.T. Sul, Biomaterials 24 (2003) 3893-3907.

[12] R. M Bradley and J. M. E. Harper, J. Vac. Sci. Technol. A, 6, 2390 (1988).

[13] S. Facsko, T. Dekorsy, C. Koerdt, C. Trappe, H. Kurz, A. Vogt, and H. L. Hartnagel, Science, 285, 1551 (1999).

[14] Purohit, P. K., J. Kondev, and R. Phillips., Proc. Natl. Acad. Sci. USA. 100, 3173 (2003).

[15] "DNA Packaging in Bacteriophage: Is Twist Important ?", Andrew James Spakowitz and Zhen-Gang Wang, Division of Chemistry and Chemical Engineering, California Institute of Technology, Pasadena, California 91125.

[16] Ullner, M.; Woodward, C. E. Macromolecules 2002, 35, 1437.

[17] O. Kratky and G. Porod, Rec. Tray. Chim. 68, 1106 (1949).

[18] Claudio Rivetti, Chip Walker, and Carlos Bustamante, J. Mol. Biol. (1998) 280, 41-59.

[19] Claudio Rivetti, Martin Guthold, and Carlos Bustamante, J. Mol. Biol. (1996) 264, 919-932.

[20] L.D. Landau, E.M. Lifshitz, Theory of Elasticity. Vol. 7 (3rd ed.) (1986).

[21] J. F. Marko and E. D. Siggia, Macromolecules 28, 8759 (1995).

[22] Dill, K.; Bromberg, S., Garland Science: New York, NY; Vol. 1, Chapter 32, p 609 (2003).

[23] Annalisa Calò, Pablo Stoliar, Eva Bystrenova, Francesco Valle, and Fabio Biscarini, J. Phys. Chem. B, 113, 15, (2009).

[24] Ph. Dumas, B. Bouffakhredine, C. Amra, O. Vatel, E. Andre, R. Galindo, and F. Salvan, Europhys. Lett. 22, 717 (1993)

[25] F. Biscarini, P. Samortz, O. Greco, and R. Zamboni, Phys. Rev. Lett., 78 (1997) 2389.

[26] C. Bustamante, J. F. Marko, E. D. Siggia, and S. Smith, Science 265, 1599 (1994).

[27] Subrata Majumder, D. Paramanik, V. Solanki, B.P. Bag, and Shikha Varma, App. Phys. Lett., 98, 053105 (2011); Subrata Majumder, D Paramanik, V Solanki, I Mishra, D.K. Avasthi, D. Kanjilal, and Shikha Varma, Appl.Surf.Sci., 258, 4122-4124 (2012).

[28] V.E.Henrich, G. Dresselhaus, and H.J. Zeiger, Phys. Rev. Lett., 36, 1335 (1976).

[29] M. Nozu, M. Tanemura, and F. Okuyama, Surf. Sci. Lett., 304, L468 (1994).

[30] F. Frost, A. Schindler, and F. Bigl, Phys. Rev. Lett., 85, 4116 (2000).

[31] S.K. Tan, and A.T.S. Wee, J. Vac. Sci. Technol. B, 24, 1444 (2006).

[32] D. Paramanik, S. R. Sahoo, Subrata Majumder and Shikha Varma, Vacuum, 84, 602 (2010).

[33] D. Paramanik, S.N. Sahu, and Shikha Varma, Jour. Phys. D-Appl. Phys., 41, 125308 (2008).

Chapter 5

ZnO Nanostructures : Their Magnetic Properties and Interaction with DNA

5.1 Magnetic Properties of ZnO Nanostructures

5.1.1 Introduction

In recent years, the development of semiconductor-magnetic materials have initiated enormous scientific interest due to their novel and versatile applications in memory, optoelectronic and spintronics devices. Since the semiconductor property promotes high speed data transfer where as the magnetic property effects storage of data information, the combination of these two properties can lead to a faster and cheaper electronic devices. The main challenge of these materials is to preserve their magnetic behavior beyond the room temperature for technological application. In the last few years, extensive research is ongoing for the development of such magnetic-semiconductor materials mainly by minute(5%) doping of transition metal magnetic impurities into semiconductor and insulator oxide thin films such as ZnO, TiO_2, SnO_2, In_2O_3, CeO_2 etc. termed as Dilute Magnetic Semiconductors (DMS) [1]. The main reason for the development of ferromagnetism in the magnetic-semiconductor materials was thought to be due to the magnetic doping [2–4] caused by the segregation of metallic clusters [5] and double exchange interactions mediated by electrons in different valance states of the impurities [6, 7].

Very recently, studies on some non-magnetic semiconductor materials like HfO_2, CaO, SiC [8–10] have shown that the ferromagnetism can also arise in non-magnetic semiconductor thin films without any magnetic doping even at room temperature, although their bulk materials show diamagnetic or paramagnetic behavior. In some other recent works, it has been shown that the magnetism in DMS thin films and nanoparticle systems does not exclusively depend on the magnetic doping but strongly depends on the defects created during the growth process [11, 12, 15]. The ferromagnetism in these low dimensional non-magnetic semiconductor systems has been attributed mainly to their low dimensionality and the oxygen defects created at the surface and interface. It has been suggested that the development of magnetism in these non-magnetic semiconductor nanoparticles system is strongly dependent on the fabrication process and the environment during preparation.

ZnO nanostructures have attracted enormous scientific interest in recent years because of their potential applications in UV, Optoelectronics and data storage devices. ZnO has a wide band gap of 3.37 eV and large exciton energy of 60 meV at 300 K which proves its superiority compared to GaN.

The present chapter discusses the room temperature ferromagnetic behavior of undoped ZnO nanostructures. ZnO nanostructures have been grown here by physical vapor deposition (PVD) method. The results show that although isolated magnetic domains displaying large coercivity are observed for small ($\sim$90 nm) ZnO nanostructures, long range magnetic ordering and smaller coercivity is observed for the bigger ($\sim$270 nm) nanostructures. It is further observed that the nanostructures are semiconducting in nature and the room temperature ferromagnetism, as exhibited by these nanostructures [13, 14], is mainly due to the presence of Oxygen vacancies. Interaction of ZnO nanostructures with DNA has also been investigated and it is observed that the DNA is more stable on the surface with larger nanostructures.

5.1.2 Experiments

ZnO nanostructures (NS) have been grown by physical vapor deposition (PVD) method. ZnO films of thickness 500nm and 1000nm were grown on Si(100) wafer. The films were observed to be discontinuous and displayed nanostructures. Average size of nanostructures observed for 500nm thick film was ∼90nm (small NS), whereas the average size was found to be ∼270nm (large NS) for the thicker 1000nm film. Deposition was performed by heating a (1:1) mixture of ZnO powder (99%) and graphite at 900° C in a system with a base pressure of $1 \times 10^{-5}\ mbar$. The graphite serves as the catalyst which can reduce the melting point of bulk ZnO powder below 900°C. ZnO nanostructures have been characterized by Atomic Force Microscopy (AFM), Magnetic Force Microscopy (MFM), Magneto-Optical Kerr Effect (MOKE), X-ray Photoelectron Spectroscopy (XPS), Photoluminescence (PL), Rutherford Back Spectrometry (RBS) and X-ray diffraction (XRD). For XPS studies a VG system equipped with Mg-Al K_α anode was utilized. XPS results reported here were acquired using the Al K_α anode. AFM-MFM studies were performed using a Nanoscope III-A controller supplied by Veeco. Images have been acquired in tapping mode using a FESP tip. MOKE studies have been performed using a He-Ne laser source in the longitudinal mode at room temperature. PL studies were performed using a Hg (370 nm) excitation source at room temperature and the XRD measurements were performed using a Cu K_α radiation source.

5.1.3 Results and Discussions

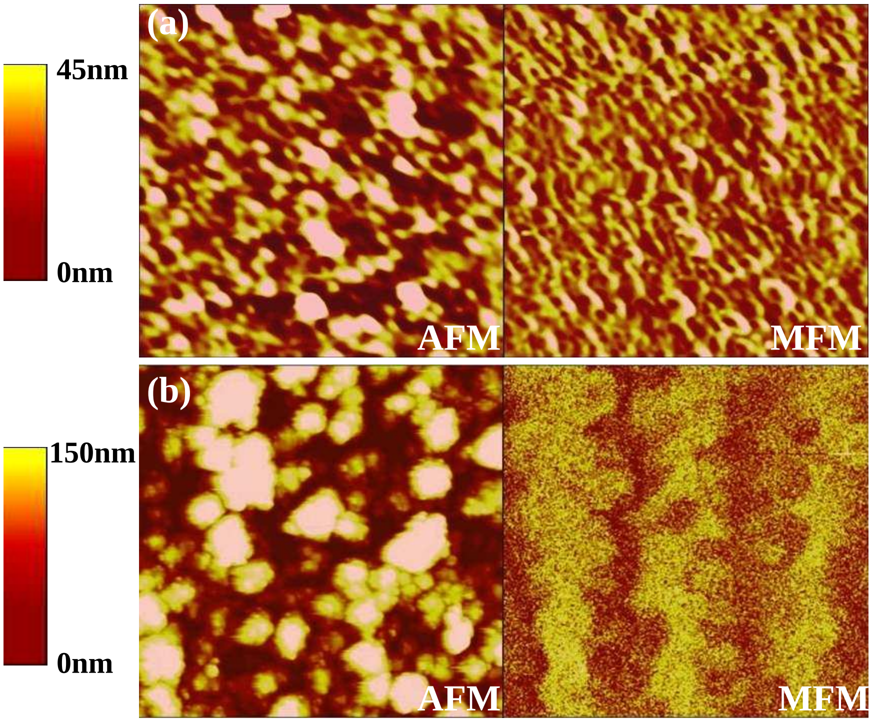

Figure 5.1: AFM-MFM images from $5\mu m \times 5\mu m$ regions are shown for (a) small NS (∼90 nm) and (b) large NS (∼270 nm) ZnO nanostructures. Topography and MFM images are shown in the left and right sections, respectively. Scale bars for topographic images are also shown.

Figure 5.1(a) shows the AFM image from a 500 nm thick ZnO film. Images show the presence of nanostructures on the surface. The average size of these ZnO nanostructures (small NS) is about 90 nm. The corresponding MFM image shows the isolated magnetic domains from ZnO film. Figure 5.1(b) shows the AFM-MFM images from the 1000 nm thick film. The average size of ZnO nanostructures is ∼270 nm (large NS). Interestingly, the magnetic domains in the MFM image do not appear isolated any more and show long range ordering. From fig. 5.1 it is clear that the small ($\sim 90\ nm$) ZnO nanostructures show isolated magnetic domains with short range exchange interaction which transforms to long ranged magnetic ordering when the ZnO nanostructures grow bigger (∼270 nm) in size.

The results of MOKE studies are shown in fig. 5.2. Both the small NS ($\sim$90 nm) and large NS ($\sim$270 nm) show ferromagnetic behavior at room temperature although it is well known that the bulk ZnO is diamagnetic in nature [16]. The hysteresis loop from small $\sim$90 nm nanostructures shows a coercivity of 520 Oe which reduces to 230 Oe for the larger $\sim$270 nm nanostructures. This can be because the larger ZnO nanostructures, can reduce the domain wall pinning effect and in turn decrease the coercivity [17]. The reduction of pinning will increase the range of exchange interaction among the neighboring localized electron spin moments in the ferromagnetic domains leading to the long range of order seen for large nanostructures in MFM. For the small nanostructures of $\sim$90 nm, only short range of exchange interaction is observed. Another interesting feature shown by MOKE results, in fig. 5.2, is the asymmetries in the hysteresis loops for both the small NS and large NS. These asymmetric loops can arise due to collinear uniaxial and unidirectional anisotropies in the magnetic field applied at the certain angles to the anisotropy axes of the nanostructures and the local strains. Such asymmetry is often imperceptible on longitudinal hysteresis loops, especially for nanostructures with small uniaxial anisotropy [17, 18].

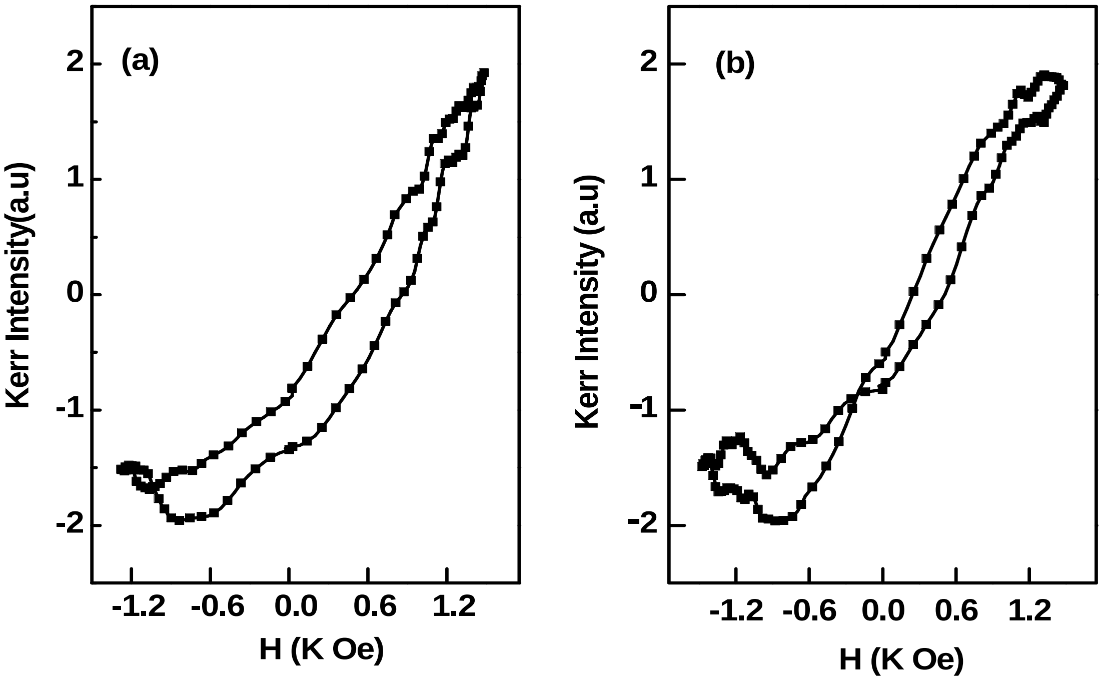

Figure 5.2: Hysteresis loop for (a) small NS (∼90 nm) and (b) large NS (∼270 nm) ZnO nanostructures. Kerr intensity versus magnetic field (H) has been plotted.

Various irregularties in the hysteresis curve are caused by the inhomogeneities in the nanostructures and the other defects at the surface which impede the motion of Domain Wall (DW) in the film. This is related to the phenomenon of Barkhausen effect, where the DW can remain pinned to the inhomogeneities even with the change in magnetic field but jumps off and becomes unpinned on subsequent change in field [19].

The origin of ferromagnetism can be attributed to the point defects present in undoped ZnO nanostructures [20]. The defects can be either of Zn or O type and may arise as vacancies or interstitials depending upon the fabrication process. The physical vapor deposition method preferentially creates vacancies rather than interstitials and the Oxygen vacancies(V_o) are likely to be more in number than the Zn vacancies(V_{zn}) [21] due to their high diffusivity in oxide systems, which occurs specially at the surface and interfaces. The charge states of these V_o vacancies can be of (+2), (+1) or (0). The theoretical calculation for ZnO type structures show that (+2) and (0) charge states create relatively larger local strain in the lattice sites than (+1) state [22]. Hence, the Oxygen vacancies in ZnO are preferentially in the (+1) charge state. The electrons trapped in the Oxygen vacancies are polarized which are assumed as the origin of the room temperature ferromagnetism in undoped ZnO nanostructures.

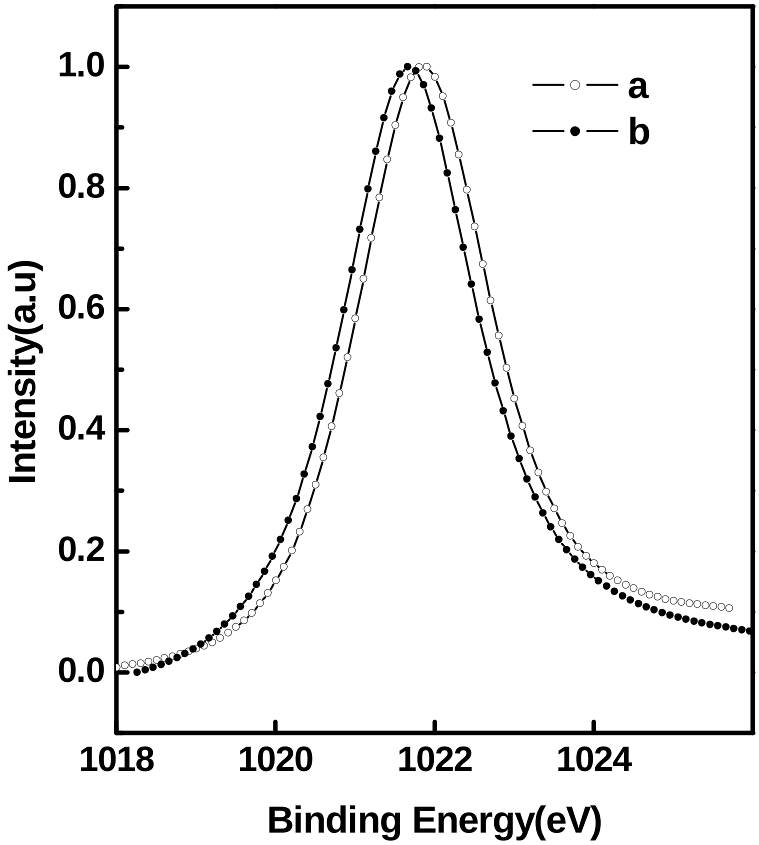

Figure 5.3: Core level XPS spectra for Zn(2p$_{3/2}$) level from (a) small NS ($\sim$90 nm) and (b) large NS ($\sim$270 nm).

The Zn(2p) state for the ZnO nanostructures has been investigated by the XPS and is shown in fig. 5.3 for both the small (∼90 nm) and large (∼270 nm) nanostructures. The binding energy (BE) of Zn($2p_{3/2}$) state at 1021.7 eV for large (∼270 nm) nanostructures is about 0.2 eV lower than the position of this state (1021.9 eV) for small (∼90 nm) nanostructures. Lower BE seen for large nanostructures (∼270 nm) can be due to the increased screening effect of the valence electrons at the Zn sites after the reduction in charge transfer from Zn to O caused by the presence of excess Oxygen vacancies in the ZnO crystals at the surfaces and interfaces.

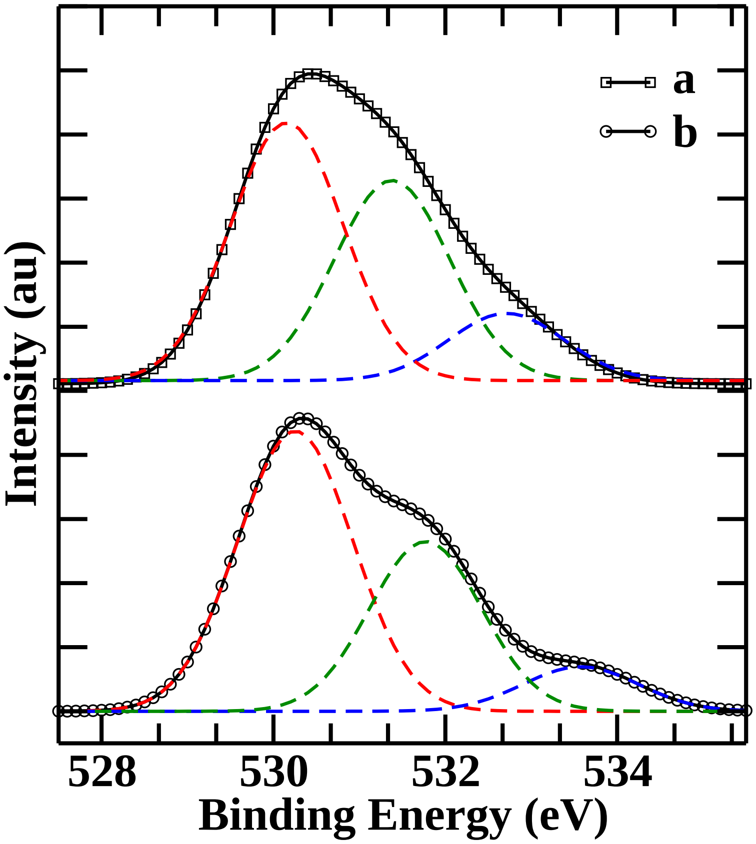

Figure 5.4: Core level XPS spectra for O(1s) level from (a) small NS (∼90 nm) and (b) large NS (∼270 nm).

The O1s spectra for both small and large ZnO nanostructures are shown in fig. 5.4. The spectra for small NS ($\sim$90 nm) displays three components at 530.2, 531.4 and 532.7 eV. The lowest binding energy component centered at 530.2 eV is attributed to O^{2-} ion from ZnO [23,24]. The high binding energy components located at 531.4 and 532.7 are attributed to the presence of loosely bound oxygen on the surface of ZnO nanostructures belonging to species like hydroxides [25]. The corresponding features from the large nanostructures ($\sim$270 nm) are respectively observed at 530.3, 531.7 and 533.6 eV. Increased BE for all oxygen components, for large nanostructures (compared to small nanostructures) are consistent with the presence of oxygen vacancies on the surface and a decreased screening effect on oxygen atoms.

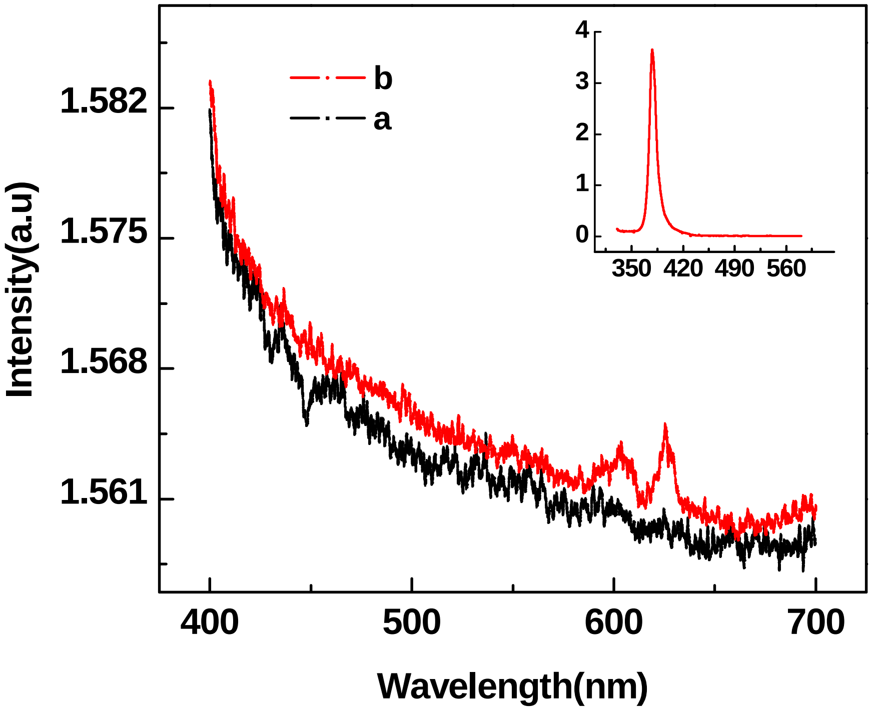

Figure 5.5: PL spectra from (a) small NS ($\sim$90 nm) (lower) and (b) larger NS ($\sim$270 nm) (upper). The inset shows the emission at 376 nm due to the semiconducting band gap of 3.37 eV for large NS.

Photoluminescence results (fig. 5.5) clearly support the presence of excess vacancies for large nanostructures (∼270nm) compared to small (∼90nm) nanostructures. The features at 610 nm and 630 nm, representing the yellow and red wavelengths respectively, are attributed to the emission due to the direct recombination of the photo generated charge carriers generated at the oxygen vacancy sites to the valance band state of Zn sites. Both these features being stronger for the large nanostructures, compared to the small nanostructures, support the XPS results that excess Oxygen vacancies are present in the bigger (∼270 nm) nanostructures. The XPS studies did not show presence of any material other than Zn or O which support the fact that the level of impurities (of any kind) is less than 0.01%. The magnetic moment associated with that very minute doping impurities, if at all present, will be very small which can not create the strong ferromagnetism seen here. The large nanostructures (∼270 nm) displaying long range magnetic ordering with small coercivity of 230 Oe also show semiconducting behavior. The inset of fig. 5.5 shows the 376 nm emission due to the semiconducting ZnO band gap of 3.37 eV for these nanostructures. This PL measurement was done using a 325 nm He-Cd laser source. XRD results from the large nanostrctures (∼ 270nm) thin film is represented in fig. 5.6. The spectra show the presence of ZnO (100), (101), (102), and (002) phases. This shows the nanostructures are composed of ZnO only [26].

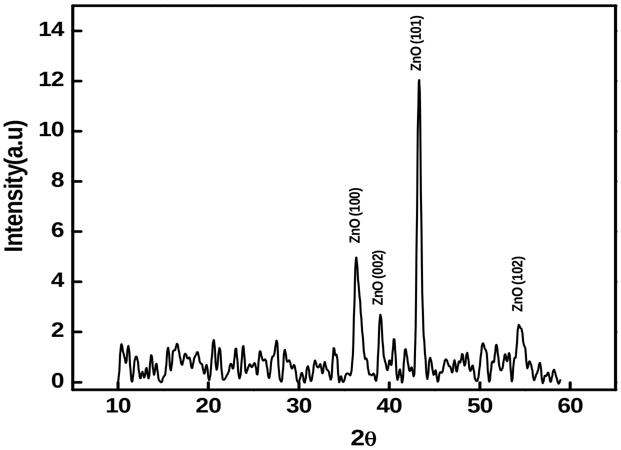

Figure 5.6: XRD spectra for large (∼270 nm) ZnO nanostructures.

5.2 Interaction of DNA with ZnO Nanostructures

We have investigated the interaction of λDNA with the large (∼270 nm) and small (∼90 nm) ZnO nanostructures. The fabrication of nanostructures was discussed in the previous section. The λDNA, utilized in this study contained about 48K base pairs. The concentration of the λDNA was maintained at 0.03ng/nl and it was stored in the 10ml Tris-Hcl buffer (pH 7.6) at -20°C.

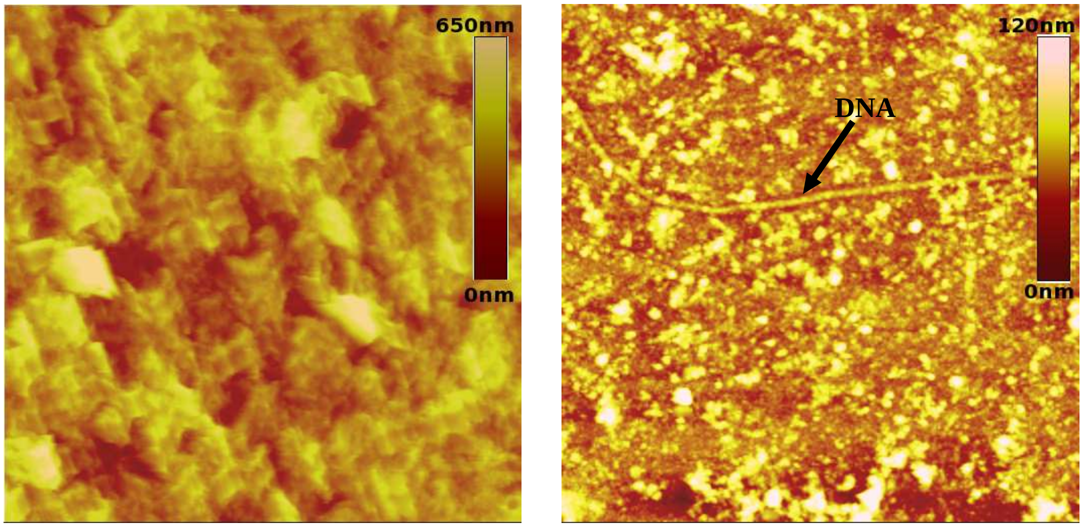

(a) (b)

Figure 5.7: AFM topographic images of λDNA interacted with (a) small NS (∼90nm) and (b) large NS (∼270nm). The scan size of the images is $10 \times 10 \mu m^2$.

Figure 5.7a displays the AFM image after the interaction of the λDNA with small (∼90 nm) nanostructures of ZnO. The image indicates an agglomeration of DNA due to the nanostructures. The rms roughness of the surface has been measured to be 88.7 nm. Surprisingly, the DNA does not agglomerate on the surface with larger (∼270nm) ZnO nanostructures rather at many places long strands of DNA are observed. One such region is shown in fig. 5.7b. The rms roughness of the surface is seen to be very low (18.8 nm).

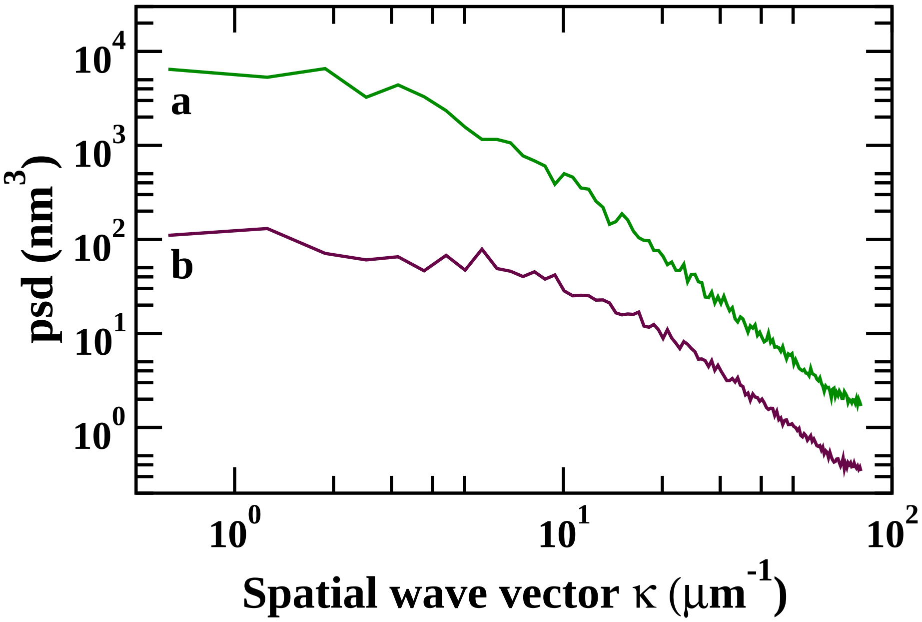

Figure 5.8: PSD plots after interaction of DNA with (a) small NS (∼90nm) and (b) large NS (∼270nm).

The Power Spectral Density plots after the interaction of λDNA with smaller (∼90nm) and larger (∼270nm) ZnO nanostructures are shown in fig. 5.8. The PSD plots also show the roughness comparison of the two surfaces interacted with λDNA. Considering the behavior of $PSD(\kappa)$ with κ, as $PSD(\kappa) = A[1 + B^2\kappa^2]^{-(1+c)/2}$, the slope for $PSD(\kappa \simeq 0)$, gives the equivalent surface *rms* roughness. The roughness values derived from PSD plots are relatively similar to those obtained from AFM images. High *rms* roughness is observed on surface with small (∼ 90nm) nanostructures. The results presented here display that λDNA is very stable on large (∼270nm) nanostructures. The overall surface roughness is also lower on this surface. However, after interaction with smaller (∼90nm) nanostructures DNA agglomerates resulting in a surface which is not desireable for DNA applications.

5.3 Summary and Conclusion

In this chapter, ZnO nanostructures produced by PVD method are discussed. These nanostructures are semiconducting in nature and display room temperature ferromagnetism. Isolated magnetic domains for smaller ZnO nanostructures but long range magnetic ordering with exchange interactions is observed for larger nanostructures. Ferromagnetism may be primarily arising due to the presence of Oxygen vacancies in the ZnO nanostructures. The photonic properties of these ZnO nanostructures are strongly affected by the Oxygen vacancies as has been shown by XPS and PL studies. The interaction of DNA with ZnO nanostructures has also been investigated here. The DNA remain stable on larger nanostructures but agglomerates on the smaller nanostructures.

References

[1] T. Dietl, H. Ohno, F. Matsukur, J. Cibert and D. Ferrard, Science, 287, 1019 (2000).

[2] D. P. Norton, M. E. Overberg, S. J. Pearton, K. Pruessner, J. D. Budai, L. A. Boatner, M. F. Chisholm, J. S. Lee, Z. G. Khim, Y. D. Park, and R. G. Wilson, Appl. Phys. Lett., 83, 5488 (2003).

[3] P. Sharma, A. Gupta, K. V. Rao, F. J. Owens, R. Sharma, R. Ahuja, J. M. O. Guillen, B. Johansson and G. A. Gehring, Nat. Mater., 2, 673 (2003).

[4] M. Venkatesan, C. B. Fitzgerald, J. G. Lunney, and J. M. D. Coey, Phys.Rev.Lett., 93, 177206 (2004).

[5] S. R. Shinde, S. B. Ogale, J. S. Higgins, H. Zheng, A. J. Millis, V. N. Kulkarni, R. Ramesh, R. L. Greene, and T. Venkatesan, Phys.Rev.Lett., 92, 166601 (2004).

[6] S. D. Yoon, Y. Chen, A. Yang, T. L. Goodrich, Xu Zuo, D. A. Arena, K. Ziemer, C. Vittoria and V. G. Harris, J.Phy:Cond.Mat., 18, L355 (2006).

[7] M. A. Garcia, M. L. Ruiz-Gonzalez, A. Quesada, J. L. Costa-Kramer, J. F. Fernandez, S. J. Khatib, A. Wennberg, A. C. Caballero, M. S. Martin-Gonzalez, M. Villegas, F. Briones, J. M. Gonzalez-Calbet and A. Hernando, Phys.Rev.Lett., 94, 217206 (2005).

[8] M. Venkatesan, C. B. Fitzgerald and J. M. D. Coey, Nature, 430, 630 (2004).

[9] I.S. Elfimov, S. Yunoki and G.A. Sawatzky, Phys.Rev.Lett., 89, 216403 (2002).

[10] A.Zywietz, J.Furthmuller and F.Bechstedt, Phys.Rev.B, 62, 6854 (2000).

[11] K. R. Kittilstved, N. S. Norberg, and D. R. Gamelin, Phys.Rev.Lett., 94, 147209 (2005).

[12] Y. Gong, T. Andelman, G. F. Neumark, S. O'Brien, and I. L. kuskovsky, Nanoscale. Res. Lett., 2, 297 (2007).

[13] S. Majumder, D. Paramanik, A. Gupta, Shikha Varma, Appl. Surf. Sci., 256, 513-516 (2009).

[14] S. Majumder, V. Solanki, A. Gupta and Shikha Varma; Asian Journal of Physics, 19, 2 and3, 269-272 (2010).

[15] S. Larcheria, C. Armellinia, F. Roccaa, A. Kuzminb, R. Kalendarevb, G. Dalbac, R. Graziolac, J. Puransc, D. Pailhareyd and F. Jandardd, Superlattice Microst., 39, 267 (2006).

[16] A. Sundaresan, R. Bhargavi, N. Rangarajan, U. Siddesh, and C. N. R. Rao, Phys.Rev. B, 74, 161306(R) (2006).

[17] G. Bertotti, Hysteresis in Magnetism for Physicists, Materials Scientists, and Engineers, (Academic Press, California, USA, 1998).

[18] J. Camarero, J. Sort, A. Hoffmann, J.M. Garcia-Martin, B. Dieny, R. Miranda, J. Nogues, Phys. Rev. Lett., 95, 057204 (2005).

[19] H. Hauser, M. Evanzin, Sensors and Actuators A, 129, 231 (2006).

[20] M. A. Garcia, J. M. Merino, E. F. Pinel, A. Quesada, J. de la Venta, M. L. R. GonzÃąlez, G. R. Castro, P. Crespo, J. Llopis, J. M. GonzÃąlez-Calbet, and A. Hernando, Nano Lett., 7(6), 1489 (2007).

[21] F. A. Selim, M. H. Weber, D. Solodovnikov, and K. G. Lynn, Phys.Rev.Lett., 99, 085502 (2007).

[22] P. Erhart, K. Albe, and A. Klein, Phys.Rev. B, 73, 205203 (2006).

[23] Li Li, Liang Fang, Xian Ju Zhou, Zi Yi Liu, Liang Zhao, Sha Jiang, Journal of Electron Spectroscopy and Related Phenomena, 173, 7 (2009).

[24] N. Tabet, M. Faiz, A. Al-Oteibi, Journal of Electron Spectroscopy and Related Phenomena, 163, 15 (2008).

[25] B.J. Coppa, C.C. Fulton, P.J. Hartlieb, R. F. Davis, B. J. Rodriguez, B. J. Shields, and R. J. Nemanich J. Appl. Phys., 95, 5856 (2004).

[26] J.L. van Heerden, R. Swanepoel , Thin Solid Films, 299, 72-77 (1997).

Chapter 6

Fabrication of Hg Nanostructures within DNA: Demonstration of DNA as a sensor of Mercury

6.1 Introduction

Coming together of nanotechnology and bioengineering provide the template for designing useful nanostructures through the manipulation of biological molecules like de-oxy-ribo-nucleic-acid (DNA). These molecules exhibit great flexibility and have shown potential as precisely controllable and programmable scaffolds for designing, fabricating and organizing functional nanomaterials [1–7]. Metallic nanostructures (NS) have attracted much attention, since they show the distinctive physical and chemical properties found in neither bulk nor molecular/atomic systems. With the top down approach having several limitations in this frontier, role of DNA for assembling metal NS through their selectivity and specificity of binding nature can have far reaching consequences. The NS can in turn be utilized to modulate the properties and functions of the DNA. The DNA templated NS also show promise to become useful in bio electronic devices and sensors [8]. Mercuric metal ion as carcinogenic element, that perturbs and influences DNA structure, also imparts serious concern for understanding the binding of this divalent ion to DNA. A comparison of the toxicity values of different forms of mercury on the prokaryotes and eukaruyotes is shown in Table 6.1.

Table 6.1: Chemical toxicity values of *mercury* Hg^{2+}

Form of Mercury[a]	Non Cancer Effect	
	Oral-RfD[b]	*Inhalation-RfC*[c]
Metallic Mercury	None Established	0.0003 mg/m^3
Mercuric Chloride	0.0003 mg/Kg-day	None Established
Methyl Mercury	0.0001 mg/Kg-day	None Established
Phenyl Mercuric Acetate	0.00008 mg/Kg-day	None Established

[a] Adapted from Health Fact Sheet, NIH, USA
[b] RfD: Reference Dose
[c] RfC: Reference Concentration

In this chapter, the fabrication of mercuric NS within the DNA scaffold by utilizing the site specific interactions [9, 10] is demonstrated. The Hg-NS are embedded within double helix and exclusively interact with the nucleic acid bases of DNA. In addition, protonation of amine group (see fig. 6.1), promotes the formation of metal-base complexes (like Metal-Purine (M-Pu) and Metal-Purine-Pyrimidine (M-Pu-Py)). Stabilization energy estimates suggest that G-C base pair sites are the likely candidates in the formation of these complexes. Formation of metal-base complexes as well as the modifications in transport (electrical) properties of DNA, after conjugation with Hg ions, can be utilized as sensor of mercury contamination and DNA assays.

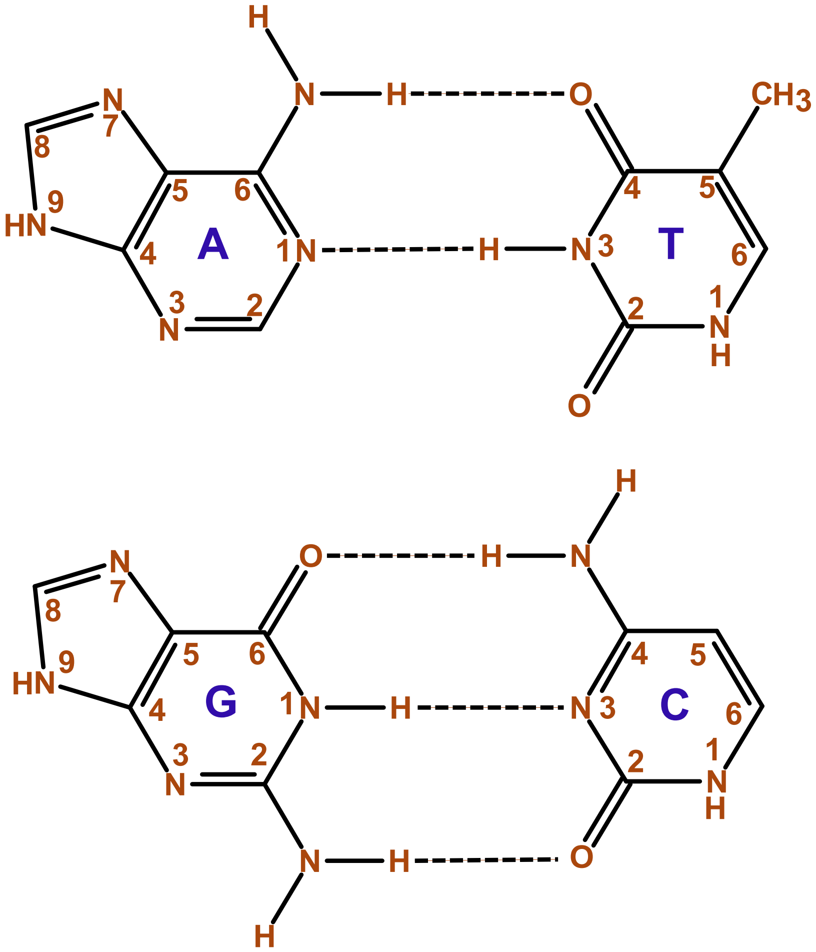

Figure 6.1: Structure of Watson-Crick (top) Adenine (A)-Thymine (T) and (below) Guanine (G)-Cytosine (C) base pairs. (Pu: A,G; Py: T,C).

6.2 Experimental

Plasmid (pBSIISK with ∼ 3400 base pairs) DNA was isolated from the bacterial cell(DH5α) in mid-log phase as per the standard protocol (Sambrook and Russell 2001) and was used in the present study. 2ng/μL DNA was reacted with 10mM mercuric acetate salt and EDTA solution. The Hg^{2+} ions created in the aqueous solution bind to DNA bases forming the complex NS and EDTA acts as the capping agent. Nanoscope IIIA multimode was utilized for tapping mode SPM and Scanning Tunneling Spectroscopy (STS) studies, of samples prepared by placing the solution of the un-reacted or the reacted DNA on the mica surface and then drying it under ambient conditions. Nearly 200 images of 50 nm to 10 μm sizes were imaged. XPS was performed on a VG instrument with a Mg Kα source at an emission angle of 30°. All binding energies are referenced to the C1s peak at 284.6eV. TEM images were acquired, utilizing a liquid nitrogen cell, in JEOL microscope.

6.3 Results and Discussion

Figure 6.2 show the AFM topographic images of the reacted as well as unreacted DNA's with the Hg. Image from the un-reacted DNA (fig. 6.2a) displays several circular plasmid DNAs of 200-500nm diameter. The reaction with Hg salt, however, linearizes the circular DNA plasmid as seen in fig. 6.2b where only linear DNAs, with their lengths varying from 0.2-1μm, are observed. A typical high resolution image from a linearized DNA (fig. 6.2c) displays several high intensity zones (marked by arrows) where the mercury NS, of 8-10nm sizes, have got embedded within the DNA. Local melting or denaturing of DNA may be responsible for this NS embedding since the double helix is undisturbed in the other regions where periodic bright spots representing 10 DNA base pairs units with, expected, helical pitch of $3.4 \pm 0.3 nm$ are observed.

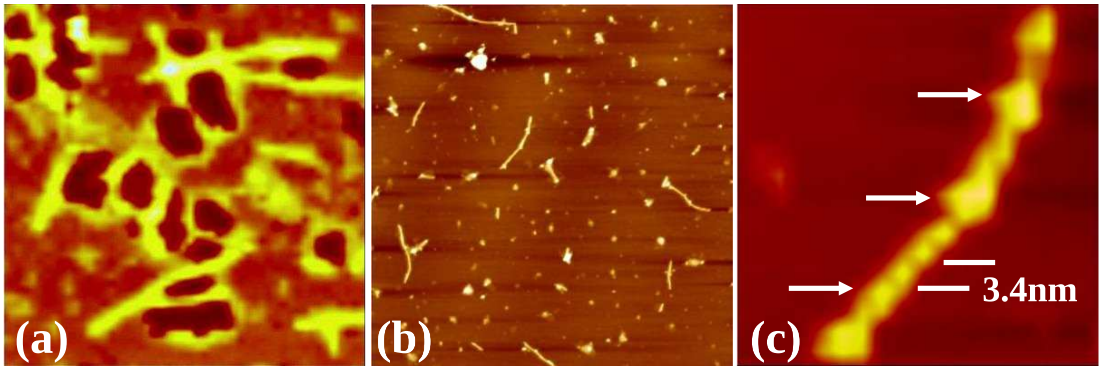

Figure 6.2: (a) $1 \times 1\ \mu m^2$ image of un-reacted DNA on mica. Images of DNA reacted with Hg ions are shown from (b) $5 \times 5\ \mu m^2$ and (c) $750 \times 750\ nm^2$ regions. Arrows mark the positions where Hg NS have got embedded within plasmid. The helical pitch of 3.4nm between the 10 base pairs of DNA is also marked.

The P-2p XPS spectra, in fig. 6.3a, do not exhibit any significant differences between the un-reacted or the metal reacted DNA. The scenario, however is very different for N1s core levels. The binding energies of the main features of P(2p), Hg(4f), and N(1s) are presented in Table 6.2. Prior to metal interaction, nitrogen N1s features (see Table 6.2) related to amino (-NH_2), imine (-N=) and amine (-NH-) structures [11, 12] are seen in fig. 6.3b. Although all these features are seen, after interaction of DNA with mercury, the spectrum is very broad and displays six features each of 1.5eV FWHM. The severe modifications in this spectrum suggest extensive perturbations in the DNA which in comparison with the absence of any modifications in P spectrum signifies the selective interaction of Hg ion with Nitrogen site of nucleic acid bases. Consequently the new nitrogen features (at 395.47, 403.09 and 405.57 eV) must have their origin in the conjugation of Hg- cation with DNA.

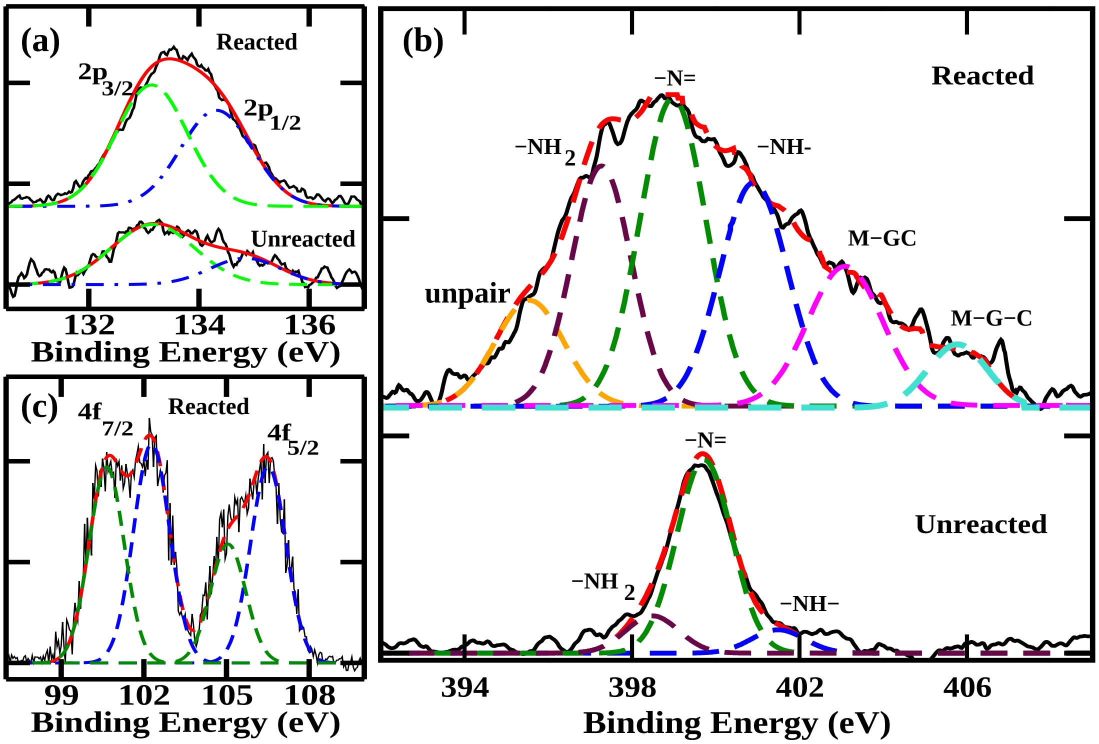

Figure 6.3: XPS spectra are shown from un-reacted (lower) as well as metal reacted DNA (upper) for (a) P2p, (b) N1s regions and from metal reacted DNA for (c) Hg4f. All XPS intensities are in arb. units.

Table 6.2: Binding Energy (eV) of Core Levels

	P2p		Hg4f			
	$2p_{3/2}$	$2p_{1/2}$	$4f_{7/2}$ M-G-C	$4f_{7/2}$ M-GC	$4f_{5/2}$ M-G-C	$4f_{5/2}$ M-GC
Unreacted	133.15	134.83	-	-	-	-
Reacted	133.15	134.32	100.65	102.28	105.05	106.51

	N1s					
	Unpair	$-NH_2-$	-N=	-NH-	M-GC	M-G-C
Unreacted	-	398.42	399.66	401.42	-	-
Reacted	395.47	397.26	398.97	400.90	403.09	405.57

The ab intio calculations, based on quantum chemistry, show that empty orbitals of transition metal cation on accepting electrons from the nucleobase moiety, with the N7 atoms of Purines (G,A) being the most preferred sites (see fig. 6.4), form coordination complexes [13]. Based on above observations, we propose, that the protonation of imine (N7) nitrogen causes, as also observed in polymers [14–16], the high BE feature at 403.09 eV (fig. 6.3b) due to the formation of Metal-Purine (M-Pu) complex. Furthermore, formation of more stabilized Metal-Purine-Pyrimidine (M-Pu-Py) complex, also proposed by ab initio model, produces the higher BE, 405.57 eV, feature. Although the theoretical feasibility of such metal-base complexes has been discussed by Burda etal. [13], this study presents the experimental verification of the formation of such complexes. The schematic of the Metal-Purine (M-Pu) and Metal-Purine-Pyrimidine (M-Pu-Py) complex inside the DNA bases are shown in fig. 6.4.

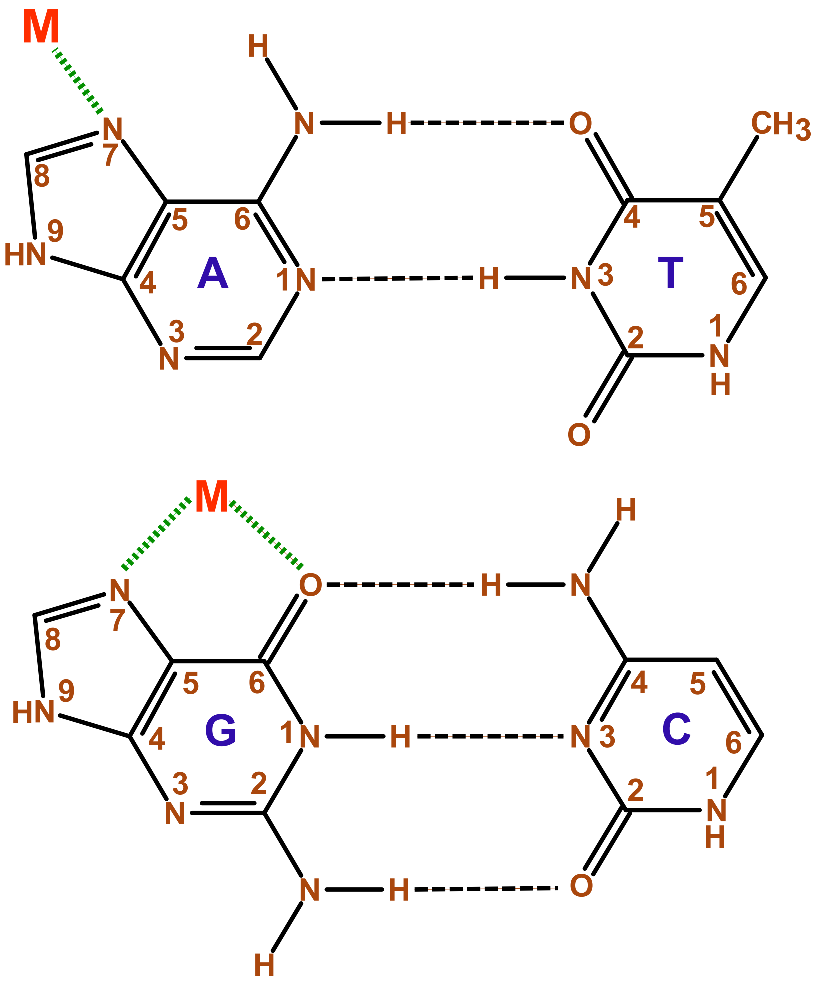

Figure 6.4: Possible Metal (M) attachment sites in Purine-Pyrimidine (Pu-Py) structure. Metal attachment to (top) AT and (below) GC complex.

The strong affinity of DNA for mercury ions, compared to Au nanoparticles [17], as suggested by the excessive perturbations in nitrogen signal (fig. 6.3b) promotes the local melting within DNA double helix. Consequently, some hydrogen bonds,between the DNA bases, get ruptured leading to the perturbations and the denaturing of the associated exocyclic groups (-NH, -NH_2, C=O) attached to these sites [18]. These exposed exocyclic groups produce the lowest BE "unpaired" 395.47 eV feature in fig. 6.3b. Thus 1.79 eV, the energy difference between the "unpaired" and the amino (-NH_2) features (in Table 6.2), reflects the energy required for stabilizing the base pair interaction.

Comparing with the quantum chemical calculations, where stabilization of G-C and A-T pairs respectively require 1.1 and 0.4 eV [13], it can be concluded that the "unpaired" feature is most likely due to the rupturing of hydrogen bonds of G-C base pairs in fig. 6.4. The intensity strengths, from XPS spectra, reveal that the ratio of "unpaired" bases is about half of paired amino group implying a significantly large number of unpaired sites for DNA in the presence of metal.

The ab initio calculations, under Hartree Fock (HF) formalism, have demonstrated that the stabilizing energy for Hg- Purine system, within M-GC (M-AT) complex is 8.5 eV (5.47 eV) whereas for Hg- Purine- Pyrimidine system is 10.37 eV (6.4 eV) for M-G-C(M- A-T) complexes [13]. Comparison with the post- conjugation XPS results, exhibiting extra N1s features at 403.09 and 405.57 eV (fig. 6.3b) displaying respectively a separation of 7.62 and 10.1 eV referenced to the "unpaired" bases (at 395.47 eV), suggests that these high BE features, are most likely due to the formation of M-GC or M- G-C complexes, respectively, and less likely due to M-AT and M-A-T complexes. Weak coordinations with adenine are, however, possible. Smaller dipole moments of adenine, compared to guanine, and its orientation can be responsible for a much weaker coordination to metal ion.

The Hg 4f spectrum (fig. 6.3c), displaying four features, also reflects the formation of metal-nucleobase complexes with $4f_{7/2}$ and $4f_{5/2}$ components respectively appearing at 102.28 and 106.51 eV for M-GC complex and at 100.65 and 105.05 eV for M-G-C complex. The higher intensity of former two features is in agreement with the results of fig. 6.3b with a more intense M-GC feature. Influence of electropositive Hg, as well as its nanostructure nature, causes the shift towards higher BE for these complexes compared to bulk metallic-Hg core levels expected at 99.7 ($4f_{7/2}$) and 103.8 eV ($4f_{5/2}$).

The scenario, based on the picture developed by AFM and XPS thus suggest that Hg NS get embedded within the nucleolic acid bases through their strong affinity, rather than by the encapsulation of NS by the major grooves of the DNA. The later process has been utilized by Liu etal [19] for forming Au clusters. The strong affinity of Hg ions for nitrogen bases also results in the formation of M-GC and M-G-C complexes. These complexes, or metal bound bases, then serve as additional nucleation sites for the stabilization of Hg-NS within DNA. These results highlight the possibility that Hg- NS could be assembled by DNA. The Hg- NS bound bases may link with other base acceptors allowing separated DNA strands, or their separated local domains to cross link forming a network of DNA aggregates as seen in the TEM image (fig. 6.5) where circular DNA aggregates can be delineated.

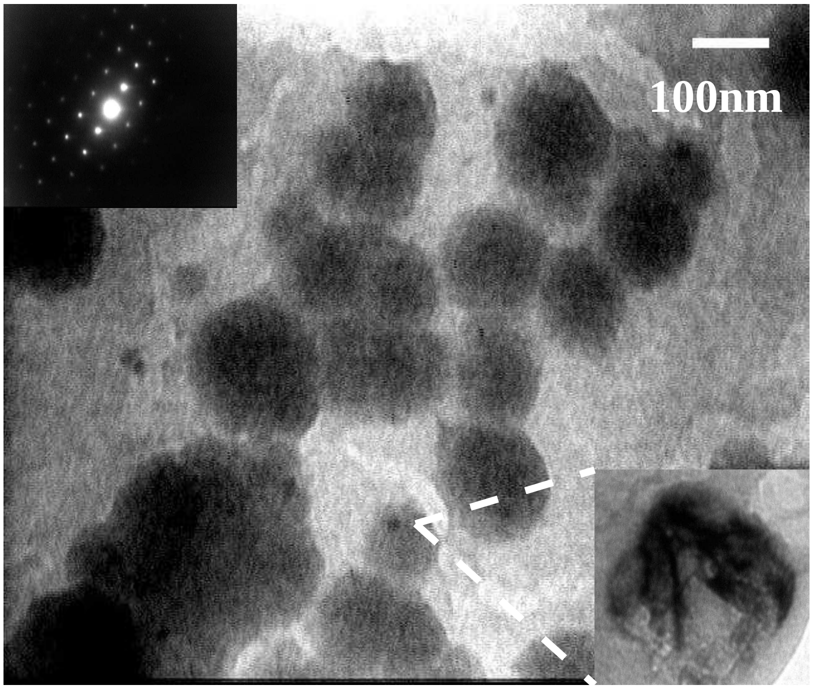

Figure 6.5: TEM image of aggregation of Hg NS conjugated DNA. Inset shows a cubic nanocrystal within the Hg- DNA aggregate. The SAD pattern from this nano-crystal (top-left inset) shows a lattice constant of 3.004Å.

Geometrically distinct shapes for aggregates have been observed in other studies also [17]. Inside these aggregates the cubic Hg NS (inset fig. 6.5) have been observed. The SAD pattern from a Hg crystallite, within the aggregate, displays an ordering of 3.004Å, similar as the lattice spacing for rhombohedral mercury crystal. Several other studies have previously addressed aggregation of DNA in the presence of divalent metal cations. These display a close correspondence between thermal and metal induced melting [18].

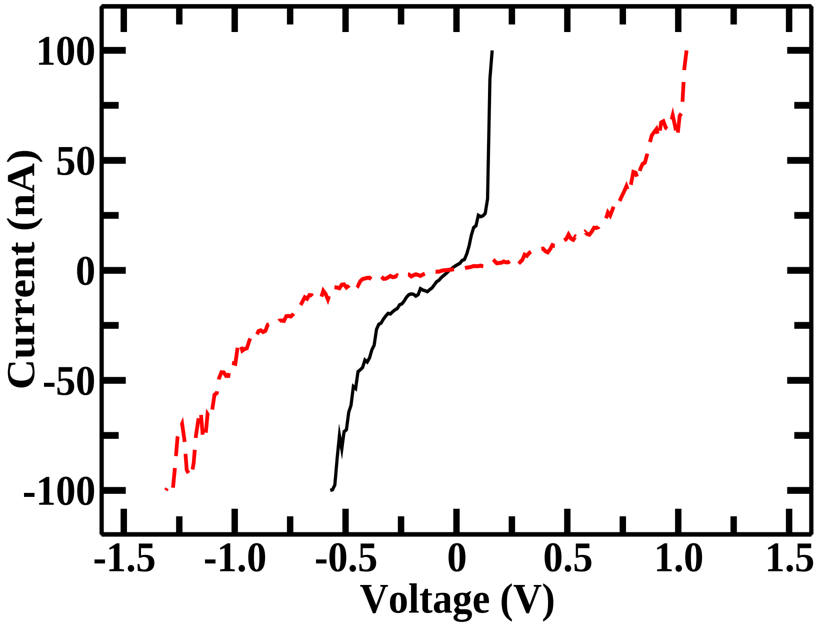

Figure 6.6: STS of bare DNA (straight line) as well as metal conjugated DNA (dashed line).

The STS images studied for the modifications in transport behavior exhibit a rectifying behavior for the Hg conjugated DNA in fig. 6.6. The bare plasmid, on the other hand, displays a semi- metallic behavior. This is a significant result that can also be utilized as a sensor for the mercury contamination.

6.4 Summary and Conclusion

In this chapter the fabrication of Hg nanostructures (NS) templated on the linear DNA is demonstrated. The Hg-NS, exclusively interact with the nitrogen bases of the DNA and have no influence on the phosphorus backbone of DNA. The conjugation displays the formation of two metal-base complexes which can be considered as the signature of metal-DNA conjugation. Energy stabilization estimates suggest that these complexes form after the interaction of Hg ion with the G-C base pairs. Formation of these complexes and the modifications in transport behavior of DNA, on interaction with Hg-metal will have applications as sensor of mercury contamination.

References

[1] J.L. Coffer, S.R. Bigham, R.F. Pinizzotto, H. Yang, Nanotechnology, 3 (1992) 69.

[2] C.A. Mirkin, R.L. Letsinger, R.C. Mucic, J.J. Storhoff, Nature 382 (1996) 607.

[3] A.P. Alivisatos, K.P. Johnsson, X. Peng, T.E. Wilson, C.J. Loweth, M.P. Bruchez Jr., P.G. Schultz, Nature 382 (1996) 609.

[4] E. Braun, Y. Eichen, U. Sivan, G. Ben-Yoseph, Nature 391 (1998) 775.

[5] J. D. Le, Y. Pinto, N. C. Seeman, K. Musier-Forsyth, T. A. Taton, and R. A. Kiehl, Nano Lett., 4, 2343 (2004).

[6] J. Zhang, Y. Liu, Y. Ke, and H. Yan, Nano Lett., 6, 248 (2006).

[7] L. Berti and G. A. BurLey, Nat. Nanotech., 3, 81 (2008).

[8] K. Keren, M. Krueger, R. Gilad, G. Ben-Yoseph, U. Sivan, E. Braun, Science, 297, 72 (2002).

[9] Subrata Majumder, M. Priyadarshini, U. Subudhi, M. Umananda, G. B. N. Chainy, P. V. Satyam, and Shikha Varma, Appl. Phys. Lett., 94, 073110 (2009).

[10] S. Majumder, M. Priyadarshini, U. Subudhi, G.B.N. Chainy and Shikha Varma, Appl. Surf. Sci., 256, 438-442 (2009).

[11] A. Haug, S. Schweizer, F. Latteyer,M. B. Casu, H. Peisert, C. Ochsenfeld, T. Chasse, Chem. Phys. Chem., 9, 740 (2008).

[12] J. Peeling, F.E. Hruska, and N. S. McIntyre, Can. J. Chem., 56, 1555 (1978).

[13] J. V. Burda, J. Sponer, J. Leszczynski, and P. Hobza, J. Phys. Chem. B., 101, 9670(1997).

[14] K. L. Tan, B. T. G. Tan, E. T. Kan, and K. G. Neoh, Phy. Rev. B., 39, 8070 (1989).

[15] A.G. Macdiarmid, J. C. Chiang, and A. F. Richter, Synth. Met., 18, 285 (1987).

[16] Jin-Chih Chiang and A. G. Macdiarmid, Synth. Met., 13, 193 (1986).

[17] J. Yang, B. K. Pong, J. Y. Lee, and H. P. Too, Jour. Inorg. Biochem., 101, 824 (2007).

[18] J. Duguid, V. A. Bloomfield, J. Benevides, and G. J. Thomas Jr., Biophys. J., 65, 1916 (1993).

[19] Y. Liu, W. Meyer-Zaika, S. Franzka, G. Schmid, M. Tsoli, and H. Kuhn, Angew. Chem., Int. Ed., 42, 2853 (2003).

Chapter 7

Summary and Conclusion

The studies presented here, in this thesis, demonstrate the formation of TiO_2, ZnO and Hg nanostructures and their interactions with DNA. The oxide (TiO_2, ZnO) and Hg nanostructures display immense potential for numerous applications in the fields of photocatalysis, optical and electronic devices, magnetic recording media and biosensors. The formation of nanostructures, here, has been undertaken by a variety of routes for creating self assembled structures. The modifications in the conformations of DNA molecule, through interaction with these nanostructures, have also been investigated here.

An introduction to the basic concepts on the formation of nanostructures and some theoretical concepts are presented in **chapter-1**. The nanostructures, here, have been created by several methods like ion irradiation, Physical Vapor deposition and through selective conjugation within DNA. Discussions of these selected methods along with the various experimental techniques, utilized in this thesis, are presented in **chapter-2**.

Chapter-3 presents the formation of nanostructures on TiO_2 surfaces by low energy ion irradiation technique. Fabrication of patterns, by this method, is a powerful technique to grow self assembled nanostructures, on large surface area, in a single technological step. The nanostructures were formed on rutile $TiO_2(110)$ surfaces using 3keV Ar^+ ions, from

ECR source, at a fluence of 1.5×10^{19} $ions/cm^2$. Preferential sputtering of the surface results in the formation of oxygen vacancies (like Ti^{3+} states) as well as Ti rich zones on the nanopatterned surfaces. The existence of Ti rich zones act as the nucleation centre for the creation of nanodots on the ion sputtered surfaces. A compressive stress inside the crystal is also generated in the lattice along [110] direction due to the reduction in the interplanar separation after the sputtering. The nanodot patterned surfaces show a remarkably enhanced UV-Vis absorption, higher PL as well as a reduction in bandgap. These properties can be utilized for better photocatalytic behavior.

Chapter-4 describes the interaction of plasmid DNA with the nanodot patterned TiO_2 surfaces. The nanostructures were created via ion beam irradiation of surfaces by utilizing low energy Ar^+ ion source in UHV. The results show prominent alteration in the conformation of DNA molecule after its interaction with the ion sputtered surfaces. The morphological parameters of DNA, like its correlation length (ξ) and persistence length (P), as well as the size of DNA have been investigated to understand the adsorption properties and interaction behavior of DNA with the surfaces. An increase in the morphological parameters of DNA and an enhancement in DNA- diameter displays a larger interaction and a higher adsorption of DNA on ion irradiated surfaces. This also suggests a better biocompatibility and hydrophilicity, increasing with fluence, of the sputtered surfaces. The Ti rich sites and oxygen vacancies, created after the sputtering of TiO_2 surfaces, are crucially responsible for increased charge transfer from negatively charged phosphate backbone of DNA to the patterned surfaces.

Chapter-5 presents the formation of ZnO nanostructures produced by PVD method. The undoped ZnO nanostructures are semiconducting in nature and display room temperature ferromagnetism. The smaller ZnO nanostructures, of size $\sim$90nm, show isolated magnetic domains, where as, the larger ZnO nanostructures, of size $\sim$270nm, show long range magnetic ordering along with strong exchange interactions. The experimental results from XPS and PL studies show the presence of higher Oxygen vacancies in the larger nanostructures, and the room temperature ferromagnetism may be primarily arising due to these Oxygen vacancies in the ZnO nanostructures. The interaction of DNA with ZnO nanostructures has also been investigated here. The larger sized nanostructures show better stability of the DNA molecule, compared to the smaller sized nanostructures, where the DNA agglomerates on the surface.

Chapter-6 presents the fabrication of Hg nanostructures using the DNA template. The Hg nanostructures form by rupturing the nitrogen bases of the DNA. The experimental results strongly support the fact that, Hg nanostructures exclusively interact with the nitrogen bases (G and C in the present study) and have no influence on the phosphorus backbone of DNA. The protonation of amine group, of the DNA bases, promotes the formation of the metal-base complexes like, Metal-Purine (M-Pu) and Metal-Purine-Pyrimidine (M-Pu-Py). The as formed Hg-base complexes have also displayed very different electrical conduction behavior compared to the unreacted DNA. This unique finding shows the possibilities in the development of a sensor for mercury contamination and DNA assays.

In conclusion, the metal oxide, TiO_2(110) and ZnO, nanostructures, studied here, show several unique properties. The nanostructures created on the TiO_2 surfaces show enhanced optical properties in the visible as well as in the UV regime. The Oxygen vacancies created during the sputtering process have been shown to be primarily responsible for these enhanced photocatalytical properties. These nanodot patterned surfaces also display higher biocompatibility and hydrophilicity. The ZnO nanostructures display room temperature ferromagnetism in the absence of any magnetic doping. The larger nanostructures show very strong long range magnetic ordering at room temperature. The Oxygen vacancies created, during growth, are primarily responsible for these observations. The larger nanostructures are also more biocompatible, with DNA displaying more stable conformations on them. Self assembled Hg nanostructures have been fabricated through the conjugation within the DNA double strands. The interaction between the Hg nanostructures and DNA has been investigated and the results show that Hg exclusively interacts with the nitrogen bases of the DNA and not with the phosphate backbones. The formation of two specific metal- base compounds as well as the modification in the transport properties, after interaction of Hg with DNA, have been demonstrated here. Both these properties, together display that DNA can be used as a sensor of mercury.